Structural geology and geochronology of the Kluane schist, southwestern Yukon Territory

by
Benjamin Stanley

A thesis

presented to the University of Waterloo

in fulfilment of the

thesis requirement for the degree of

Master of Science

in

Earth Sciences

Waterloo, Ontario, Canada, 2012

I hereby declare that I am the sole author of this thesis. This is a true copy of the thesis, including any required final revisions, as accepted by my examiners.

I understand that my thesis may be made electronically available to the public.

Abstract

In light of the recent increase of mineral exploration in the northern Cordillera, private, educational, and governmental agencies have been compelled to revisit and research areas of the Cordillera whose geologic evolution still remains enigmatic. The current study is concerned with better understanding how a region of the boundary zone separating the peri-Laurentian realm from the exotic, Insular realm evolved following deposition of the meta-sedimentary Kluane schist in the Late Cretaceous. The schist is a northwest striking 30 km wide and 160 km long belt of highly deformed greenschist to amphibolite facies meta-sedimentary rocks located east of Kluane Lake, southwestern Yukon Territory. These deformed sediments as well as numerous other deformed Jurassic-Cretaceous meta-sedimentary units present along the same boundary zone (north and south of the schist) represent important rocks that can help constrain how this part of the Cordillera has evolved since the mid-Mesozoic.

To better understand how the Kluane schist evolved, detailed field mapping, petrography, and U-Pb geochronological studies were undertaken in the area encompassing the schist. This data is integrated with pre-existing and recently collected geologic databases from the region to propose a model for the tectonic and structural evolution of the Kluane schist. Conclusions drawn from this study indicate the Kluane sediments were likely deposited into a closing Late Cretaceous seaway from sources derived from Yukon-Tanana terrane (YTT) to the east. The basin into which the sediments were deposited represents a remnant ocean basin that was present between Insular terrane and YTT prior their amalgamation in the Jurassic. Thrusting of YTT over the Kluane schist basin resulted in burial, metamorphism, and ductile deformation of the schist. Contemporaneously, the early stages of the Ruby Range batholith (RRB) were intruding the schist as well as the schist/YTT contact. This batholith intruded syn- to post-tectonically from approximately *ca.* $\geq$ 77 Ma to 65 Ma and it is responsible for imparting a kilometer scale inverted contact metamophic aureole onto the Kluane schist wherein metamorphic grade decreases to the southwest. Subsequently, a gneissic sub-unit of the Kluane 'schist' was formed by partial melting of the RRB/Kluane schist contact. During this composite deformation event, the schist was transported to mid-crustal depths by an oblique sinistral shear zone. Shortly thereafter, the schist was exhumed and deformed by consistent northeast-over-southwest shearing. Regional scale, broad open folding of the schist ensued and likely occurred by flexural slip along foliation planes with low cohesion. Two syn- to post-tectonic igneous phases associated with Hayden Lake intrusive suite have been dated to *ca.* 55 Ma. This timing likely correlates with broad, open folding and a 'late' syn- to post-kinematic

thermal overprint of the schist. The combined results of this study indicate that deformation and metamorphism of the Kluane schist was a long-lived event, extending from *ca.* 82 Ma to *ca.* 55 Ma.

Acknowledgements

I would like to thank my two supervisors Dr. Shoufa Lin and Dr. Cees van Staal for the opportunity to work and learn alongside their two creative minds. The friendly staff at the Yukon Geological Survey were also important to this study, specifically Dr. Steve Israel and Dr. Don Murphy. I am also indebted to Dr. Don W. Davis, Dr. Mike Tubrett and Dr. Vanessa Bennett for their patience and guidance during the laboratory component of this work. My family and friends as always play an important role in all my endeavors and for that I would like to thank them from the bottom of my heart.

Table of Contents

List of Figures

List of Tables

1 Introduction

1.1 Scientific background and thesis objectives

The northern Cordillera is a mountain belt extending from southern British Columbia, through Yukon into Alaska. The present day Cordillera was founded upon the ancient western margin of the Laurentian craton (future North America; Figure 1), which has been tectonically active since Proterozoic time when the supercontinent Rodinia was shedding detritus into flanking depocenters. Intra-continental rifting resulted in the break up of Rodinia and the birth of the Paleozoic supercontinent Pangea. Mesozoic time is punctuated by the northern Cordillera mountain building event. This orogeny is commonly referred to as a relatively young event since its inception has been tied to the opening of the North Atlantic Ocean during Middle Jurassic time. As this ocean opened, Pangea broke apart to form Laurentia. Subsequently, Laurentia and the peri-cratonic terranes were pushed west towards an east-directed Triassic(?) subduction zone (Murphy *et al.,* 2009; Monger and Price, 2002). From Triassic to the Late Cretaceous/Early Tertiary time, this subduction zone and another east-dipping subduction zone outboard of the exotic, oceanic Insular terrane played a critical role in creating voluminous arc-derived magmatism upon peri-Laurentian and Insular terranes. The subsequent amalgamation of these two terranes in the Jurassic resulted in deforming various sedimentary basins that were also evolving along peri-Laurentia's western margin and Insular's eastern margin.

In southwestern Yukon Territory, the current study area is located at the tectonic boundary that separates the peri-Laurentian realm [Yukon-Tanana terrane (YTT)] from the exotic, oceanic realm (Insular terrane; Figure 1). Within the study area, these terranes are separated by the deformed greenschist facies Jurassic-Cretaceous Dezadeash Formation, the highly-deformed greenschist to amphibolite facies Late Cretaceous Kluane schist, and the syn- to post-tectonic Late Cretaceous to Eocene Ruby Range batholith (RRB), from west to east respectively (Figure 2). The Dezadeash Formation is derived from Insular terrane to the west and the Kluane schist is believed to be sourced from YTT to the east (Eisbacher, 1976; Israel *et al.,* 2011a). The RRB is a broadly northwest-southeast striking syn- to post-tectonic magmatic lesion that represents the northern extent of the Coast plutonic complex. The RRB obliterates most of the original YTT/Kluane schist contact. The Denali fault system lies west of the schist as anastomosing Paleocene (and younger) dextral strike-slip faults. This fault system is an arcuate feature that strikes west-east through Alaska and curls southeastward through Yukon and British Columbia (Figure 1).

The tectonic setting of the Kluane schist sedimentary protolith remains enigmatic wherein several authors support a back-arc-basin depositional setting (Eisbacher, 1976; Lowey, 1992,

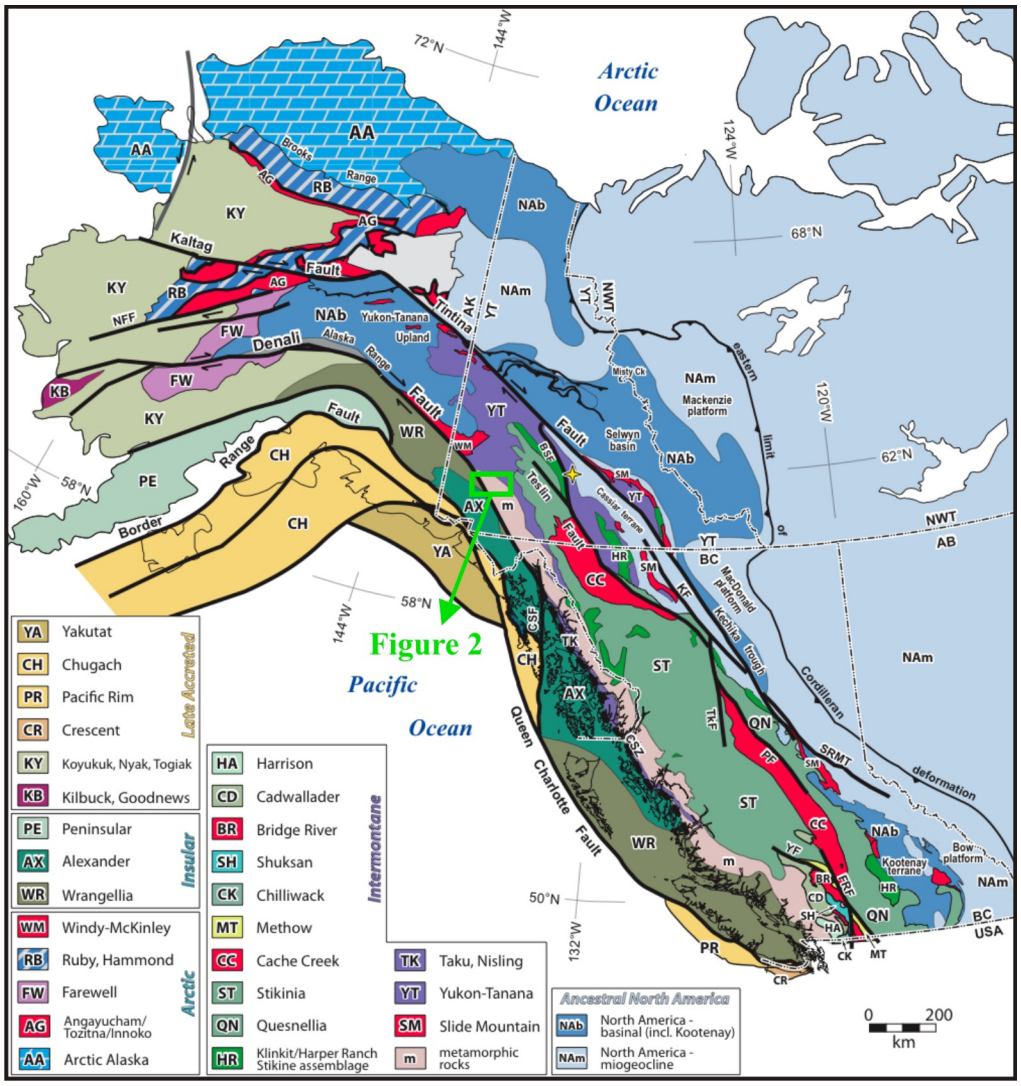

Figure 1: Terranes of the northern Cordillera. Geological features/regions and major strike-slip fault systems are shown. Green rectangle at center indicates location of Figure 2. Yellow star marks the location of Solitary Mountain in south-central Yukon Territory. Fault abbreviation: CSZ = Coast shear zone. Other abbreviations: AB - Alberta; AK - Alaska; BC - British Columbia; NWT - Northwest Territories; YT - Yukon Territory. Compiled from Wheeler *et al.,* (1991); Silberling *et al.,* (1994); Colpron (2006). Other abbreviations are found in Figure 1 of Nelson and Colpron (2007) with references therein.

2007; Mezger, 1997, 2000, 2003; Mezger *et al.,* 2000, 2001) and others promote an accretionary fore-arc-related depositional setting (Ridgway *et al.,* 2002; McClelland and Saleeby, 1992; McClelland *et al.,* 2000; Murphy *et al.,* 2009; Mortensen and Hart, 2010). The lack of abundant relatively young oceanic crust and the lack of back-arc-related magmatism proximal to the study area indicates the tectonic setting was more likely a subduction zone. The basin that originally hosted the Kluane schist protolith was a broad oceanic basin that collapsed shortly after deposition (discussed in detail later in document). Along the trend of the Denali fault

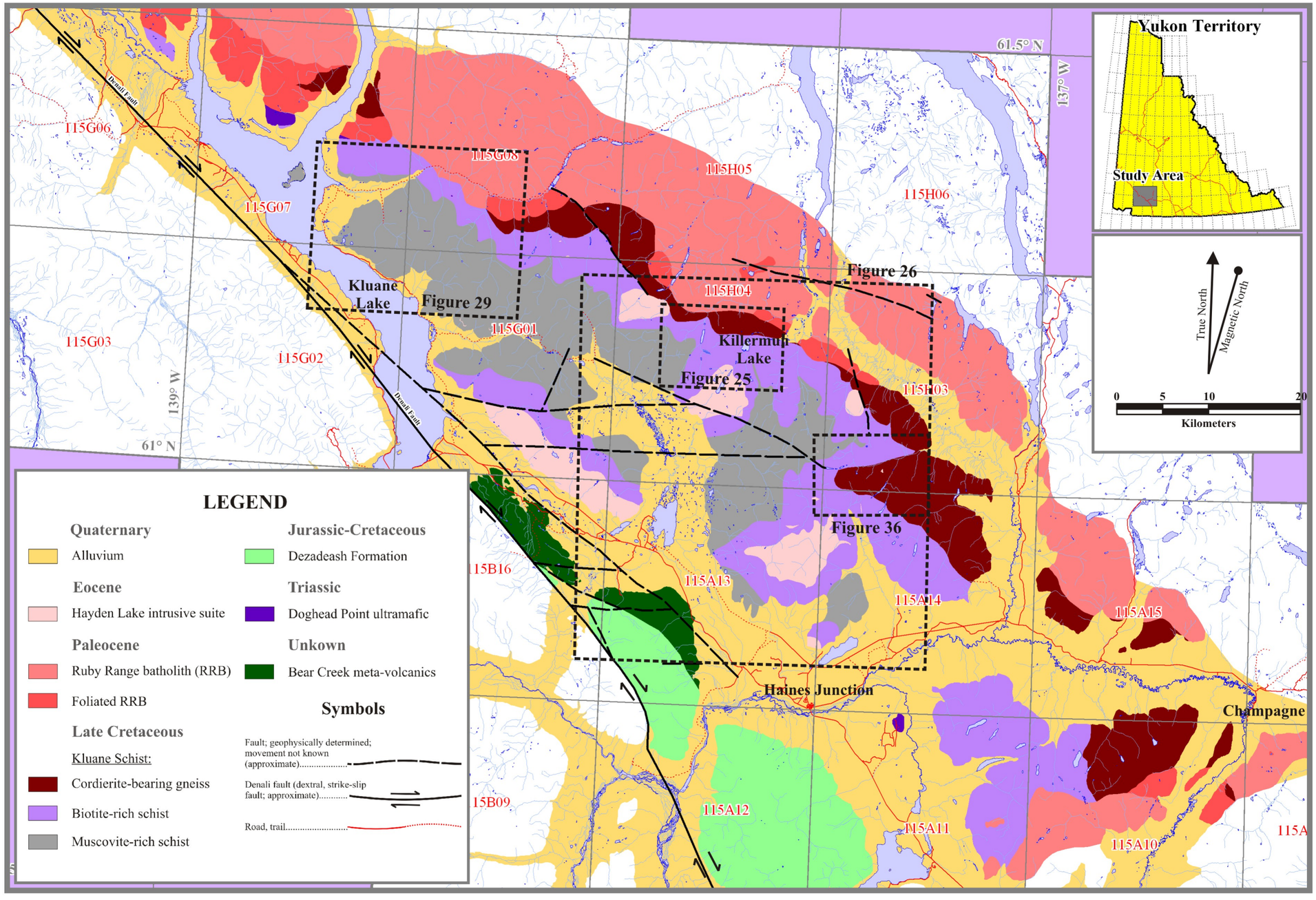

Figure 2: Simplified geological map of the study area. Rhyolite Creek volcano-plutonic complex and Yukon-Tanana terrane are absent from legend since the units do not outcrop at the scale of this map. Outlined polygons represent location of detailed maps in succeeding chapters. A detailed map at the same scale of this figure is available in the appendix A of this document.

system several variably deformed and metamorphosed Jurassic-Cretaceous sedimentary basins are present; they include the: Kahiltna, Nutzotin, Gravina, and Bowser basins. The deformed sediments that originally filled these basins (and the Kluane basin) are important to Cordilleran tectonics because their current structural characteristics preserve how the peri-Laurentia and exotic, oceanic realms were behaving during Late Jurassic to Early Cretaceous amalgamation (McClelland and Saleeby, 1992; McClelland *et al.,* 2000; Ridgway *et al.,* 2002; Hampton *et al.,* 2010).

The current study is concerned with a structural and geochronological analysis of the Kluane schist and associated plutonic rocks. Although this study is not the first to encompass the schist or parts thereof (Eisbacher, 1976; Mezger, 1997, 2000, and 2003; Mezger *et al.,* 2000 and 2001; Israel *et al.,* 2010 and 2011), it does represent a more detailed approach to understanding the intricacies of micro- to macroscopic structures ubiquitously observed throughout the schist. The primary aim of this research is to constrain how and when the Kluane schist evolved during the Late Mesozoic to Early Cenozoic when it was deposited and subsequently deformed. To answer these questions, overprinting field relationships of foliations, lineations, and folds are used to document four distinct generations of structures with several intervening periods of quartz-vein and pluton/dyke emplacement.

1.2 Scope of this study

This study is one of numerous academic works being completed in northern Canada under the supervision of Dr. Cees van Staal at the Geological Survey of Canada (GSC). This and many other projects are a direct result of the Canadian federal government's 2008 initiative to undertake five years of Geo-mapping for Energy and Minerals (GEM) in northern Canada. Underneath the GEM program, the Edges project aims to assist mineral exploration in the northern Cordillera by outlining resource-rich regions in and associated with the exotic, accreted terranes[1]. The current study has been directly funded by the GEM-Edges project, as well as supplemental funding from the Yukon Geological Survey (YGS) and an NSERC discovery grant.

In total, approximately five months were spent in the field from early July, 2009 to late August, 2010 during which a sizable data-set was collected. Data collection for this study covered an area of approximately 3800 km^2 between the small town of Champagne and the

[1] Although the economic potential of the schist is not the focus of this study, it should be mentioned that the schist is prospective for gold exploration. This fact is supported by the numerous placer gold mines (*e.g.,* Gladstone, Twelve of July and Granite creeks; see mapsheets 115G07, 115G01, and 115A11 in appendix A) and the abundant mineral tenures that veil a large portion of the Kluane schist's bedrock exposure (see YGS MapMaker Online at www.geology.gov.yk.ca for additional information).

northwest end of Kluane Lake (Figure 2). Traverses were made dominantly along ridges and on small access and main roads. Access to these areas was accomplished by helicopter support as well as all wheel drive vehicles. The data were compiled on a base-map at a scale of 1:100,000. The regional geological map of southwestern Yukon Territory by Israel (2004) was used as a general reference map for preliminary structural, stratigraphic, and tectonmetamorphic information. To complement the data-set, portions of maps by Muller (1967), Mezger (1997), and Israel (2004) were imported and digitized into a computer. Geological attributes found in these maps and not observed during the course of this study were, in places, used to augment the geological information collected during this study. The locations of the attributes were carefully positioned to retain map interpretations of the original authors. This was done to compare and complement the detailed data-set collected for this study.

The laboratory component of this study involves uranium-thorium-lead (U-Th-Pb) zircon geochronology using laser ablation-inductively coupled plasma mass spectrometry (LA-ICPMS). This method was used on four schist, one gneiss, and three igneous samples from the Kluane schist and associated plutonic rocks. The objectives of this laboratory work are to contribute age constraints to an ongoing study aimed at better understanding the paleotectonic setting(s) and evolution of terranes and terrane boundaries in the northern Canadian Cordillera. To meet this objective, samples collected during the summer field-season of 2009 and 2010 were processed and analyzed by the author at the Jack Satterly Geochronology Laboratory, University of Toronto, under the supervision of Dr. Don W. Davis and, at the Core Research Equipment and Instrument Training Network, Memorial University under the supervision of Dr. Mike Tubrett and Dr. Vanessa Bennett.

A detailed 1:100,000 scale bedrock/structural map of the area encompassing the Kluane schist is enclosed in Appendix A of this document. This map is based on data compiled at 1:50,000 scale and interpretations from regional aeromagnetic data. A simplified version of this map is included as Figure 2 above. The area covered by this map is referred to as the study area throughout the thesis.

1.3 Thesis outline

This thesis is composed of four main chapters ($2-5$). In Chapter 2, the regional geological setting is introduced, detailed stratigraphic descriptions of the units within the study area are presented, and a current understanding of the tectonic evolution of the study area is summarized. A structural analysis of the Kluane schist and associated plutonic rocks is presented in Chapter 3. Field observations, detailed petrography, and ages are used to constrain the geometry and kinematic evolution of the Kluane schist. In Chapter 4, absolute age constraints

on the timing of multiple episodes of deformation within the Kluane schist are presented based on LA-ICPMS U-Pb ages of detrital, magmatic, and metamorphic zircons from samples with clearly defined field relationships. This age data is compared with available U-Pb ages throughout the study area to discern the importance of Late Cretaceous deformation. 'Late' thermal events overprint the Kluane schist and are constrained by previously determined K/Ar and Ar/Ar cooling ages (Mezger, 1997 with references therein). Finally, Chapter 5 incorporates a discussion on the field and analytical data with a model for the tectonic evolution of the Kluane schist from deposition in the Late Cretaceous to the present.

2 Stratigraphic and tectonic framework

2.1 Introduction

Substantial databases consisting of geochronological, isotopic, geochemical, fossil, paleomagnetic, and mineral deposits have allowed for an elegant, though still not complete reconstruction of the northern Cordillera. Data collected for this study is concentrated along an important tectonic boundary zone separating the peri-Laurentian realm from the exotic, Arctic realm; therefore, understanding the structural complexities of rocks found in this zone provide valuable information in regards to its evolution. The current study area includes a fragment of the intensely deformed Paleozoic Yukon-Tanana terrane, Triassic ultramafic bodies, the Late Cretaceous Kluane schist, as well as numerous Cretaceous and younger syn- to post-tectonic intrusive and extrusive phases. The sections that follow serve to highlight this stratigraphy and the tectonic framework of the Cordillera with emphasis given to the current study area.

2.2 Paleozoic stratigraphy

2.2.1 Yukon-Tanana terrane (YTT)

Approximately 20 kms northeast of the current study area, YTT rocks outcrop in a large areal extent as a structurally northeast-dipping panel of rocks. Within the study area YTT rocks outcrop only in two areas: 1) intrafoliated within the Kluane schist and 2) as an isolated roof pendant within the Ruby Range batholith (RRB). The voluminous RRB obliterates the majority of the YTT-Kluane schist contact; therefore, the sole observation of YTT rocks intrafoliated within the Kluane schist represents an important contact. North of the study area, YTT rocks commonly outcrop as roof pendants within the RRB and Early Jurassic Aishihik batholith to the east. These roof pendants are composed of poly-deformed and metamorphosed psammitic schists, quartzite, marble, garnet amphibolite, and rare meta-plutonic rocks (Israel *et al.,* 2011a). The presence of carbonate within YTT rocks is variable and can, in places, be pervasive. YTT rocks are typically deformed by tight to isoclinal folds that have re-folded interference patterns. Johnston and Erdmer (1995) indicate that pre-Jurassic and Jurassic deformation and metamorphism are responsible for the initial foliation development. Further to the east, YTT takes on a relatively higher degree of metamorphism possibly related to the proximal Aishihik batholith (Johnston and Erdmer, 1995; Israel *et al.,* 2011a).

YTT rocks within the current study area are observed only at two locations. At station 10-VLS-272, 5 km west of Killermun Lake (Figure 2), YTT outcrops as an approximately 100 m thick and 300 m long outcrop of foliated and intensely calcareous sedimentary and mafic

and felsic volcanic rocks (Figure 3). This outcrop is mantled above and below by foliated biotite-rich Kluane schist that contains a foliation oriented parallel to the orientation of the foliation in the YTT body (Figure 4). The lateral extent of this outcrop is unknown. At station 10-VLS-337, 7 km south-southwest of Champagne (Figure 2), YTT also appears as a 20 m long elongate roof pendant of foliated calcareous psammitic schists with subordinate mafic volcanic rocks. The contact between this roof pendant and the surrounding foliated hornblende-biotite-tonalite (*i.e.,* RRB) is covered by rubble and vegetation.

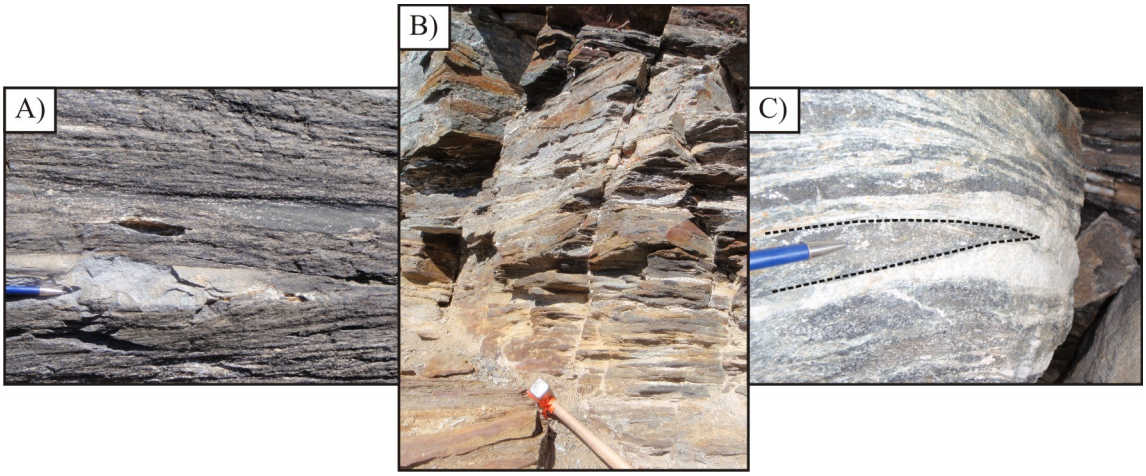

Figure 3: YTT stratigraphy observed at station 10-VLS-272. Photos A through C represent structurally highest to lowest units in outcrop. A) Foliated mafic volcanic rock with deformed felsic volcanic fragment oriented parallel to foliation (parallel to pencil). B) Interbedded buff weathered brown to grey calcareous psammitic and semi-pelitic schists. C) Interbedded white marble and grey calcareous psammitic schist with isoclinal fold defined by the trace of a white marble layer (black dashed line).

YTT is believed to be composed of four Paleozoic tectonic assemblages: the basal siliciclastic Snowcap assemblage that was derived from Laurentia's northwestern passive margin and, three unconformity-bounded volcanic and volcaniclastic successions of predominantly continental arc affinity (Piercey *et al.,* 2006 with references therein): Upper Devonian to Lower Mississippian Finlayson assemblage, mid-Mississippian to Lower Permian Klinkit assemblage, and the Middle to Upper Permian Klondike assemblage. Israel *et al.* (2011a) believe that YTT rocks proximal to the current study area appear similar to Snowcap and Finlayson assemblages.

2.3 Mesozoic to Early Cenozoic stratigraphy

2.3.1 Triassic - Ultramafic bodies

Numerous outcrops of ultramafic rocks are present throughout the entire Kluane schist. These ultramafic rocks are antigorite-olivine serpentinite schist, talc serpentinite schist, and olivine-enstatite meta-peridotite metamorphosed from greenschist to amphibolite facies (M. Escayola,

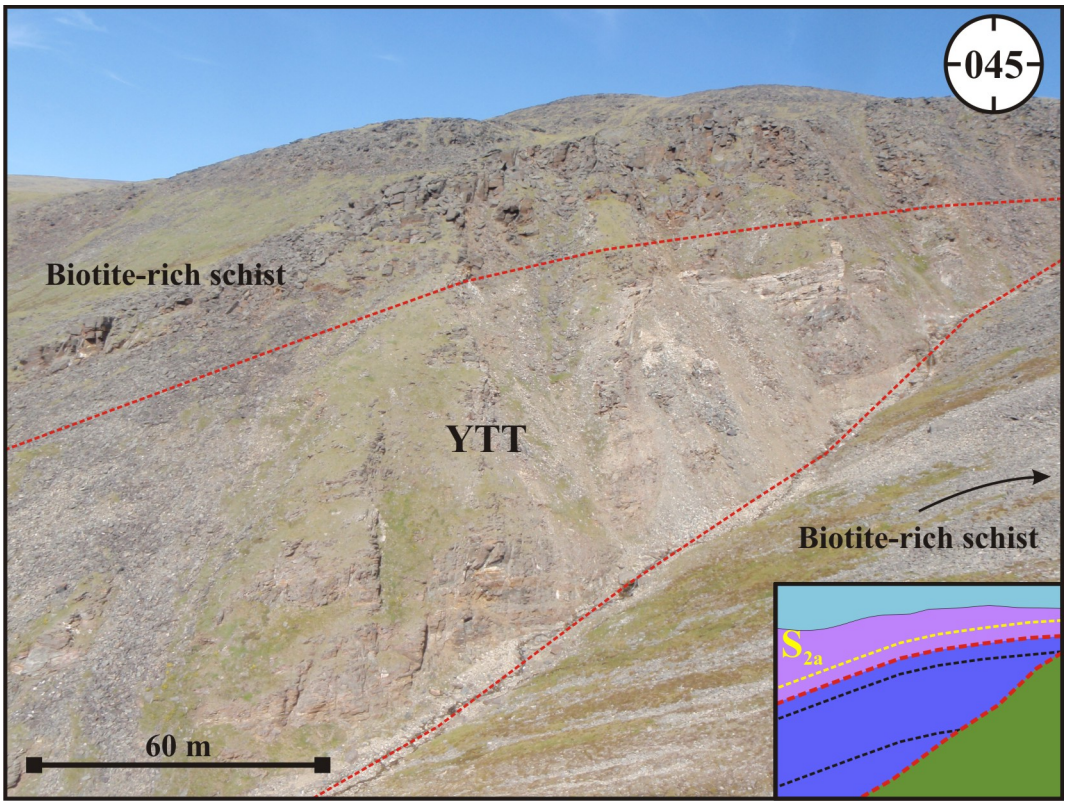

Figure 4: YTT outcrop (enclosed in red dashed lines) observed at station 10-VLS-272 (looking 045°). Inset image shows the YTT outcrop is mantled above by biotite-rich schist that retains a well-developed foliation (S_{2a} - yellow dashed line) oriented parallel to the foliation observed in the YTT rocks (black dashed line) and the top lithological contact (red dashed line). The trace of the bottom contact is apparent since it is a creek bed that cuts into the lower hillside that is covered by rubble and vegetation (green in inset image).

pers. comm., 2011). Fresh surfaces appear silky green to dark grey and weathered surfaces are typically buff brown to rusty brown. The northwestern most exposure of these rocks are represented by the Doghead Point ultramafic (Figure 2). This exposure is a kilometer-scale foliated outcrop in contact with foliated RRB to the north and biotite-rich Kluane schist to the south. The Doghead Point ultramafic unit is distinguished by an obvious positive magnetic anomaly on the 1969 GSC aeromagnetic map (Mezger, 1997). Southeast of this exposure, numerous meter scale foliated ultramafic bodies are present intrafoliated within the muscovite- and biotite-rich Kluane schist units (Figure 5A). The furthest southeastern exposure of this ultramafic unit is represented by a kilometer scale outcrop south of Haines Junction (Figure 2). The contact of this exposure is buried beneath alluvium.

The ultramafic rocks are predominantly composed of dominantly forsterite, antigorite, talc, and enstatite with subordinate amounts of iddingsite, magnetite, chromite, pentlandite, and trace calcite (Figure 5B and C; Mezger, 1997; M. Escayola, pers. comm., 2011). Forsterite

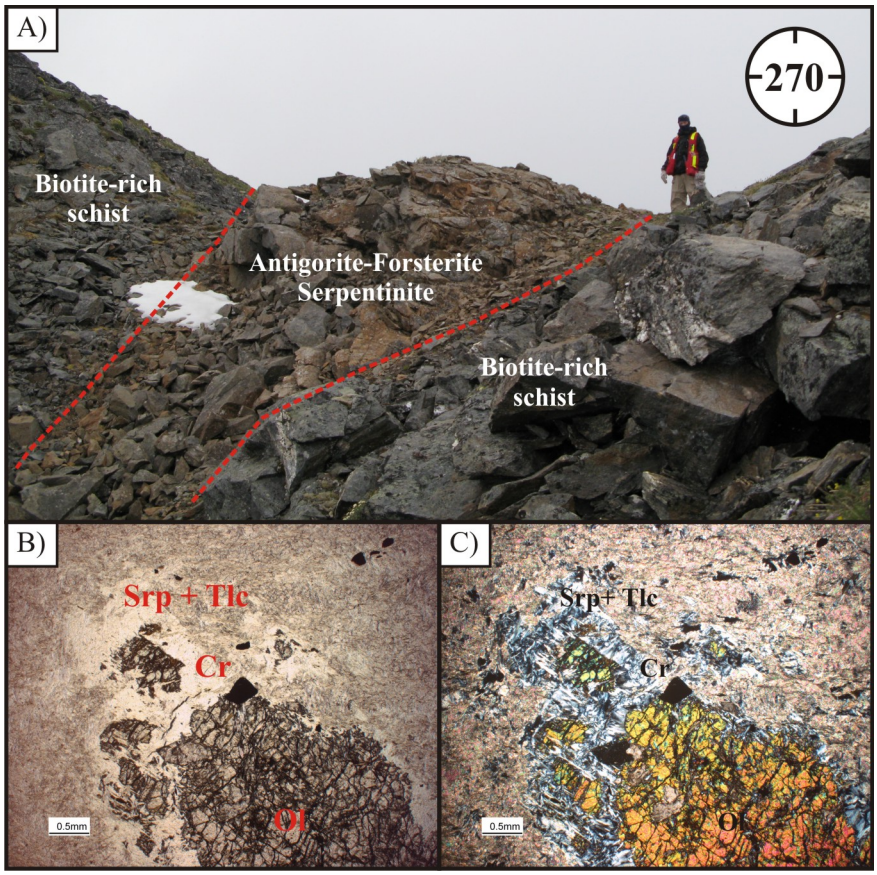

Figure 5: Outcrop and thin section examples of antigorite-olivine serpentinite intrafoliated between biotite-rich Kluane schist. A) Station 09-VLS-030 looking 270°. B) Plane polarized light thin section photograph of antigorite-olivine serpentinite from station 09-VLS-303 (Ol = olivine; Srp = serpentine; Tlc = talc; Cr = chromite) and C) corresponding crossed polarized light thin section photograph.

and talc, in places, appear as coarse anhedral grains wherein forsterite grains are mantled by a corroded rim containing fine grained antigorite. These olivine grains commonly contain fine grained inclusions of chromite. Metamorphic growth of antigorite and olivine in an igneous olivine-rich matrix is indicated by Escayola (pers. comm., 2011) wherein both metamorphic minerals appear in paragenetic equilibrium (*i.e.,* high greenschist facies metamorphism). Poikilitic talc crystals are also present and indicate prograde metamorphism. Prograde metamorphism is also recorded by the presence of olivine and enstatite in equilibrium (*i.e.,* amphibolite facies metamorphism).

In places, planar fabric forming elements defined by the alignment of antigorite and talc are present in these rocks. At Doghead Point, the dominant north dipping foliation in the ultramafic body is oriented parallel to the foliation in the proximal biotite-rich schist and parallel to the foliated RRB unit/contact. Similarly, the other relatively smaller foliated and massive ultramafic outcrop exposures are oriented parallel to the dominant foliation of the host

schist. Mezger (1997) states the presence of a C/S structural fabric within the Doghead Point ultramafic unit as well as talc and tremolite crystals that overgrow the dominant foliation plane. At the northern margin of the Doghead Point ultramafic exposure, Mezger (1997) records fresh olivine grains that overgrow the dominant foliation plane indicating contact metamorphism. Along strike of the Doghead Point ultramafic unit, Escayola (pers. comm., 2011) notes the unit displays progressive metamorphism from antigorite-olivine to talc-olivine schist, as well as the preservation of dunite dykes and tronhdjemite veins. This compositional zoning is believed to represent a compositional variation of the metamorphosed protolith (*i.e.,* harzburgite and dunite rocks intruded by dunite). Uranium-Pb geochronology completed by Escayola (pers. comm., 2011) yield crystallization ages of 205.9 $\pm$ 0.4 Ma to 206.8 $\pm$ 3.2 Ma for the Doghead Point ultramafic unit.

Escayola (pers. comm., 2011) interpret ultramafic rocks of Doghead Point as part of a mantle transition zone. The emplacement mechanism for these rocks remains ambiguous. However, these rocks were at least in contact with the Kluane schist early in the schist's tectonic evolution since the juxtaposed units retain similar and parallel tectonic fabrics (discussed in Chapter 3).

2.3.2 Cretaceous - Kluane schist

2.3.2.1 Introduction

The Kluane schist is a highly deformed package of monotonous psammitic to semi-pelitic sedimentary rocks that were deposited during the Late Cretaceous (Israel *et al.,* 2011). The schist outcrops throughout the northern and southern sections of the Dezadeash and Ruby ranges, respectively (Figure 2). Towards the east, the schist is overlain by the RRB, which in-turn is overlain by YTT. All three units outcrop as broadly northeast-dipping panels except for the southermost portion of the schist which dips towards the southwest. South of Kluane Lake, the schist's southwestern boundary with the Jurassic-Cretaceous Dezadeash Formation and associated Bear Creek meta-volcanic rocks (unknown age and affinity) is covered by alluvium of the Shakwak Trench. This valley fill is believed to cover splays to the main northwest-southeast striking dextral strike-slip Denali fault system. Displacement on the Denali fault and its splays is believed to be upwards of 400 kms and likely occurred at *ca.* $\leq$ 54 Ma (Ridgway *et al.,* 2002).

Since the schist lacks good marker horizons, mapping of slight lithological variations produced three distinct units similar to that of Mezger (1997) and Israel *et al.* (2011a): 1) muscovite-rich schist, 2) biotite-rich schist, and 3) cordierite-bearing Kluane gneiss. The dis-

tinction of these three units is subtle, wherein the dominance of muscovite and/or biotite defines the first two units. The cordierite-bearing gneiss is defined by the abundance of centimeter scale thick leucocratic quartzofeldspathic igneous layers, which are also present in the biotite-rich schist in subordinate to trace amounts. The transition between the three units is gradational over hundreds of meters. All three units appear to preserve similar early tectonic evolutions since they retain identical micro- to macroscopic planar and linear structural fabrics (discussed in detail in Chapter 3). Post-tectonic metamorphism of the three units is variable.

Uranium-Pb detrital zircon LA-ICPMS completed by Israel *et al.* (2011a) on samples of the Kluane schist indicate sediment deposition likely occurred as early as *ca.* 95 Ma. This same study found through analysis of the detrital zircon age populations that the sediments were likely sourced from YTT and Jurassic to Cretaceous plutons of the Aishihik batholith and the Coast Plutonic complex to the east. Geochemical and isotopic signatures calculated by Mezger *et al.* (2001) confirm the Kluane sediments were sourced from a mixture of Archean and juvenile terranes. Metamorphic age constraints were also obtained by Israel *et al.* (2011a) after analyzing zircon overgrowths. Results from these analyses indicate significant Pb-loss and 'new' zircon growth events occurred at *ca.* 82 and 70 Ma. Detrital zircon U-Pb geochronology completed for the current study yields similar results. Geochronological age dating of syn- and post-tectonic igneous phases found within the Kluane schist were also targeted for U-Pb zircon LA-ICPMS. These samples were analyzed to ascertain age constraints of the various deformation events that overprint the schist. These ages and their significance are discussed later in this document.

Initial age determinations regarding the Kluane schist were obtained by K-Ar biotite, K-Ar muscovite, ^{40}Ar-^{39}Ar muscovite, Rb-Sr muscovite, U-Pb monazite, U-Pb xenotime, and depleted mantle model ages using Nd-isotopes (Mezger, 1997 with references therein). The former six methods produced ages ranging from 42.5 to 66.7 Ma for the muscovite- and biotite-rich schist units. Mezger (1997) indicates these ages are similar to previously determined K-Ar biotite ages calculated for the RRB (*i.e.,* 50 to 57 Ma; Farrar *et al.,* 1988). In terms of depleted mantle model ages, samples from the muscovite- and biotite-rich schist units yield 1.22 to 1.45 Ga ages using Nd-isotopes (Mezger, 1997). That same study concluded that although the model ages do not represent a time of deposition for the schist, the ages could possibly represent an age of the source rock(s). One sample from the cordierite-bearing gneiss was analyzed for U-Pb zircon LA-ICPMS during this study and, the results reveal a relatively complex detrital zircon age spectrum similar to the Kluane schist samples discussed in Israel *et al.* (2011a).

At the outcrop scale, grain size variations and the variable abundance of quartz and/or

mica in certain layers appears to exhibit primary clastic layering characteristics (Israel *et al.,* 2011a). Minor amounts of deformed and undeformed mafic and felsic dykes, ultramafic bodies, and carbonate-rich layers are present in the schist. As well, abundant amounts of deformed and undeformed milky white quartz(± carbonate)-rich veins are also present. These geologic features are introduced here and discussed in detail later in Chapter 3. The following subsections highlight the compositional and textural variation of the muscovite- and biotite-rich schists as well as the cordierite-bearing gneiss.

2.3.2.2 Muscovite-rich Kluane schist

The muscovite-rich Kluane schist, mapped as calcic schist by Mezger (1997) due to its abundance of calcium-bearing minerals, outcrops throughout the core of the schist exposure from Jacquot Island in the northwest to Paint Mountain in the southeast (Figure 2). North-northwest of Kloo Lake the muscovite-rich schist is a continuous unit mantled to the northeast and southwest by biotite-rich schist. This contact is parallel to the strike of the dominant foliation in both units and also parallel to the overall contact of the RRB to the northeast. The western exposure of the muscovite-rich schist is on Jacquot Island. Further towards the northwest, the entire schist exposure appears to thin until the bedrock map pattern is completely obscured by alluvium cover near Burwash Flats. From Shutdunmun Lake towards the southeast, the muscovite-rich schist map pattern is slightly more convoluted. This feature is the result of relatively younger intrusive phases that cross-cut and impart local contact metamorphic aureoles onto the schist. These intrusive phases are contemporaneous with regional scale, broad, open folding of the dominant foliation. The southeastern exposure of the muscovite-rich schist appears in the vicinity of Dezadeash River proximal to the northern extent of the Dezadeash Range. This region is covered by extensive amounts of alluvium.

Fresh surfaces of the muscovite-rich schist typically contain a grey to dark grey appearance, while weathered surfaces appear light grey to greenish-grey (Figure 6A). Outcrop exposures remain difficult to decipher due to weathering and the abundance of lichen that appears to thrive on all exposures of the schist. Petrographic investigations indicate the muscovite-rich schist is composed of medium to coarse grained plagioclase feldspar porphyroblasts and, fine to medium grained muscovite + chlorite + quartz + feldspar + epidote + abundant very fine grained opaque graphitic material (± hornblende, biotite, and garnet; Figure 6B and C). When present in moderate to abundant amounts, the plagioclase porphyroblasts give the schist a mottled, 'knotty' texture. Feldspar porphyroblasts are determined to be albite to oligoclase in composition based on electron microprobe work completed by Mezger (1997). Within the plagioclase porphyroblasts, graphite appears as very thin, parallel inclusion trails

that, in places, are crenulated into microscopic, open to close symmetric folds. Quartz, which makes up approximately 30 to 50 vol.% of the rock, is typically anhedral in shape and, fills the interstitial space between and/or forms layers between the other mineral phases. Mezger (1997) records that clinozoisite and minor amounts of epidote are common constituents in the muscovite-rich schist. These minerals appear as stubby, subhedral to euhedral fine to medium grains that make up to 10 vol.% of the rock. The transition between muscovite- and biotite-rich schist is gradational over hundreds of meters and, in places, is difficult to identify due to weathering and alteration. Also present in the gradational zone are fine to coarse grained anhedral to subhedral garnet porphyroblasts. In places, these porphyroblasts retain spiral-shaped inclusion trails of graphite. Electron microprobe studies by Mezger (1997) indicate the garnets range in composition from spessartine to almandine. Fine grained accessory phases include tournaline, apatite, sphene, zircon, illmenite, and calcite. Mezger's (1997, p. 15) detailed stratigraphic report indicates the presence of "discontinuous, boudinage[d], grass-green layers of coarse grained actinolite fels, [chrome]-mica-actinolite schist and greenish grey [chromite-muscovite-albite-actinolite-epidote-chlorite] schist... interfoliated with the [muscovite-rich schist]." These units may represent intensely altered portions of the Triassic ultramafic bodies (or sedimentary rocks derived from the ultramafic rocks) described above given their 'unique' chromium-bearing signature. These distinctly different layers were not observed over the course of this study.

Planar and linear fabric forming elements are ubiquitous in the Kluane schist. Within the muscovite-rich schist, the dominant spaced cleavage foliation is defined by a muscovite- and chlorite-rich cleavage and quartz- and feldspar-rich microlithons. Mineral aggregate and mineral stretching lineations are defined by elongate plagioclase porphyroblasts that intersect the dominant foliation surface and, elongate accumulations of quartz and feldspar grains that exhibit a crack-seal texture.

Mezger (1997, p. 21) interprets the muscovite-rich schist protolith was likely a "calcic shale, depleted in aluminum [and] interbedded with more aluminous layers." This interpretation is based on the disseminated appearance of graphite and the abundance of calcium-bearing minerals.

2.3.2.3 Biotite-rich Kluane schist

The biotite-rich Kluane schist, mapped as aluminous schist by Mezger (1997) due to its abundance of aluminum-bearing minerals, dominates the outcrop exposure of the Kluane schist (Figure 2). In the northwest, the biotite-rich schist mantles the muscovite-rich schist to the northeast and southwest and, the exposure appears to terminate near Burwash Flats. Between

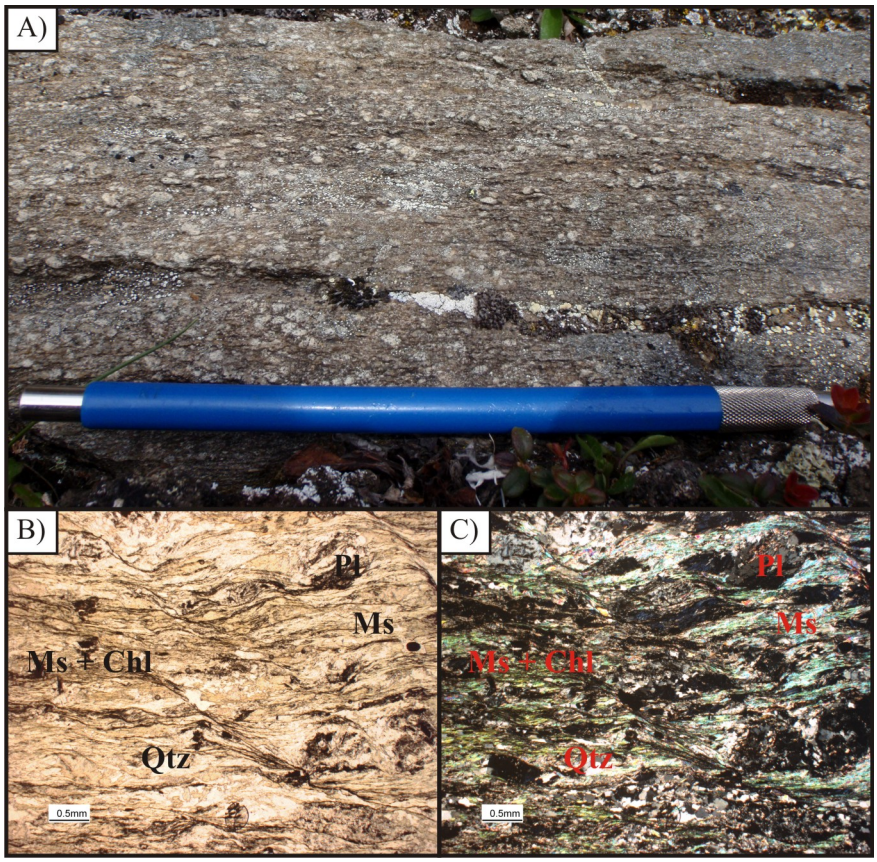

Figure 6: Macroscopic and microscopic textural morphology of muscovite-rich schist. A) Station 09-VLS-001 shows buff weathered grey muscovite-rich schist with mottled texture due to plagioclase porphyroblasts. B) Plane polarized light thin section photograph of muscovite-rich schist from station 09-VLS-136. Note the abundant opaque material disseminated throughout the section is graphite (Pl = plagioclase; Ms = muscovite; Chl= chlorite; Qtz = quartz). C) Corresponding crossed polarized light thin section photograph.

Shutdunmun Lake and Haines Junction, the map pattern of the biotite-rich schist is also convoluted similar to the muscovite-rich schist. This feature is due to contact metamorphism and regional scale folding. Further towards the southeast, the biotite-rich schist outcrops over a large area that, coupled with the cordierite-bearing gneiss, underlies the entire northern Dezadeash Range. South of this region, the voluminous, massive RRB is present.

Fresh surfaces of the biotite-rich schist typically retain a dark bluish-grey to blackish-grey appearance, while weathered surfaces appear dark grey to bluish-black (Figure 7A). Similar to the muscovite-rich schist, it is difficult to interpret geological features on the outcrop due to weathering and the abundance of lichen. Petrographic investigations indicate the biotite-rich schist is composed of medium to coarse grained plagioclase feldspar and garnet porphyroblasts and, fine to medium grained biotite + staurolite + andalusite + sillimanite + sericite + quartz + feldspar + spinel (± muscovite and chlorite; Figure 7B and C). Plagioclase and garnet

porphyroblasts are determined by electron microprobe studies to be oligoclase to andesine and almandine to spessartine in composition, respectively (Mezger, 1997). Garnet grains are present as two distinct phases: 1) Phase one garnet grains are represented by poikolitic porphyroclasts with quartz and feldspar inclusions that, in places, contain parallel spiral-shaped inclusion trails of graphite. This garnet phase is similar to the garnet grains observed in the muscovite-rich schist. The rims of the poikiolitic garnet porphyroclasts are typically corroded and altered to chlorite, sericite, and biotite (Mezger, 1997). 2) Phase two garnet grains are pristine, medium to coarse grained and inclusion-free porphyroblasts with sharp grain boundaries that truncate the dominant foliation in the surrounding matrix (Figure 7D and E).

The abundant fine grained opaque material observed in the feldspar and garnet porphyroblasts is graphite. Within plagioclase and garnet porphyroblasts graphite occurs as very thin, parallel inclusion trails. Texturally, graphite also appears disseminated throughout the biotite-rich schist. Quartz is less abundant in the biotite-rich schist compared to the muscovite-rich schist and it is typically anhedral in shape and fills the interstitial space between and/or forms layers between the other mineral phases. The transition between muscovite- and biotite-rich schist units is gradational.

Within the biotite-rich schist, a spaced cleavage is defined by a biotite-rich cleavage and quartz- and feldspar-rich microlithons. In places, the foliation is also defined by subordinate amounts of foliation parallel quartzofeldspathic igneous material. Notably, the quartz, feldspar, biotite, and hornblende within these layers is distinctly coarser grained than the same mineralogy found in adjacent cleavage domains. The dominant mineral aggregate and mineral stretching lineations are defined by elongate plagioclase and garnet porphyroblasts that intersect the dominant foliation surface and, elongate quartz and feldspar grains, respectively. Closer to the cordierite-bearing gneiss, the biotite-rich schist is coarser grained and the recognition of tectonic fabrics is obscured.

Mezger (1997, p. 21) interprets the biotite-rich schist protolith was likely a "homogeneous package of pelitic sediments." This interpretation is based on the disseminated appearance of graphite (*i.e.,* organic matter) and the abundance of aluminum-bearing mineral phases. Mezger (1997, p. 21) states "the similarity of the appearance and major mineral assemblage of the calcic and aluminous mica-quartz schist implies a similar depositional environment for both units with slightly different geochemical bulk composition of the source [rock]."

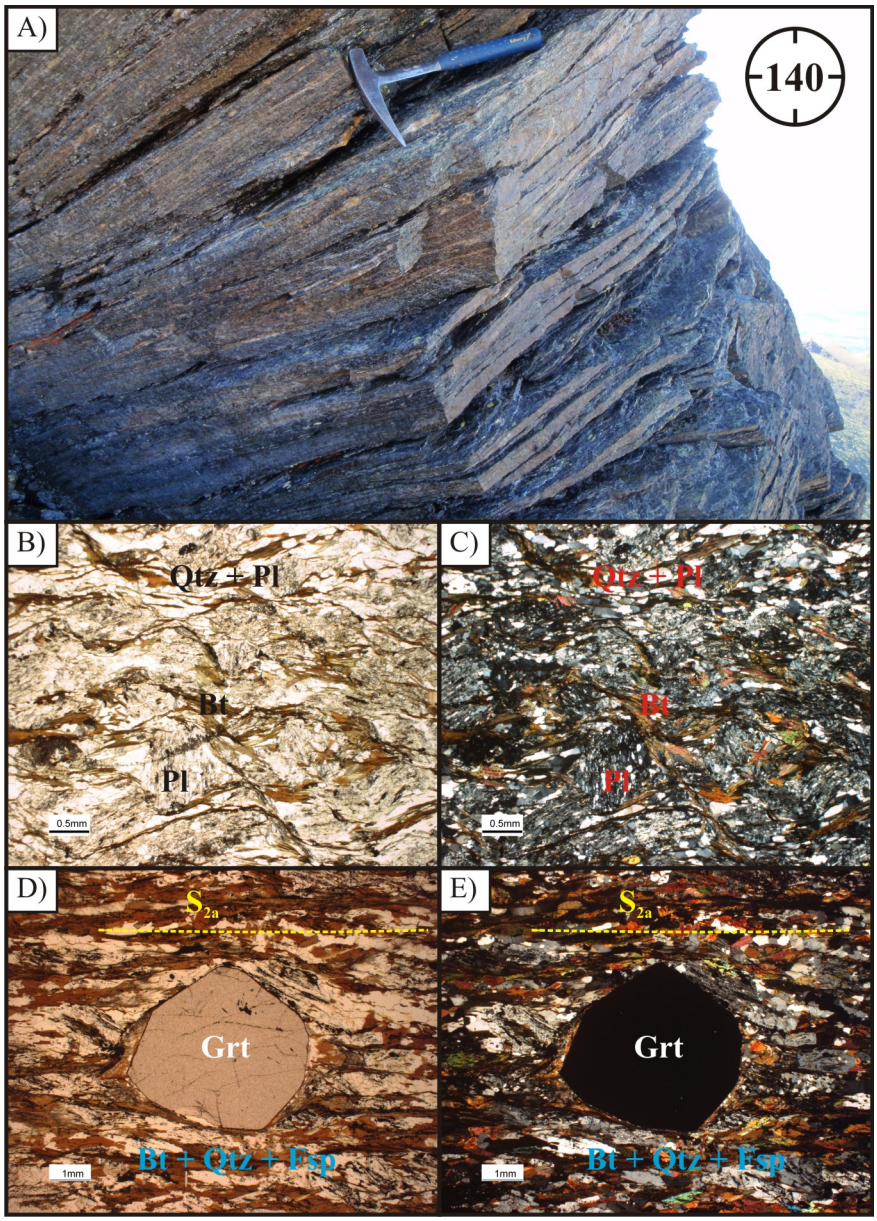

Figure 7: Macroscopic and microscopic textural morphology of biotite(± garnet)-rich schist. A) Station 10-VLS-145 shows weathered dark bluish-grey biotite-rich schist (looking 140°). B) Plane polarized light thin section photograph of biotite-rich schist from station 09-VLS-085 (Qtz = quartz; Pl = plagioclase; Fsp = feldspar; Bt = biotite; Grt = garnet). C) Corresponding crossed polarized light thin section photograph. D) Station 10-VLS-160 showing textural example of biotite(± garnet)-bearing contact metamorphic aureole rock-type associated with the syn- to post-kinematic Hayden Lake intrusive suite phases. Note the pristine grain boundaries of the garnet porphyroblast and also the truncation of S_{2a} against the garnet grain boundaries. E) Corresponding crossed polarized light thin section photograph.

2.3.2.4 Cordierite-bearing Kluane gneiss

In the eastern Ruby and Dezadeash ranges, the cordierite-bearing Kluane gneiss outcrops as a linear unit that parallels the Ruby Range batholith contact (RRB; Figure 2). In places, this

unit is spatially associated with foliated phases of the RRB, which are believed to represent the earliest intrusive phases of RRB (discussed in following section). Except for a section east of Gladstone Creek mouth, the gneiss is a continuous unit that pinches-and-swells, wherein it continually thins towards the northwest and thickens towards the southeast. The northernmost exposure of this unit is present along the western shores of Talbot Arm. In this region, the gneiss contains foliated RRB and deformed and metamorphosed carbonate horizons (Israel *et al.,* 2011a). Approximately 15 km southeast of Killermun Lake (Figure 2), the gneiss appears to be offset by approximately 7.5 km of right-lateral horizontal displacement. The nature of this intricate map pattern is discussed in detail in Chapter 3. The southernmost exposure of the gneiss is terminated by the relatively young and voluminous massive RRB.

The gneiss is distinguished from the adjacent biotite-rich schist and RRB by obvious luecocratic/melanocratic layering that dominates the outcrop texture (Figure 8A). The felsic layering is typically composed of coarse to very coarse grained quartz + feldspar + biotite + hornblende + cordierite. The melanocratic layering is generally composed of fine to coarse grained biotite + feldspar + quartz + garnet + graphite (Figure 8B and C). The melanocratic mineral assemblage (and texture) resembles the biotite-rich schist unit. The felsic layering typically retains a salt-and-pepper texture and/or a rusty-brown to pinkish-brown colour. Electron microprobe data by Mezger (1997) indicates the feldspar grains in the leucocratic layers are potassium feldspar. The contemporaneous growth of cordierite and potassium feldspar indicates a metamorphic origin for the two minerals (Mezger, 1997). This point is rather important since the melanocratic layers retain a similar texture and composition to that of the adjacent biotite-rich schist, indicating the gneiss is likely a higher metamorphic grade form of the biotite-rich Kluane schist. Tight asymmetric southwest vergent fold structures are observed in the gneiss.

The gneiss is texturally coarser grained than that of the proximal biotite-rich schist. This feature is relatively important since planar and linear tectonic fabrics that pre-date the coarsening of grain size are not well-preserved. Rarely preserved are rotated garnet porphyroclasts similar to those found in the muscovite- and biotite-rich schists indicating the three units likely shared a similar, early metamorphic evolution. Secondary biotite grains observed in the quartzofeldspathic and melanocratic layers overgrow the dominant foliation. Myrmekite texture observed in feldspar grains is common in the gneiss unit (Figure 8D and E). This texture is an intergrowth feature typically formed by igneous processes in granitic rocks, however, the texture can also form through metamorphic processes (Winter, 2001).

Mezger (1997) notes the presence of a orthoamphibole-biotite-plagioclase-quartz-rich schist within the gneiss in the eastern Dezadeash Range. The mineral assemblage, geochemistry, and

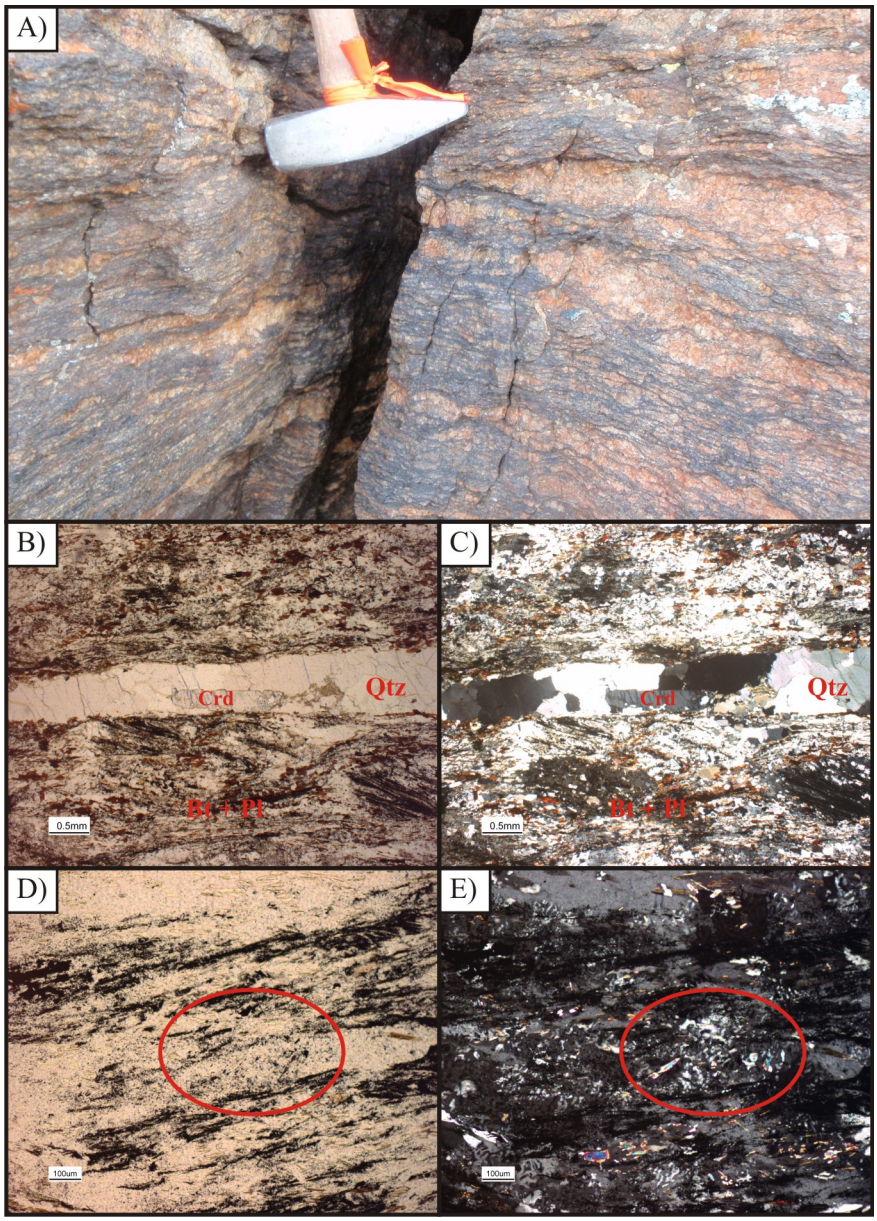

Figure 8: Macroscopic and microscopic textural morphology of cordierite-bearing gneiss. A) Example of outcrop texture observed where sample 10-VLS-262 was collected for U-Pb zircon LA-ICPMS (see Chapter 4). Note the quartzofeldspathic layer margins overgrow the dominant foliation plane of the melanocratic layers defined by the alignment of biotite and hornblende grains. B) Plane polarized light thin section photograph of cordierite-bearing gneiss from station 10-VLS-253 (Qtz = quartz; Pl = plagioclase; Bt = biotite; Crd = cordierite). C) Corresponding crossed polarized light thin section photograph. D) Plane polarized light thin section photograph of cordierite-bearing gneiss from station 10-VLS-294. Red ellipse indicates irregular 'wormy' blebs that represent an igneous intergrowth texture termed myrmekite. E) Corresponding crossed polarized light thin section photograph.

isotopic data of this unit indicates an andesitic composition and is more juvenile than the adjacent biotite-rich schist. Mezger (1997) notes that the contact and regional extent of this unit is unknown. The protolith for this layer is believed to be a metamorphosed sedimentary rock

derived from an andesitic source. Micro- and macroscopic structures and textures observed in this unit coupled with U-Pb detrital zircon LA-ICPMS analyses completed on a sample from this unit indicates the gneiss is genetically related to the Kluane schist wherein it represents the highest metamorphic grade portion of the schist.

2.3.3 Late Cretaceous to Paleocene - Ruby Range batholith (RRB)

All along the northeastern, eastern, and southern boundary of the Kluane schist lies the Late Cretaceous to Paleocene RRB (Figure 2). The batholith is regionally expansive and, it ranges in composition from quartz-diorite, tonalite, to granodiorite with subordinate amounts of diorite, gabbro, and granite (Figure 9; Israel *et al.,* 2011a). Texturally, it ranges from fine-grained to megacrystic and, it commonly retains a euhedral porphyritic texture. The RRB has a salt-and-pepper colour as the result of abundant euhedral hornblende and biotite grains (± magnetite) that, in places, makes up to 50 vol.% of the rock. Mezger (1997) indicates that subhedral to anhedral pyrope-almandine garnet grains exist in minor amounts close to the Kluane schist contact. Israel *et al.* (2011a) state the RRB composition is more felsic towards the north where it transitions into dominantly quartz-feldspar-porphyry of the Rhyolite Creek volcano-plutonic complex (see following section). This work also notes the presence of miarolitic cavities within the RRB in the northern region. Ellipsoidal, melanocratic enclaves composed almost entirely of biotite and hornblende are also present in the RRB. These enclaves have an aspect ratio up to approximately 4 : 1 with a long axis typically not exceeding 40 cm.

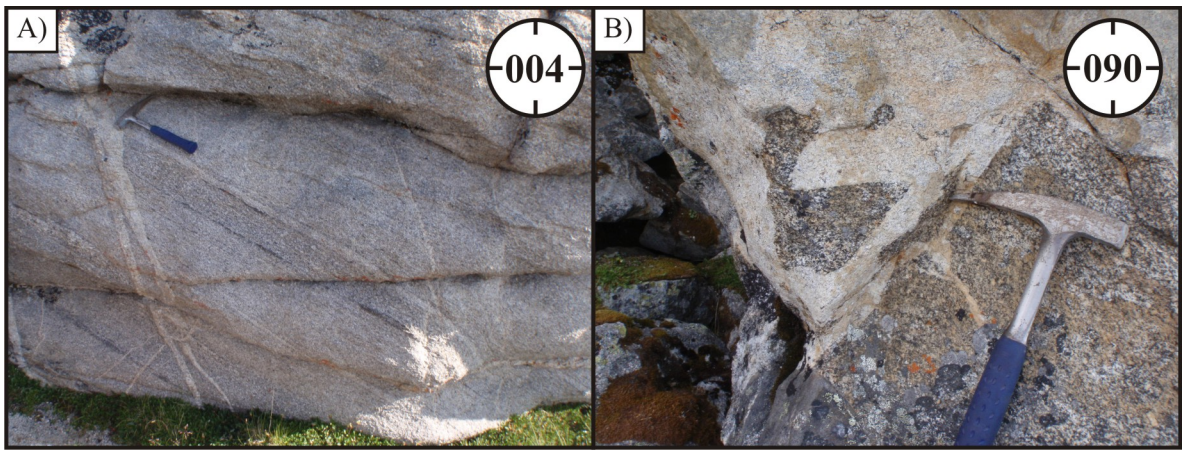

Figure 9: Textural and compositional variations of the Ruby Range batholith. A) Foliated salt-and-pepper biotite-hornblende-tonalite cross-cut by thin leucocratic quartzofeldspathic dykes (station 09-VLS-101 looking 004°). B) Leucocratic biotite-tonalite intruding melanocratic biotite-hornblende-granodiorite (station 09-VLS-095 looking 090°).

On a regional scale, the RRB is a composite body of massive and foliated exposures (Figure 9) wherein foliated exposures are more commonly found in close proximity to the RRB-

Kluane schist contact. The orientation of the foliated exposures is parallel to the structurally lower northeast-dipping biotite-rich Kluane schist. Conversely, massive RRB phases increase in abundance away from the Kluane schist contact. The foliated RRB units represent the structural base of the RRB. The foliation is defined by the alignment of hornblende and biotite grains; however, in places, this fabric is also defined by compositional layering of felsic and mafic accumulations. The planar fabric defining elements are typically undeformed phenocrysts; however, a strong gneissosity is commonly observed and could be of tectonic origin. Where exposures are deemed adequate, the planar fabric forming elements may also be measured as linear features. As noted above, the RRB contains ellipsoidal melanocratic biotite-hornblende-bearing enclaves. When present in the foliated RRB phases, the long axis of these enclaves are oriented parallel to the linear phenocryst alignment. These enclaves indicate an incomplete mixing of the RRB magma chamber during crystallization (Winter, 2001). Israel *et al.* (2011a) interpret the presence of foliated RRB phases along the Kluane schist-RRB contact and, the lack of foliated RRB exposures to the north as the result of localized strain accumulation that was focused towards the base of the RRB during emplacement. Rarely, foliated RRB rocks are found within the Kluane schist as sills oriented parallel to the dominant foliation of the host schist. These sill-like bodies also appear as deformed, fold structures. Massive, non-foliated phases dominate the exposed RRB bedrock. These phases truncate and cross-cut the Kluane schist, gneiss, and foliated RRB units.

Magnetic geophysical surveys flown in early 2010 by the Geological Survey of Canada define anomalous portions of the RRB that are relatively more or less magnetic thereby defining distinctly different intrusive phases of the RRB (see appendix A). This study and Israel *et al.* (2011, with references therein) record U-Pb zircon ages for the RRB from *ca.* 77 to 57 Ma. Field relationships indicate that the felsic, massive phases are relatively younger and mafic/intermediate, foliated phases are relatively older (Figure 9B). Mezger (1997) notes the relative age and textural relationships are similar to tonalites of the Great tonalite sill in southeastern Alaska. This point is important for mineral exploration within the current study area since the Alaskan equivalent represents a mineral exploration analogue that Yukon Territory exploration companies could exploit (*i.e.,* Juneau Gold Belt; Israel *et al.,* 2011a). U-Pb zircon age determinations of a deformed leucocratic tonalite dyke collected for the current study provide a lower age constraint for the earliest phases of the RRB at *ca.* 77 Ma (discussed in detail in Chapter 4). A fine-grained boudinaged biotite-granitic dyke that cross-cuts the gneiss near the Alaska Highway-Aishihik River intersection reported by Israel *et al.* (2011a) yields concordant U-Pb zircon igneous ages at *ca.* 71.8 ± 0.2 to 68.4 ± 0.2 Ma (Mezger, 1997; Mortensen, unpublished data). Israel *et al.* (2011a) interpret these igneous ages are related to pre-main stages of RRB emplacement plutonism. However, the RRB is likely a composite

body that, with more age constraints, could likely be subdivided into various magmatic events. The RRB is interpreted as a composite syn-tectonic/syn-metamorphic batholith that intruded from approximately *ca.* 77 to 57 Ma, however, it is likely that this age bracket could increase given the significant amount of RRB-like rocks whose age remains unknown.

2.3.4 Early Paleogene - Rhyolite Creek volcano-plutonic complex (RCC)

The RCC outcrops almost entirely north of the current study area adjacent the northeastern exposure of the expansive RRB. Compositionally, volcanic rocks of the RCC range from "intermediate volcanic flows, breccia and tuff, flow-banded rhyolite and felsic tuff, and rare mafic flows, breccia and tuff" (Israel *et al.,* 2011a, p. 109). Porphyritic rocks are common in the RCC and, they generally retain smokey blue quartz phenocrysts with subordinate amounts of smokey white plagioclase phenocrysts up to 1 cm in diameter (Figure 10).

Figure 10: Layered quartz-feldspar-porphyry dyke of the RCC (station 10-VLS-066 looking 300°).

North of the current study area, where the archetypical RCC is observed (*i.e.,* proximal to Rhyolite Creek), the RCC outcrops as kilometer scale exposures cross-cutting RRB and Yukon-Tanana terrane (YTT) rocks. Within the current study area, RCC is observed in only a few places and it always cross-cuts all tectonic fabrics of the Kluane schist and RRB. In these exposures, RCC is represented by porphyritic phases with variable amounts of quartz and feldspar phenocrysts. These exposures are small (*i.e.,* typically 1 m thick and tens of meters in strike length) vertically dipping, discontinuous dykes with variable strike orientations. Israel *et al.* (2011a) state the porphyritic phases, in places, intrude the overlying volcanic units of the RCC. That same study indicates volcanic and plutonic units of the RCC both yield ages of *ca.* 57 Ma thereby confirming their contact relationships, which implies they were emplaced contemporaneously (Crowley and Murphy, unpublished data). The RCC is a composite post-tectonic unit that is observed in only a few places throughout the current study area as cross-

cutting dykes.

The RCC is referred to by Israel *et al.* (2011a) as a volcano-plutonic complex that equates to the youngest known porphyritic phase of the RRB. Coupled with miarolitic cavities observed in the northern RRB exposures and the more felsic composition of the RRB in the north, the RCC likely represents the structurally highest and stratigraphically youngest portion of a broad, composite intrusive body.

2.3.5 Middle Paleogene - Hayden Lake intrusive suite (HLIS)

The HLIS outcrops throughout the central portion of the study area as diorite to quartz-diorite units (Figure 2) that are rarely associated with medium to coarse grained gabbro. The former units commonly contain fine to medium grained euhedral phenocrysts of biotite and muscovite (± hornblende). Texturally, this unit is dominantly massive although strong planar fabrics are observed in some exposures close to the contact with the Kluane schist (discussed in detail in Chapter 3). These planar fabrics are defined by the alignment of biotite and hornblende as well as a compositional layering between mafic and felsic minerals. Israel *et al.* (2011b) state the HLIS commonly contains garnet crystals up to 1 cm in diameter. Texturally, the HLIS ranges from salt-and-pepper to leucocratic (Figure 11).

Figure 11: Massive leucocratic biotite-muscovite-bearing tonalite (± hornblende) of the HLIS (station 09-VLS-129 looking 180°).

On a regional scale, the *ca.* 55 to 48 Ma HLIS typically manifests itself as kilometer scale intrusive bodies that are both conformable and non-conformable with all planar and linear fabrics observed in the schist. In places, the dominant foliation of the Kluane schist

appears sub-parallel to foliated phases of the HLIS. The metamorphic signature of the Kluane schist that surrounds the HLIS exposures indicates contact metamorphism parallel to the HLIS bedrock boundaries. These metamorphic aureoles, in places, are both concordant and discordant with the dominant foliation of the host schist and therefore, the HLIS is likely a late-syn- to post-tectonic magmatic feature.

2.4 Regional tectonic framework

2.4.1 Introduction

Using a multidisciplinary database, Nelson and Colpron (2007, p. 758) state the northern Cordillera consists of five major entities that are collectively composed of various minor terranes (Figure 1). The major entities include: 1) parautochthonous Laurentia (ancient North America); 2) oceanic terranes; 3) the allochthonous marginal peri-cratonic terranes [Intermontane terrane; Yukon-Tanana terrane (YTT)]; 4) the exotic Arctic Alaska and Insular terranes; and 5) Mesozoic and younger arc and accretionary terranes that neighbor the western and southern fringe of the older elements. The following section serves to highlight the order of events leading to the inception and assembly of the major entities with emphasis on southwest Yukon Territory.

2.4.2 Laurentia and its associated western, accreted terranes: Early Paleozoic to present

Along trend of the present day northern Cordillera and overlying Proterozoic sedimentary units (not discussed here) are the long-lived Paleozoic Selwyn Basin and Kootenay terrane. Both the Selwyn Basin and Kootenay terrane host Cambrian mineralization associated with sedimentary exhalative and massive sulphide deposits, respectively (Figure 1). The Selwyn Basin and Kootenay terrane are believed to have formed through intracontinental rifting given the strong evidence for contemporaneous subsidence and extension (Nelson and Colpron, 2007).

Following Cambrian to Silurian synchronous extension and mineralization, Middle Devonian compression ensued and was followed closely by Early Mississippian extension. This change in tectonics is preserved by: 1) Middle Devonian to Late Mississippian bimodal arc-related magmatism. The felsic components exhibit a continental crustal influence, while the mafic components vary from arc tholeiite, calc-alkaline, MORB (Mid-Ocean Ridge Basalt), E-MORB (enriched-MORB), OIB (Ocean Island Basalt), boninite, and BABB (back-arc basin basalt; Piercey *et al.,* 2006; Nelson and Colpron, 2007). Detrital zircon populations and isotopic signatures suggest that although the felsic and mafic magmatic phases are arc-derived,

they were developed on an attenuating Laurentian continental margin. This period of events is believed to be responsible for inception of the peri-cratonic frontal YTT arc to the west and the cratonic margin to the east. 2) Almost simultaneously, Early Mississippian time is represented by the birth of Slide Mountain Ocean. The opening of this ocean is responsible for completely separating YTT from Laurentia's western continental margin (Figure 12; Monger and Price, 2002; Nelson and Colpron, 2007). Slide Mountain Ocean outcrops in the northern Cordillera as discontinuous slivers and slices of the Slide Mountain oceanic terrane (Figure 1).

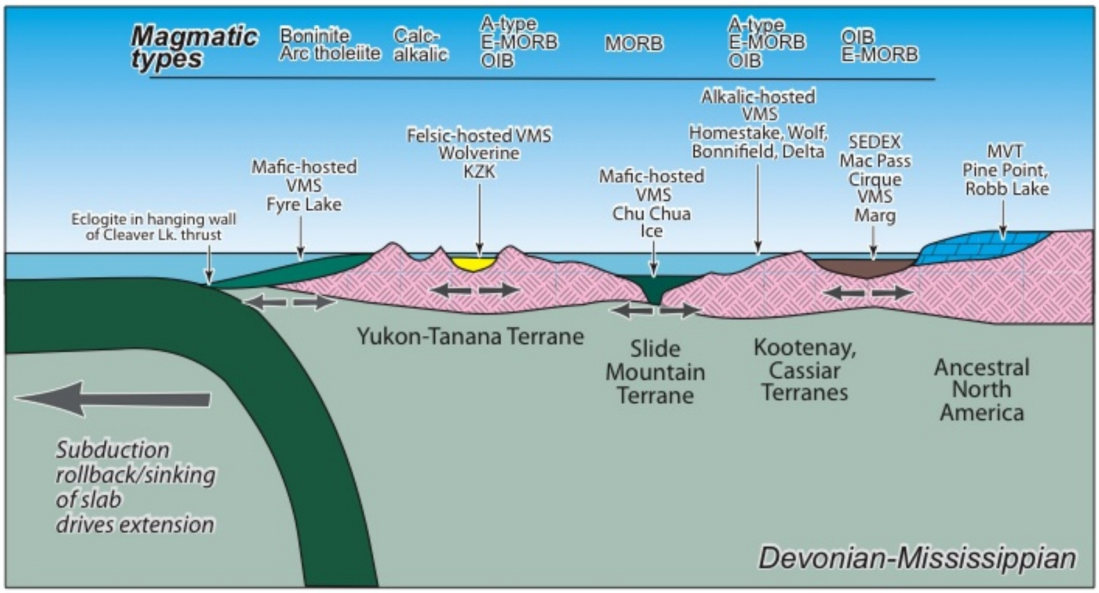

Figure 12: Schematic cross-section of western Laurentian margin from Devonian to Mississippian. Tectonic settings are interpreted based on the variation in magmatic styles and associated economic deposit types. Adapted from Nelson *et al.* (2006) and by Nelson and Colpron (2007).

Throughout the Late Paleozoic to Early Mesozoic, arc magmatism continued to build upon YTT (Colpron *et al.,* 2006; Nelson *et al.,* 2006); however, volcanism changed from bimodal to intermediate and lesser enriched basalts (Piercey *et al.,* 2006). The Mesozoic volcanic strata of Stikine and Quesnel terranes record this variation in volcanism. As well, Triassic/Jurassic sedimentary units and intrusive bodies that are present in and overlying YTT, Quesnel, and Stikine terranes confirm the relationship of continued arc magmatism. YTT, Quesnel and Stikine terranes combine to form the Intermontane terrane.

Pennsylvanian to Early Permian faunal affinities and voluminous basaltic magmatism, coupled with the lack of significant sedimentation on Slide Mountain oceanic terrane indicates that a broad ocean separated Laurentia from the Intermontane terrane during Early to Middle Permian time (Nelson *et al.,* 2006). The significant syngenetic sulphide mineralization prior to this time period was nearly diminished in the Permian, suggesting that Late Paleozoic continental margin tectonics was more subdued. Nelson and Colpron (2007, p. 769) state that

this time frame officially marks the end of continental rifting in the peri-Laurentian realm.

The peri-cratonic Intermontane terrane was eventually accreted to Laurentia as a result of Slide Mountain Ocean closure. The consumption of this broad ocean was initiated by west directed subduction underneath YTT in the Middle to Late Permian. Consequently, felsic continentally-derived magmatic rocks coupled with a belt of coeval high-pressure metamorphic rocks and growth strata wedges appear within and adjacent to the eastern side of YTT. Remnants of Slide Mountain Ocean were subsequently thrust on the eastern portion of YTT (Figure 1). A geochronological study shows that YTT detrital zircon grains occur in Triassic strata in Yukon. This suggests that YTT arrived near its present position in the Triassic (Beranek and Mortensen, 2006).

The Intermontane terrane was initially attached on its outer oceanward margin by Cache Creek terrane, an accretionary assemblage of Late Paleozoic to Lower Jurassic blocks of limestone and blueschist rocks that structurally intervenes between Quesnel and Stikine terranes (Figure 1; Colpron *et al.,* 2007). Cache Creek terrane contains Permian faunal evidence of an exotic, Tethyan (Asian) affinity indicating Intermontane terrane migrated from west to east during Slide Mountain Ocean closure (Ross and Ross, 1983). Given that Cache Creek terrane structurally intervenes between Quesnel and Stikine terranes, coupled with Triassic/Jurassic fore-arc facies in Quesnel terrane and Jurassic fore-arc facies in the Stikine terrane suggests that both Quesnel and Stikine terranes were opposing fore-arcs as the result of a subducting ocean that hosted Cache Creek terrane (Figure 13A; Mihalynuk *et al.,* 1994). Cache Creek terrane was eventually trapped between Quesnel and Stikine terranes in the Middle Jurassic as Stikine terrane accreted to Quesnel terrane. During Middle Jurassic time, arc magmatism in both Quesnel and Stikine terranes ceased. Following entrapment of Cache Creek terrane, portions of it were eventually obducted onto the northeastern side of Stikine terrane (Mihalynuk *et al.,* 2004).

The Insular (Alexander and Wrangellia terranes), Farewell, and Arctic Alaska terranes exhibit no evidence of an early relationship with Laurentia. This point is relatively important given the terranes are peri-cratonic in nature and have a long-lived history (Precambrian to Triassic; Colpron *et al.,* 2007). Alexander terrane is a composite crustal fragment composed of Precambrian to Early Paleozoic arc volcanic rocks and continental shelf/platform strata. The Wrangellia terrane is composed of similar rock although it is a relatively younger terrane (Middle to Late Paleozoic; Nelson and Colpron, 2007). Both terranes share similar Late Paleozoic arc-derived magmatic cover and voluminous accumulations of Triassic non-arc derived flood basalt cover. The Farewell terrane is composed of Proterozoic basement rocks with overlying Paleozoic shelf and slope strata and Permian clastic wedge deposits. Faunal and isotopic

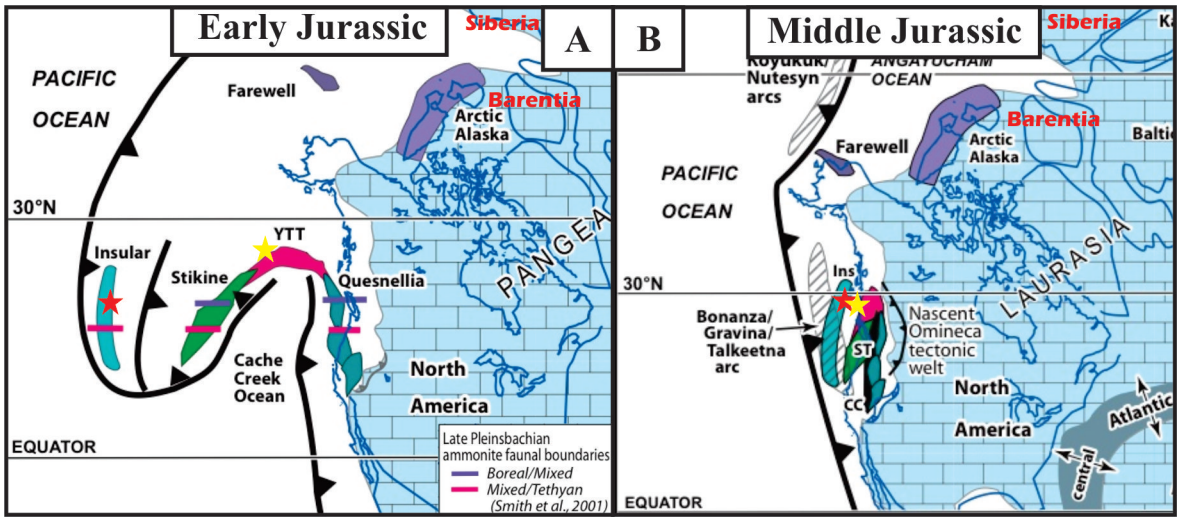

Figure 13: Schematic tectonic reconstructions of A) western Pangea during the Early Jurassic and B) western Laurentia during the Middle Jurassic. Note red text indicates location of Barentia and Siberia. Yellow and red stars indicate hypothetical location of future Kluane schist and Dezadeash Formation protoliths, respectively. Adapted from Mihalynuk *et al.* (1994) with references therein (CC - Cache Creek Terrane; Ins - Insular Terrane; ST - Stikinia Terrane). By Nelson and Colpron (2007).

studies indicate Insular and Farewell terranes are derived from either Siberia or Barentia (see bold red text in Figure 13A and B; Bazard *et al.,* 1995; Nokleberg *et al.,* 2000; Bradley *et al.,* 2003; Nelson and Colpron, 2007). The Arctic Alaska terrane is not associated with western Laurentia. Stratigraphy similar to the Russian Far East is recognized in rocks of this terrane indicating that Arctic Alaska and the Russian Far East were adjacent one another throughout most of their history (Miller *et al.,* 2006). The Insular, Farewell, and Arctic Alaska terranes are all regarded as a set of detached crustal fragments and, along with ensuing Paleozoic and Mesozoic arc-derived magmatic rocks and sedimentary cover, developed for the most part within the Arctic realm (Nelson and Colpron, 2007).

Intermontane terrane accreted to Laurentia as early as Middle Jurassic time (Figure 13). Almost simultaneously, Arctic Alaska/Insular terranes were impinging on the outer fringes of Intermontane terrane. Nelson and Colpron (2007) infer that collision of Arctic Alaska/Insular and Intermontane terranes with Laurentia are related. Substantial evidence exists to warrant the interpretation that the amalgamation and inception of the Cordilleran Orogen coincides with opening of the Atlantic Ocean (*ca.* 170 Ma). In southeastern Alaska, collision of the Insular and Intermontane terranes is constrained by $162 - 139$ Ma dykes that crosscut a ductile fault system that separates Alexander terrane from the underlying YTT. In the same region, Middle Jurassic volcanic rocks and Upper Jurassic/Lower Cretaceous strata overlie the contact of the Insular and Intermontane terranes (Nelson and Colpron, 2007). Faunal and flora evidence in the Insular and Intermontane terranes suggests both terranes were impinging on the outer

fringes of Laurentias continental margin during the Early Jurassic (see inset in Figure 13A). In British Columbia and southeast Alaska, this boundary is recognized by the juxtaposition of Alexander and Wrangellia terranes with YTT. In Yukon, approximately 100 km NNW of the current study area, oceanic crust of Windy-McKinley[2] terrane separates Alexander and YTT. Murphy *et al.* (2009) present trace-element geochemical evidence indicating the original tectonic setting of the Windy-McKinley terrane was likely an east-dipping (present day coordinates) supra-subduction zone setting. Deformed ophiolitic ultramafic rocks observed throughout the current study area could represent the southernmost exposure of oceanic crust associated with this supra-subduction zone. Nelson and Colpron (2007) use the above evidence to show collision and amalgamation of the Insular and Intermontane terranes to Laurentia was closely linked to opening of the Atlantic Ocean and westward migration of the North American plate.

After Middle Jurassic accretionary events of the Arctic Alaska/Insular and Intermontane terranes to Laurentia, various large-magnitude continental-arc-derived magmatic intrusions pierced and stitched together the northern Cordillera. These intrusions were contemporaneously imposed on west-vergent structures that resulted from the westward migration of the North American plate towards the east-dipping subduction zone (Murphy *et al.,* 1995; Gibson *et al.,* 2005; Colpron *et al.,* 2006; Nelson and Colpron, 2007). The evolving northern Cordillera eventually became a host to a vast majority of Late Jurassic through Tertiary epigenetic mineral deposits (*e.g.,* Ag, Au, Cu, Mo, and W). These deposits are delineated along, and adjacent to large (*i.e.,* 100's of kilometers long and 10's of kilometers wide), linear magmatic bodies such as the *ca.* 175 to 150 Ma Nelson plutonic suite of southern British Columbia and the *ca.* 120 to 37 Ma Coast plutonic complex of Yukon and British Columbia (*i.e.,* Ruby Range batholith, Rhyolite Creek volcano-plutonic complex, and Hayden Lake intrusive suite). Voluminous Early to mid-Cretaceous (*ca.* 115 to 90 Ma) and Late Cretaceous (*ca.* 78 to 72 Ma) magmatism reflects an active northeast dipping subduction zone underneath North America. However, the relatively younger Late Cretaceous magmatic flux is geochemically complex and possibly related to arc magmatism followed closely by lithospheric delamination associated with the emplacement of contemporaneous arc-like and mantle derived 'plume-like' magmatic signatures (Mortensen and Hart, 2010). The location and east directed younging of these magmatic belts represents a subduction related arc-trench gap migration towards the east (Nelson and Colpron, 2007). Towards the waning stages of arc magmatism (*i.e., ca.* $<$ 37 Ma), synchronous volcanism and crustal extension resulted in the exhumation of metamorphic core complexes and approximately 400 to 500 km of dextral motion accommodated along the Tintina, Fraser,

[2]Murphy *et al.* (2009, p. 195) states the assignment to Windy-McKinley terrane is obsolete, however, a new name has not been assigned yet.

and Denali faults. Epithermal mineral deposits continued to form as mineralizing fluids were channeled upward along the pre-existing faults during this time period. Subsequently, arc magmatism has all but ceased since subduction along the west coast of Canada has been translated into dextral transcurrent faulting along the Queen Charlotte fault (Figure 1).

The amalgamation of most of the present day northern Cordillera was nearly complete by Middle Jurassic time. However, the present day morphology of the northern Cordillera is likely quite different from its initial inception. With the birth of the Atlantic Ocean and westward migration of the North American plate, large-scale deformation and arc-magmatism overprinted the northern Cordillera. However, how the sedimentary basins that existed between Insular and Intermontane terranes evolved from the Late Mesozoic through to the Cenozoic still remains enigmatic.

3 Structural geology

3.1 Introduction

A large structural data-set was collected over the course of this study. Consequently, four distinct generations of structures are recognized in the Kluane schist based on foliation and fold overprinting relationships. Primary sedimentary features are rarely preserved in the Kluane schist due to the relatively large amount of bulk strain that has accumulated in the rocks. When present, the sedimentary attributes are preserved in areas of relatively low bulk strain. At the outcrop scale, these features typically manifest themselves as massive quartz-rich (± chlorite) layers up to 1 m thick that are hosted within thick, homogeneous, foliated mica-quartz-rich layers (biotite and/or muscovite ± hornblende; Figure 14). This contrast in composition is interpreted to represent metamorphosed sandstone layers [*i.e.,* psammite // S_o; S_n of Mezger (1997)] interlayered between deformed and metamorphosed quasi-mudstone layers (*i.e.,* semi-pelite to pelite). Structures formed later in the evolution of the schist have obliterated any recognition of younging direction. The structural and textural attributes of the four generations of structures are summarized below.

3.2 D_1 - Bedding parallel foliation development

Structures associated with the earliest recorded deformation event [D_1; D_{n+1} of Mezger (1997)] are pervasive in the Kluane schist. The D_1-related planar fabric is defined microscopically by graphitic inclusion trails [S_1; S_{n+1} of Mezger (1997)] preserved within D_2-related plagioclase and garnet porphyroblasts (Figures 15 and 16). S_1 crenulations within the porphyroblasts represent the oldest fold generation (F_2) preserved within the schist (Figure 15B). Macroscopically, S_1 is a bedding parallel foliation defined by the alignment of decimeter thick metamorphosed quartz-rich layers interpreted as metamorphosed psammite layers (± chlorite; Figure 14). As well, S_1 is defined by the alignment of biotite, muscovite, hornblende, and/or chlorite outside the quartz-rich layers. S_1 is parallel to a well-developed composite S_{2a} spaced cleavage associated with a succeeding deformation event (see S_{2a} in Figure 14).

Rarely, S_1 within porphyroblasts is observed gradually curling into the exterior S_1 demonstrating re-crystallization associated with the respective porphyroblast strain cap. In relation to the surrounding mica-rich matrix, mantles also associated with these porphyroblasts indicate a re-arrangement of quartz + biotite + plagioclase + hornblende grains in response to a progressive inhomogeneous deformation event (Passier and Trouw, 2005). Spiral-shaped S_1 inclusion trails infrequently preserved within garnet porphyroblasts indicate syn-kinematic

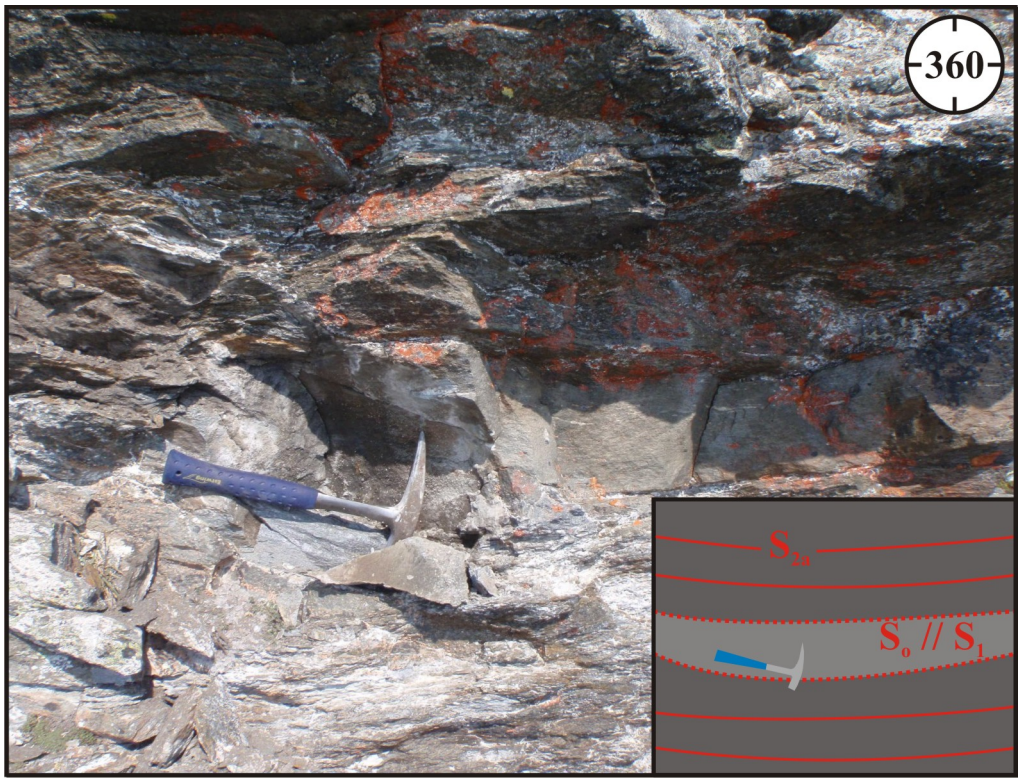

Figure 14: Station 09-VLS-092 exhibiting the distinction between massive quartz-rich layers (enclosed in red dashed line of inset image; S_o) and foliated mica-quartz-rich layers (looking 360°). Note that S_o is a bedding parallel foliation (S_1) that is also parallel to a well-developed S_{2a} spaced cleavage. Quartz-rich layer proximal to rock hammer was sampled and analyzed for U-Pb zircon LA-ICPMS (see Chapter 4 for details).

porphyroblast growth post-D_1 (Figure 16A; Passier and Trouw, 2005).

3.3 D_2 - Main tectonometamorphism of the Kluane schist

3.3.1 Introduction

D_2 (D_{n+2} of Mezger, 1997) represents the main tectonometamorphic phase of the Kluane schist. It is defined here as a composite, progressive deformation event. Although less intense post-D_2 structures have overprinted the schist, micro- to macroscopic structures related to D_2 are ubiquitous. The intensity of D_2-related planar and linear fabric elements as well as the intensity of metamorphism are regionally variable; however, D_2 intensity generally increases towards the northeast where the schist is intrafoliated with deformed ultramafic and Yukon-Tanana terrane (YTT) rocks. At the northeastern exposure of the Kluane schist, within a cordierite-bearing gneiss subunit, D_2 intensity is cryptic due to the significant amount of syn- to post-tectonic recrystallization associated with emplacement of the Ruby Range batholith (RRB). Micro- to mesoscopic D_2 structures and the D_2-related metamorphic signature of the

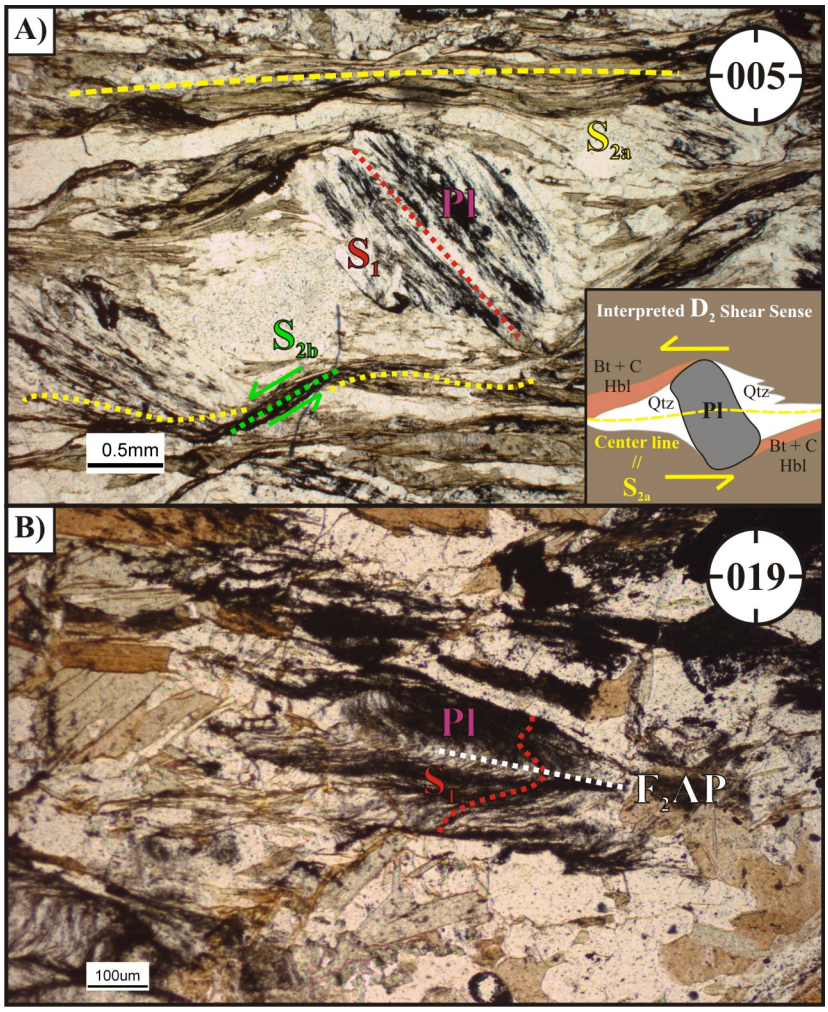

Figure 15: Textural examples of S_1 within plagioclase porphyroblasts (Pl). Plane polarized transmitted light photographs of thin sections oriented parallel to lineation (L_2) and perpendicular to dominant exterior foliation (S_{2a}). A) Station 09-VLS-055 exhibiting parallel orientation of S_1 in an asymmetric σ-type mantled porphyroblast resulting from a broadly east-over-west D_2 shearing event (looking 005°). S_{2a}, S_{2b}, and inset image indicate east-over-west shear sense of progressive D_2 deformation event (Qtz = quartz; Bt = boitite; Hbl = hornblende; C = graphite). B) Station 10-VLS-265 showing S_1 crenulated into microscopic-scale F_2 folds (F_2AP = F_2 axial plane; looking 019°). S_1 is truncated at a high angle to S_{2a} (oriented parallel to long edge of photograph) and the Pl grain boundary.

schist constrain the architecture and regional scale map pattern.

3.3.2 Micro- to macroscopic D_2 structures

Microscopically, the D_2 planar fabric is locally a crenulation cleavage inside plagioclase and garnet porphyroblasts that is pervasively differentiated into a fine grained spaced cleavage outside the porphyroblasts (S_{2a}; Figure 17). In areas of high D_2 strain, microscopic scale shear zones are oriented at a slightly oblique angle to S_{2a}. These microscopic shear zones define a

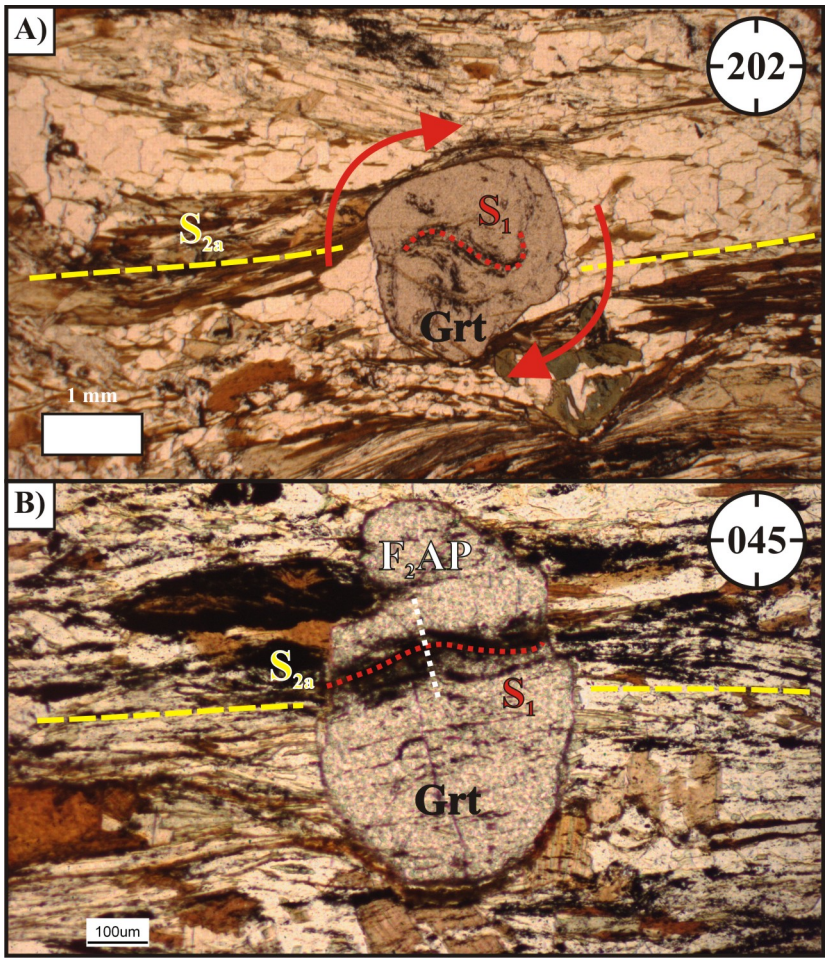

Figure 16: Textural examples of S_1 within garnet porphyroblasts (Grt). Plane polarized transmitted light photographs of thin sections oriented parallel to lineation (L_2) and perpendicular to dominant exterior foliation (S_{2a}). A) Station 10-VLS-194 showing spiral-shaped S_1 inclusion trails (looking 202°). Following S_1 development, the porphyroblast grew during a progressive clockwise, east-over-west rotation (red arrows). Note the Grt grain boundaries truncate S_{2a}. B) Station 10-VLS-294 showing a porphyroblast that grew post-crenulation of S_1 (see F_2AP; looking 045°).

C′-S fabric labelled herein as S_{2a} (S) and S_{2b} (C′; Figure 18). Both of these planar fabrics are defined by the alignment of biotite, muscovite, hornblende, and/or chlorite (± graphite; Figure 17 and 18). Within S_{2a}, micas and hornblende form the cleavage and re-crystallized quartz (± plagioclase) grains the microlithons. S_{2b} is consistently oriented at an angle $\leq$ 45° to S_{2a} and, it slightly deflects the orientation of S_{2a} wherein small amplitude folds of S_{2a} are preserved (Figure 15A and Figure 18). S_{2b} retains a consistent northeast-over-southwest sense of shear.

S_{2a} is parallel to the axial plane of micro- to macroscopic tight to isoclinal F_2 fold structures (Figure 19, 20, and 21). These fold structures appear as centimeter scale rootless intrafolial folds and micro- to macroscopic symmetric M-shaped and asymmetric S- and Z-shaped folds.

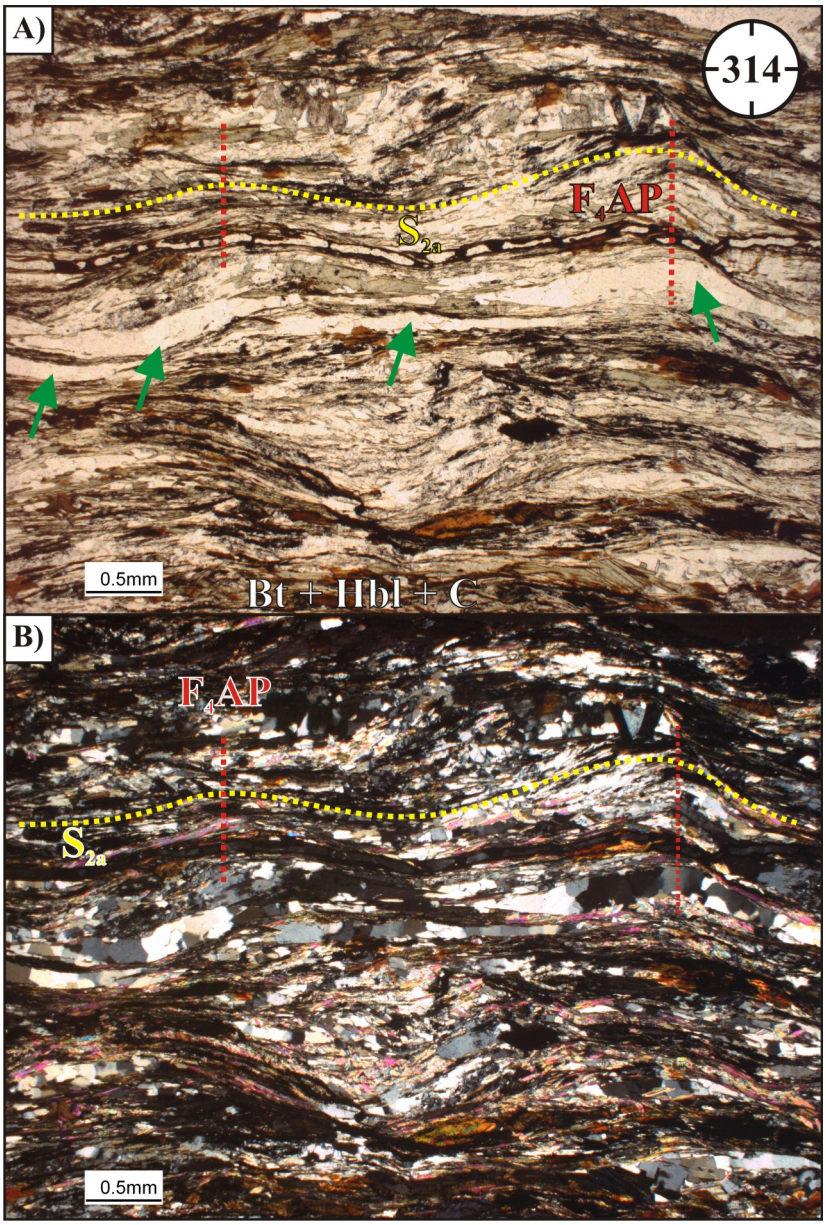

Figure 17: Station 10-VLS-264 exhibiting an example of penetrative spaced cleavage (S_{2a}). Transmitted light photographs of thin sections oriented perpendicular to lineation (L_2) and S_{2a} (looking 314°). A) Plane polarized photograph with green arrows indicating the location of lensoidal-shaped, boudinaged quartz-rich microlithons. Cleavage domains are defined by the alignment of biotite, hornblende, and graphite (Bt + Hbl + C). Yellow dashed line indicates the trace of crenulated S_{2a}. Red dashed line exhibits the trace of F_4AP (F_4 axial plane). B) Corresponding cross polarized photograph.

These folds are defined by the trace of S_o, S_1, and/or deformed pre- to syn-D_2 quartz-rich veins (discussed in following section). Where F_2 folds are completely isoclinal, S_{2a} represents the complete transposition of older foliations (*i.e.,* S_o, S_1, and quartz veins) into a composite S_{2a} transposition foliation. F_2 folds commonly exhibit both northeast-over-southwest and southwest-over-northeast vergence, which relates to the geometry of the regional scale F_2 fold

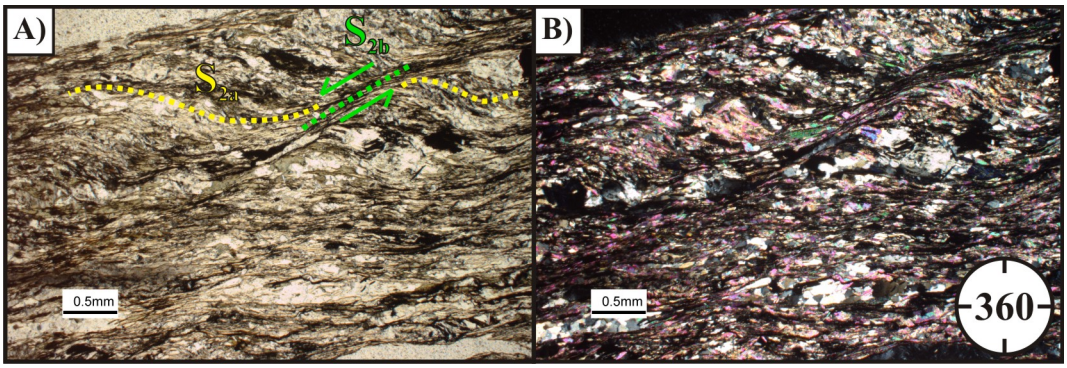

Figure 18: Station 09-VLS-063 exhibiting an example of C′-S fabric in the muscovite-rich schist. Transmitted light photographs of thin sections oriented perpendicular to lineation (L_2) and S_{2a} (looking 360°). A) Plane polarized photograph with green arrows indicating the sense of shear associated with the development of C′. Yellow dashed line indicates trace of S (*i.e.*, S_{2a}).

structure (discussed later). Open to tight microscopic F_2 folds observed wthin D_2-related porphyroblasts represents the earliest evidence of F_2 (Figure 15B and 16B).

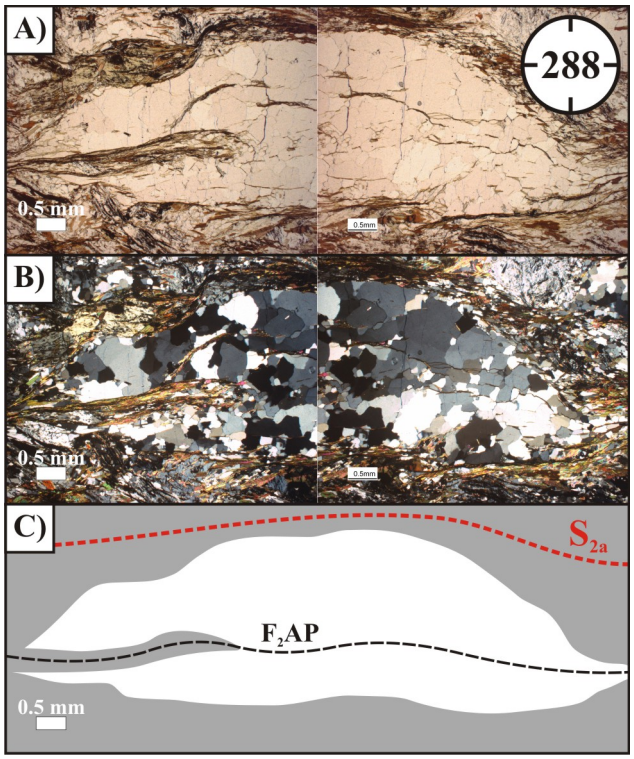

Figure 19: Station 10-VLS-265 showing an example of a microscopic isoclinal F_2 fold. Thin section is oriented perpendicular to S_{2a}. A) Plane polarized transmitted light photograph looking 288°, B) cross polarized transmitted light photograph, and C) schematic drawing of isoclinal F_2 fold structure with a well-developed S_{2a} axial planar cleavage (F_2AP = F_2 axial plane) that exhibits the complete transposition of a highly deformed pre-D_2 quartz vein.

In areas of relatively low strain, deformed plagioclase and garnet porphyroblasts are preserved in the microlithons. Plagioclase porphyroblasts regularly retain asymmetric, stair-

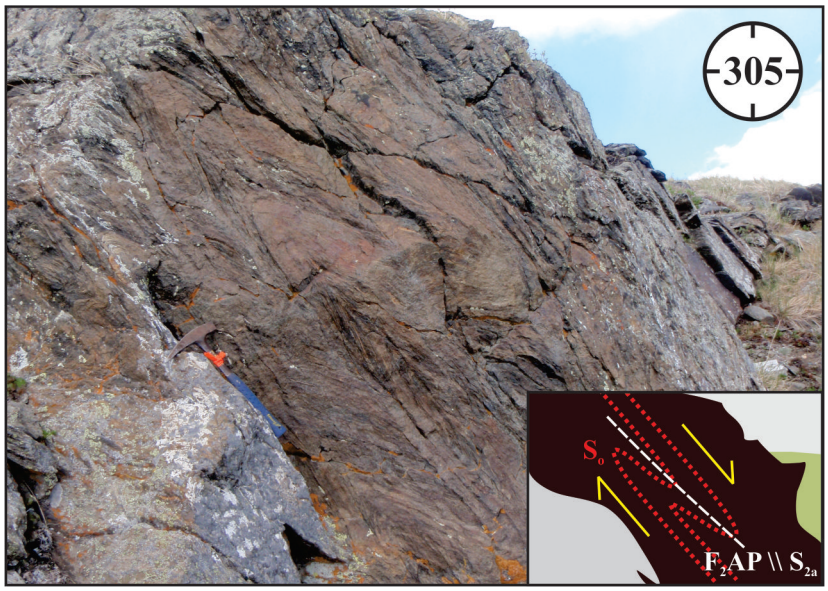

Figure 20: Station 10-VLS-011 looking 305° showing an example of a meter scale isoclinal F_2 fold defined by the trace of a quartz-rich layer interpreted as original bedding (S_o; looking 305°). This structure represents a parasitic fold related to a larger scale F_2 fold structure. Inset image exhibits a schematic drawing of the isoclinal F_2 fold structure (F_2AP = F_2 axial plane) and the corresponding shear sense (yellow arrows).

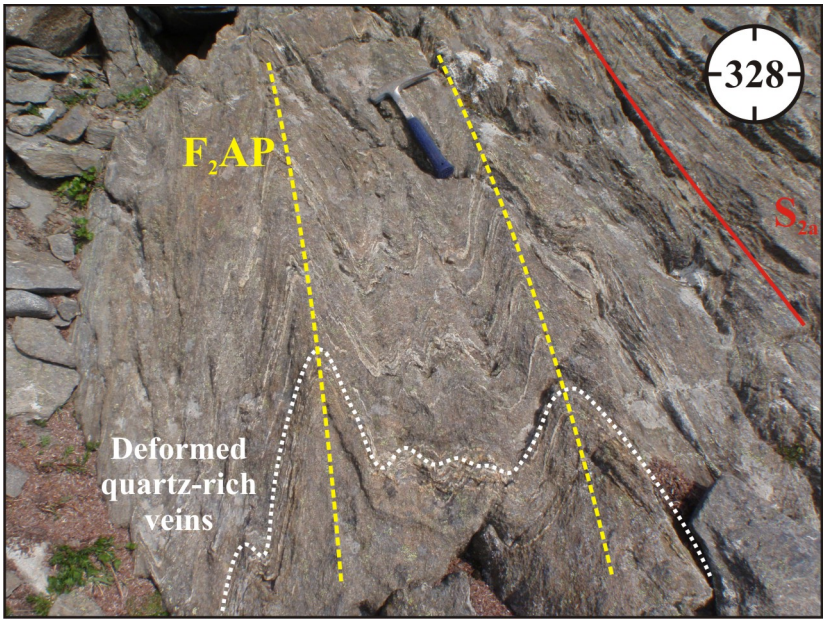

Figure 21: Station 09-VLS-088 exhibiting an M-shaped tight F_2 fold defined by the trace of deformed quartz-rich veins (white dotted line; looking 328°). This structure indicates the presence of a larger scale F_2 hinge zone. S_{2a} (red line) is parallel to F_2AP (F_2 axial plane; yellow dashed line).

stepping mantles (dominantly composed of quartz ± plagioclase ± mica; Figure 15A and 22) and, garnet porphyroblasts regularly preserve spiral-shaped S_1 inclusion trails (Figure 16A). These porphyroblasts likely formed early during D_2 deformation and were subsequently ro-

tated as passive porphyroclasts. This relationship is observed in Figure 15 where a plagioclase porphyroblast appears to have grown after the development of S_1 and, it was progressively rotated by an east-over-west sense of motion. Therefore, the transition between D_1 and D_2 events appears to have been a gradual process.

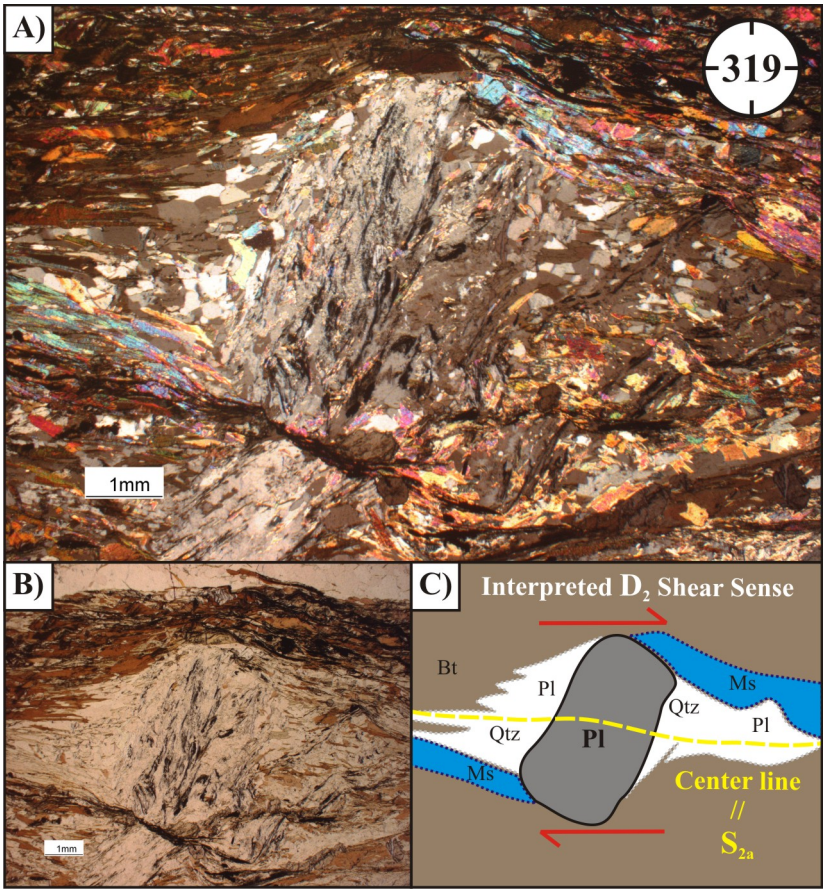

Figure 22: Station 10-VLS-157 showing an asymmetric σ-type mantled plagioclase porphyroclast resulting from northeast-over-southwest D_2 shearing. A) Cross-polarized transmitted light photograph looking 319°, B) corresponding plane polarized transmitted light photograph, and C) schematic drawing of mineralogical relationships (Bt = biotite; Ms = muscovite; Pl = plagioclase; Qtz = quartz).

Common linear fabric forming elements oriented on S_{2a} include mineral aggregate lineations (L_{2-M}) comprised of oriented micas and hornblende and mineral stretching lineations (L_{2-S}) comprised of quartz (± plagioclase and carbonate; Figure 23). Less commonly observed linear structures oriented parallel to S_{2a} include quartz-vein boudin necks (L_{2-B}; Figure 24C and D). These structures retain an oblate 'chocolate-bar' boudin morphology indicating extension in two directions. The similar mineralogical composition of L_{2-M}, L_{2-S}, and S_{2a} and, the parallel nature of these structures indicates they are genetically related. The presence of L_{2-M}, L_{2-S}, and L_{2-B} on S_{2a} coupled with the presence of D_2-related micro- and macroscopic shear sense and vergence indicators described above indicates a significant portion of the bulk

strain associated with the schist is inherently linked to the composite D_2 event.

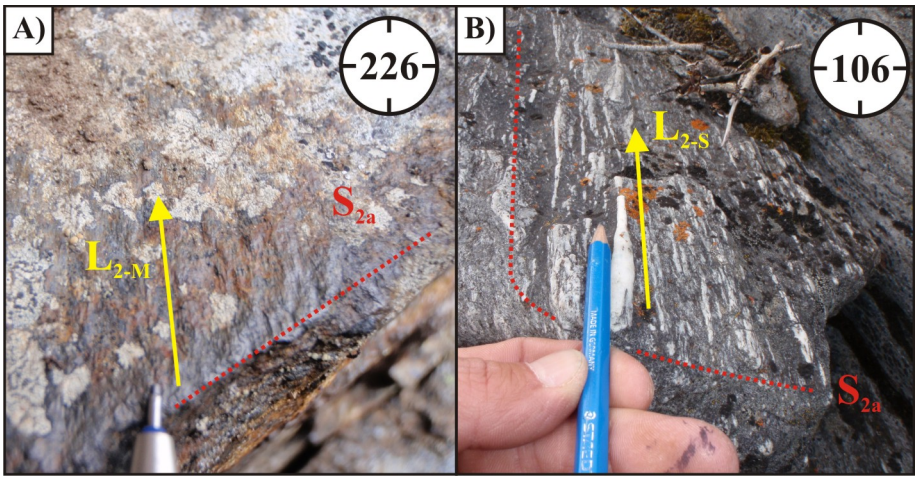

Figure 23: Textural examples of common linear fabrics associated with D_2. Yellow arrows indicate orientation of lineations and red dashed line indicates trace of S_{2a}. A) Station 10-VLS-158 showing L_{2-M} comprised of oriented fine grained biotite and hornblende grains that also define S_{2a} (looking 226°). B) Station 09-VLS-112 showing L_{2-S} consisting of well-developed 'cigar'-shaped quartz grains (looking 106°).

The rotated porphyroblasts, asymmetric strain shadows, and orientation of S_{2b} in relation to S_{2a} all represent microscopic shear sense indicators. The former two structures commonly exhibit an opposing sense of vergence similar to the asymmetric F_2 fold structures indicating they likely formed during the same, relatively early D_2 event. Although the latter structure is not as well-developed as the other D_2 structures, it does consistently exhibit a northeast-over-southwest sense of shear that this study interprets as the progressive development of a shear band cleavage during the later stages of the composite D_2 event. The progressive evolution of D_2 is interpreted to be, at least in part, responsible for dismembering and attenuating the relatively earlier formed D_2 structure.

3.3.3 Pre- to syn-D_2 quartz($\pm$ carbonate)-rich vein formation

Some time after the formation of the well-developed S_1 bedding parallel foliation, the schist became host to significant vein development. Mineralogically, the veins are composed of fine to medium grained, anhedral to subhedral, dynamically recrystallized 'milky' white quartz and carbonate grains. These veins are commonly preserved as highly attenuated centimeter scale pinch-and-swell structures oriented parallel to S_1 and S_{2a} (Figure 24). Rarely, these structures are so attenuated that the schist displays a compositional layering. Other common structures of these veins include: centimeter scale intrafolial isoclinal folds, micro- to macroscopic symmetric M-shaped and asymmetric S- and Z-shaped isoclinal folds, meter scale quartz veins that are

slightly boudinaged parallel to S_{2a}, and oblate 'chocolate-bar' boudinaged veins also oriented parallel to S_{2a} (Figure 24D). The formation of these veins prior to or during D_2 is inferred since the veins commonly trace the shape of D_2-related structures.

The orientation of veins provide valuable information in regards to the orientation and kinematics of the stress regimes during vein emplacement (Passchier and Trouw, 2005); however, in regions of high strain where veins are extremely deformed, a kinematic analysis of the stress regime during vein genesis is near impossible. Most relevant to the structural analysis of the current study is the (a)symmetry of the veins that define the trace of regional scale, overturned, parasitic isoclinal F_2 fold structures. These parasitic fold structures and the boudinaged morphology of a large portion of the pre- to syn-D_2 vein population provide shear sense indicators for the composite D_2 event. Extreme caution should be exercised when interpreting these features as the original orientation of these structures during emplacement is not known.

3.3.4 Relationship of ultramafic and YTT rocks to D_2

Within and adjacent the Kluane schist, foliated exposures of Triassic (M. Escayola, pers. comm., 2011) ultramafic and Paleozoic YTT rocks are interleaved with and conformable to S_{2a}. The numerous ultramafic bodies are commonly tens of meters in dimensions except for two kilometer scale elongate bodies at the northern end of Kluane Lake and east of Haines Junction (Figure 2). Mezger (1997 and 2000) notes the distinct textural similarity and parallel orientation of tectonic fabrics observed in the ultramafic and Kluane schist rocks (*i.e.,* S_{2a}) indicating the two were likely interleaved some time prior to or during the formation of S_{2a}. At the northeastern exposure of the biotite-rich Kluane schist approximately 3 km west of Killermun Lake, a 100 m thick and 300 m long outcrop of YTT rocks is present (Figure 4 and cross-section B-B$'$ in Figure 25). This YTT exposure is composed of interlayered foliated mafic volcanic rocks, calcareous psammitic and semi-pelitic schists, and white marble (Figure 3). Decimeter scale isoclinal folds defined by the trace of white marble layers are present in this deformed sedimentary succession. Axial planes of these folds are parallel to the orientation of a well-developed foliation in the psammitic and semi-pelitic schist layers. This foliation is defined by the alignment of biotite and the microlithons are defined by the alignment of recrystallized quartz. This YTT body is mantled by foliated (S_{2a}) biotite-rich schist. The foliations in YTT and the schist are similar in texture and parallel to each other and the structurally higher YTT/biotite-rich schist contact (Figure 4). The structurally lower lithological contact is not observed in outcrop; it is believed to be parallel to the upper lithological contact.

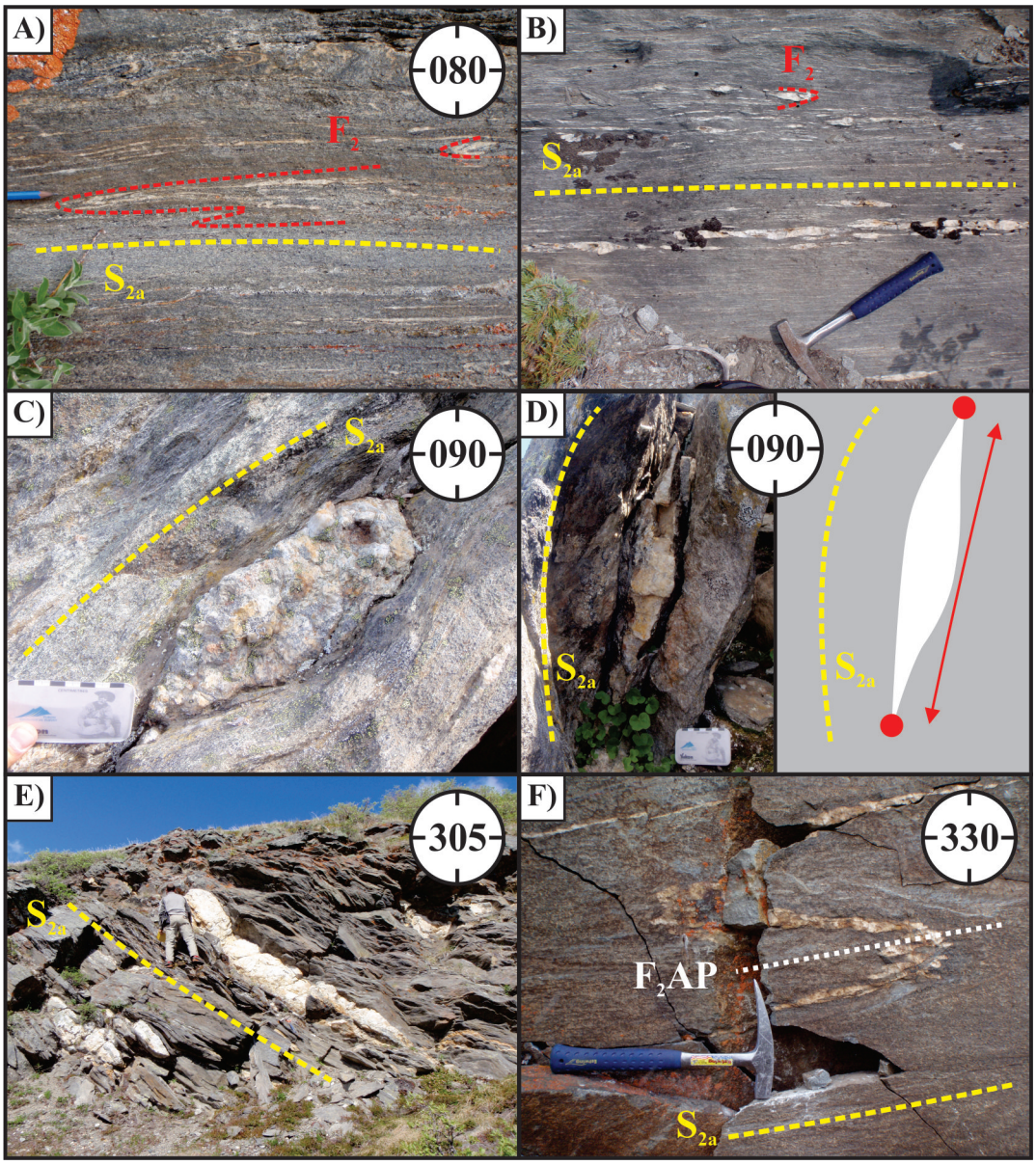

Figure 24: Examples of pre- to syn-D_2 deformed quartz-rich ($\pm$ carbonate) veins. Yellow dashed line indicates trace of S_{2a}. Orientation of view is labelled in top right corner of photographs. A dominant portion of these deformed veins appear as micro- to macroscopic isoclinal F_2 folds with axial planes oriented parallel to S_{2a}. A) Station 09-VLS-075 and B) station 09-VLS-110 exhibit centimeter thick veins that have been folded into isoclinal F_2 folds (see red dashed lines) and extended wherein the fold limbs are completely dismembered and appear as lensoidal shapes. Station 10-VLS-247 (C and D) display decimeter thick veins that retain a 'chocolate-bar' boudinage morphology indicating extreme D_2-related extension (L_{2-B} and red dots indicate orientation of boudin neck plunging into page and red arrows indicate orientation of boudin neck oriented parallel to page). E) Station 10-VLS-011 reveals a thick meter scale vein boudinaged parallel to S_{2a}. F) Station 09-VLS-029 displays a deformed vein with parasitic isoclinal F_2 fold patterns on a relatively larger S-shaped tight to isoclinal F_2 fold structure ($F_2AP = F_2$ axial plane).

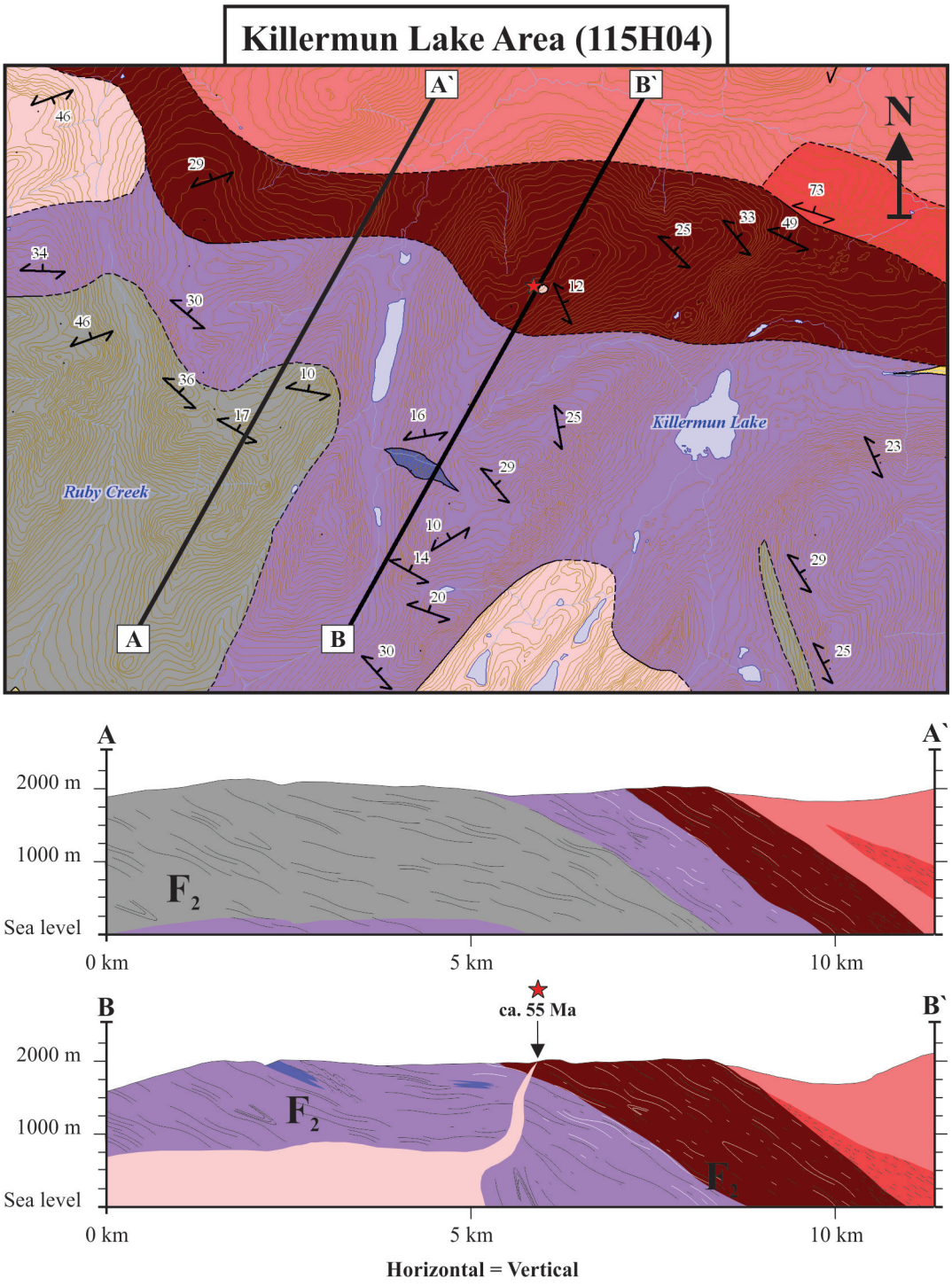

Figure 25: Geological map and cross-section A-A′ and B-B′ of the Killermun Lake area. Blue wedge at center of map indicates location of YTT rocks. Age date of undeformed dyke in cross-section B-B′ corresponds to a U-Pb zircon age date quoted in Chapter 4. Wavy black lines indicate trace of folded (F_4-related) S_{2a} and wavy white lines indicate trace of folded quartzofeldspathic igneous material (*i.e.*, leucosomes that define the cordierite-bearing Kluane gneiss). Foliated RRB is distinguished from massive RRB by small black dashes (see far right dark pink unit in both cross-sections). F_2 indicates fold structure observed at surface and interpreted in the subsurface. See Figure 2 for corresponding colour legend.

3.3.5 Regional scale S_{2a} map pattern

During the fieldwork it became apparent that the northwestern half of the Kluane schist contains moderately northeast dipping S_{2a} orientations and, towards the southeastern extent, S_{2a} orientations range from moderately northeast to steeply southwest dipping. This change in orientation is observed along McKinley Creek (Figure 26). Along this creek, S_{2a} orientations on the northern ridge tops are consistently north-northeast to northeast dipping while the southern ridge tops exhibit moderately east-southeast dipping orientations that gradually change into south-southeast dipping orientations towards the southeast. S_{2a} orientations discordant with these orientations are present and are possibly caused by either: 1) relatively younger intrusive phases and/or 2) re-organization of the bedrock due to faulting associated with the Denali fault system and its subordinate faults.

Along McKinley Creek, a geophysically determined fault is present (Figure 26). This fault could explain the change in orientation of S_{2a} however, towards the northwest where this fault appears to be terminated (east of Big Joe Lake), S_{2a} orientations north and south of the fault are parallel. Furthermore, the ridge top south of McKinley Creek exhibits a gradual change from east-southeast to south-southeast dipping S_{2a} orientations indicating that faulting north of these ridge tops is not the sole cause for the change in S_{2a} orientations. Nevertheless, the fault could help explain a small portion of the S_{2a} orientation change. Notably, at the southeastern end of McKinley Creek, the cordierite-bearing gneiss appears to be offset by approximately 7.5 km of right-lateral horizontal displacement (Figure 26); however, the muscovite-rich and biotite-rich schist units do not appear offset. This intricate map pattern is discussed in the following section as the structural characteristics of the three units in that area appear to define a relatively large scale F_3 fold pattern.

Using equal-area lower hemisphere pole-plots, S_{2a} orientations appear to display regional scale preferred orientations (Figure 27). As described above, the map pattern of S_{2a} manifests itself into two geographically distinct domains: northwest and southeast. Whereas the map pattern cryptically displays this change in orientation, statistical analysis using equal-area pole-plots clearly shows this change in orientation is hosted within the southeast domain (Figure 27C and D). Figure 27A and B shows the northwestern domain contains a point maximum of S_{2a} poles concentrated around a single mean orientation of 295/29 (RHR = Right Hand Rule). Conversely, Figure 27C and D shows the southeastern domain contains a distribution of S_{2a} poles along a great-circle girdle (π-circle) oriented at 208/81 (RHR). This great-circle girdle corresponds with a calculated beta-axis (fold-axis) of 09−118 (PLNGE-TRND = Plunge-Trend). Collectively, these calculated structural attributes define a regional scale, relatively

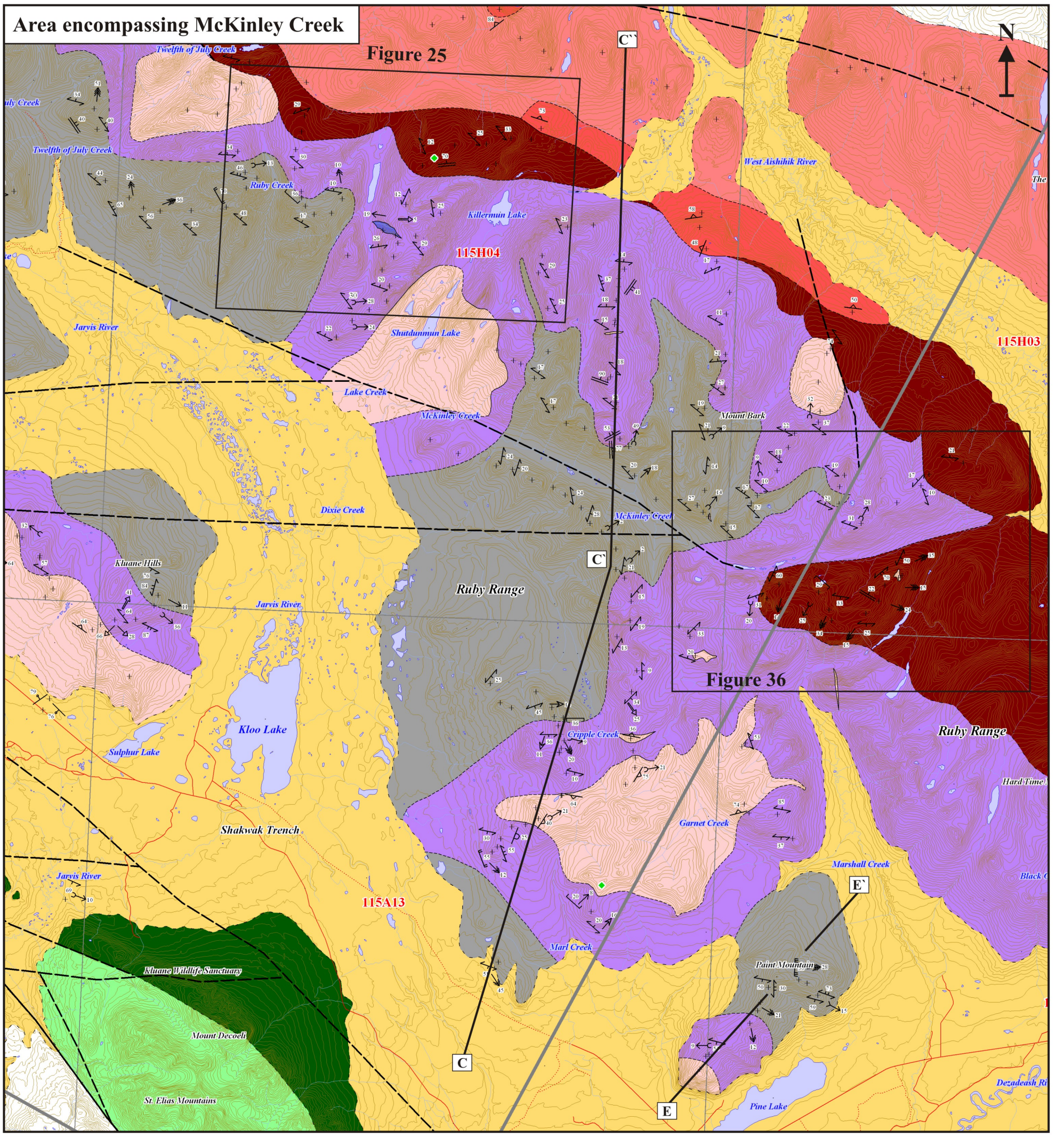

Figure 26: Geological map of area encompassing McKinley Creek. Green diamonds indicate location of *U-Pb* zircon LA-ICPMS samples discussed in detail in Chapter 4. Outline of Figure 25 and 36 are indicated as well as the location of cross-section C-C`-C`` (Figure 28) and E-E` (Figure 34). Figure 2 contains corresponding colour legend

open upright shallowly east-southeast plunging fold in the southeastern domain. Figure 28A displays this fold in the northeast-southwest trending vertical cross-section C-C′-C″. Coincidently, the location of the fault along McKinley Creek appears to be parallel to the axial plane of this broad fold. This fold structure post-dates D_2 and D_3 events (discussed in following section).

3.3.6 Regional scale F_2 fold structure

As mentioned briefly above, F_2 fold structures are ubiquitously preserved as M-, Z-, and S-shaped tight to isoclinal folds that define either northwest-over-southeast or southeast-over-northwest tectonic vergence. The opposing sense of shear associated with rotated porphyroblasts, the corresponding asymmetric strain shadows, and the F_2 folds combine to trace larger, regional scale parasitic F_2 fold structures. In the northwestern domain, one such structure is observed in Figure 29 along the vertical cross-section D-D′. At the furthest western extent of this section, the lower limb of an overturned F_2 synform is defined by the presence of an S-shaped isoclinal F_2 fold (looking north). The axial plane of this fold dips moderately towards the northeast and plunges shallowly towards the east-southeast, respectively. Further northeast along this section, Z-, S-, M-, and S-shaped fold patterns are observed in sequence. Collectively, these isoclinal F_2 folds trace the shape of overturned antiform/synform structures.

In the southeastern domain where anomalous southwest-dipping S_{2a} orientations are present, the regional scale F_2 fold structure is quite different in shape to the fold structure observed in the northwestern domain. Here, the regional F_2 fold structure is observed along the vertical cross-section C-C′-C″ (Figure 26 and 28). Along this section, S-shaped isoclinal F_2 folds (looking north) are present with axial planes dipping towards the northeast and southwest. Coupled with the trace of S_{2a}, the two S-shaped isoclinal F_2 folds define the trace of a broad, open post-F_2 fold structure. S_{2a} and F_2 axial plane orientations discordant with this large scale fold are interpreted as deflections caused by the relatively large Hayden Lake intrusive suite that outcrops throughout the central portion of schist. Assuming there is an F_2 fold closure to the west, the regional scale broad, open fold is interpreted as a folded upper limb of an overturned F_2 antiform structure.

In the northwestern domain, where a significant portion of the structural data-set is concentrated, equal-area plots generally show a point maximum of F_2 fold axis, L_{2-M}, and L_{2-S} measurements shallowly plunging towards the east and east-southeast (Figure 30). In the southeastern domain, where static recrystallization of the Kluane schist is more prevalent, linear fabric elements are less obvious and therefore, the quantity of measurements is considerably less compared to the northwestern domain. However, equal-area plots clearly show a

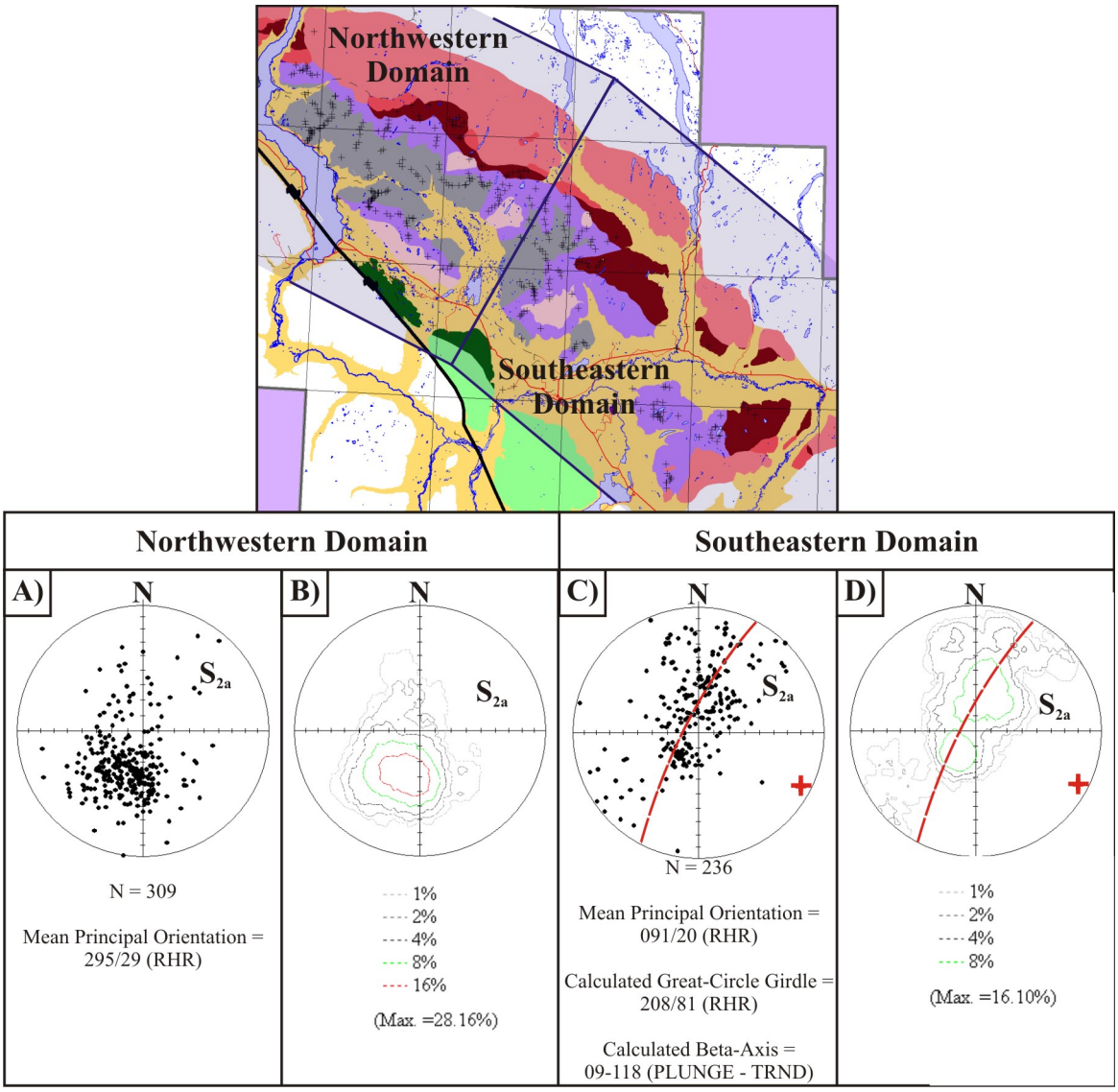

Figure 27: Northwestern (A and B) and southeastern (C and D) domain analysis of S_{2a}. Black crosses on map indicates location of S_{2a} measurements. A) equal-area lower hemisphere pole-plot and B) contoured pole-plot of S_{2a} measurements from northwestern domain. C) equal-area lower hemisphere pole-plot and D) contoured pole-plot of S_{2a} measurements from southeastern domain. Note the distinct asymmetry of the pole-plot in A and the relatively more symmetric pole-plot in C indicating the dominance of northeastern dipping foliations in the northwestern domain and the presence of a broad, open, shallowly plunging post-D_2 fold in the southeastern domain. Red dashed line and red crosses indicate locations of calculated great-circle girdle and beta-axis (*i.e.,* post-D_2 fold axis). Preferred orientation patterns of the corresponding structural element was analyzed with the use of GEOrient©, a shareware application developed to analyze orientation patterns.

point maximum of L_{2-M} measurements shallowly plunge towards the east in the southeastern domain (Figure 30E). A considerable amount of data was collected and the statistically preferred orientation patterns of D_2-related linear fabric elements display a trend towards the east to east-southeast.

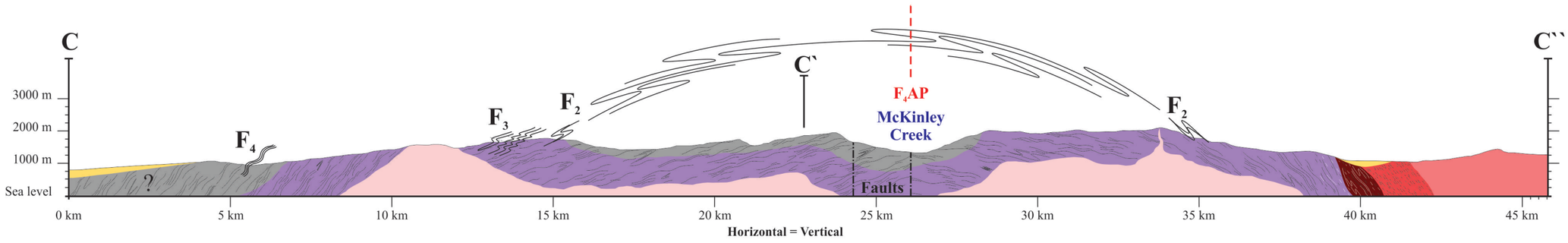

Figure 28: Cross-section C-C`-C`` exhibits the change in S_{2a} orientations in the vicinity of McKinley Creek. Thick black lines represent observations at surface and thin lines represent interpretations based on surficial observations. White lines represent quartzofeldspathic layers. See Figure 26 for location and Figure 2 for corresponding colour legend.

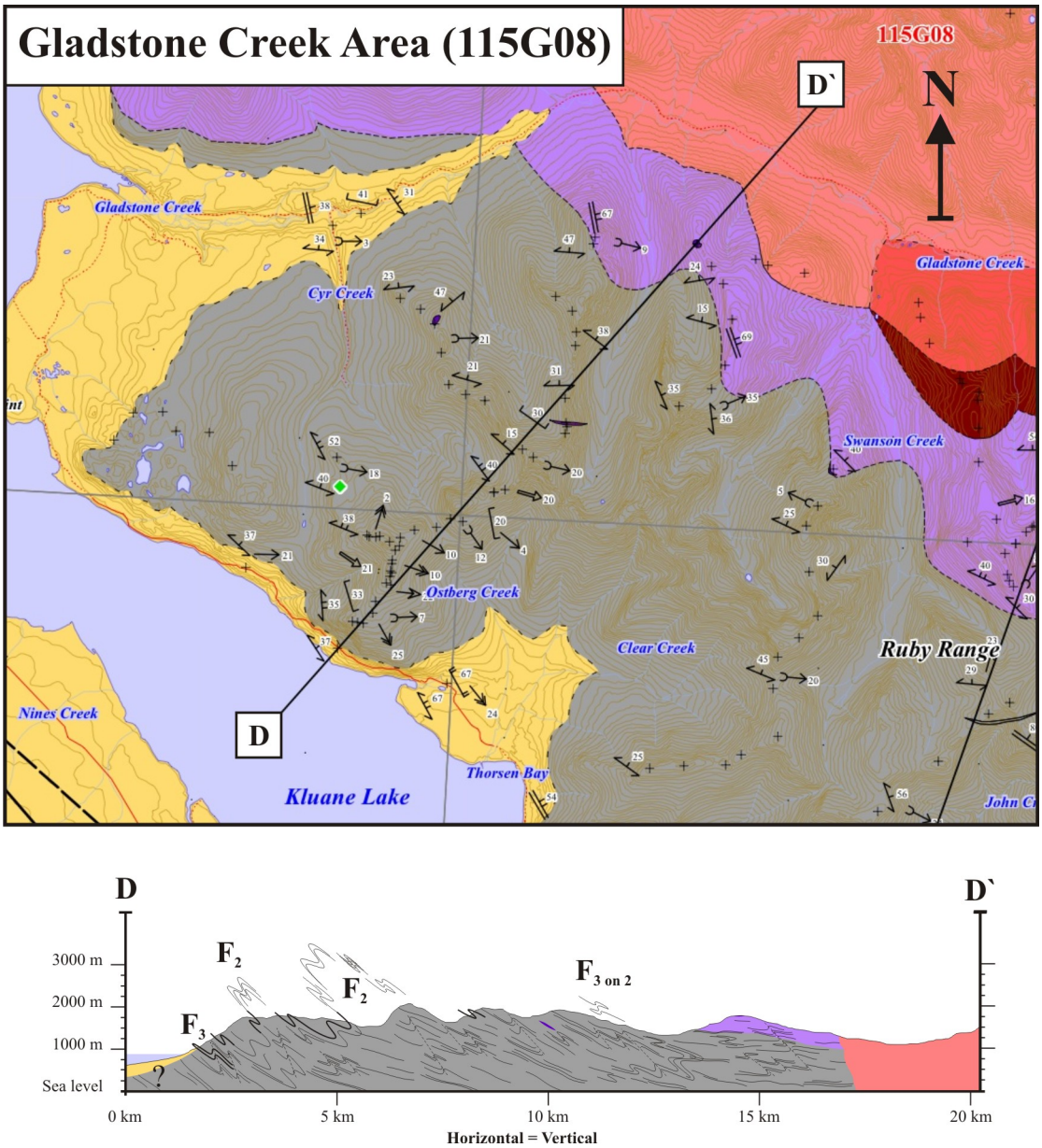

Figure 29: Geological map and cross-section D-D′ of the Gladstone Creek area. F_2 and F_3 indicate location of corresponding fold structure observed at surface. Wavy black lines indicate trace of folded (F_4-related) S_{2a}. See Figure 2 for corresponding colour legend and Figure 26 for symbol legend. Green diamond on map indicates location of U-Pb detrital zircon sample discussed in Chapter 4.

Given the large of amount of strain associated with D_2 and the monotonous lithological character of the Kluane schist, regional scale folding is difficult to deduce. However, small scale parasitic F_2 fold structures record vergence variations that, in turn, trace the schist's architecture as a sequence of overturned, dismembered, isoclinal, synform/antiform structures that have subsequently been folded into a broad, open, upright fold. High syn- to post-D_2 strain negates the ability to trace specific F_2 fold closures across valleys or along ridge-tops

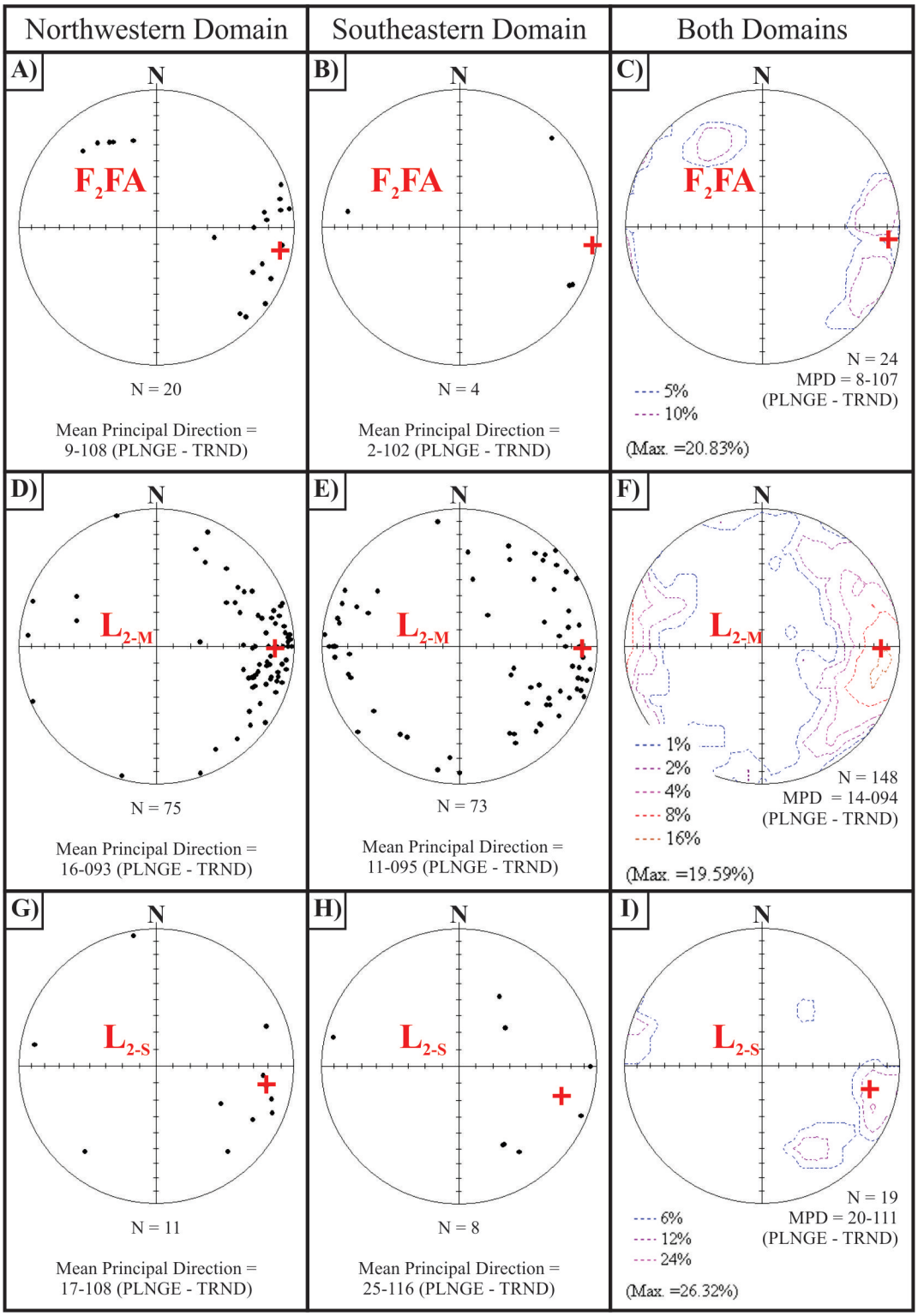

Figure 30: Equal-area lower hemisphere plots of F_2 fold axis (A-C), L_{2-M} (D-F), and L_{2-M} (G-I) from northwestern (left column) and southeastern (middle column) domains. Right column displays data from both domains as contoured plots. Red crosses indicate location of mean principle direction (MPD) of corresponding linear structure. Note the distinct preferred orientation of all three linear structures plunge shallowly towards the east to east-southeast.

that lack sufficient exposure. Moreover, the fact that F_2 fold axes are, in places, parallel to well-developed L_{2-M} and/or L_{2-S} (Figure 30) indicates the larger, regional scale F_2 fold structures are likely quite attenuated (discussed later).

3.3.7 Metamorphic signature of D_2

The earliest signals of M_2 [M_1 of Mezger *et al.* (2001)] are recorded by the growth of syn-kinematic plagioclase and garnet porphyroblasts. These porphyroblasts, coupled with the growth of other metamorphic minerals discussed above, define mineral assemblages in the schist that range from greenschist to upper amphibolite/granulite facies. Mezger (1997) completed detailed mapping of numerous metamorphic zones that are marked by the first appearance of a specific index mineral (*e.g.,* garnet, biotite, *etc.*). These zones, which are similar to the three Kluane schist sub-units identified over the course of this study, define an inverted northeast-dipping metamorphic gradient that increases towards the northeast where the relatively highest grade cordierite-bearing gneiss is present at the Kluane schist-Ruby Range batholith (RRB) contact. However, anomalous areas exist where the inverted metamorphic aureole dips broadly towards the west (see area west of Kloo Lake and the area surrounding Paint Mountain in Figure 26; also see western portion of cross-section C-C′-C′′ in Figure 28). These map patterns are interpreted to be the result of a succeeding thermal event associated with D_4 (discussed later). Intrusion of the RRB appears to be responsible for the destruction of the Kluane schist/YTT contact. The orientation of the metamorphic zones towards the northeast are parallel to sub-parallel to the orientation of S_{2a} in the schist and, they are also parallel to foliated exposures of the RRB (see eastern portions of Figure 25, 26, 28, and 29). These geologic relationships indicate that the increase in metamorphic grade towards the northeast occurred during deformation and, simultaneously, foliated phases of the RRB were intruding along the structurally highest, northeastern extent of the Kluane schist. Similar metamorphic aureoles are present surrounding syn- to post-kinematic intrusions of the Hayden Lake intrusive suite but the texture and map pattern of these aureoles indicate they formed during D_4 (discussed in later section).

The northeast dipping metamorphic zones are interpreted to have formed at some time during the composite D_2 event. Deformation associated with D_2 shearing/folding and thermal heating associated with intrusion of the early stages of RRB emplacement likely both played a role in developing the inverted contact metamorphic aureole. Faulting and/or F_2 folding of the metamorphic zones is not observed. F_3 folding of the zones appears to be present in the area proximal to the southeast end of McKinley Creek indicating the inverted metamorphic aureole formed at some time late during D_2, following regional scale isoclinal F_2 folding. Mezger *et al.*

(2001) states cores of the syn-kinematic plagioclase and garnet porphyroblasts record moderate pressure and temperature conditions at approximately 7 kbar and 500°C, respectively. This places the schist at a maximum depth of approximately 24 kms during M_2 (2.8 g/cm^3 crustal density; Winter, 2001). An interpretation of the structure and metamorphic architecture of the schist is discussed in the final section of this chapter.

3.4 D_3 - Northeast-over-southwest vergent folding and Ruby Range batholith emplacement

Structures associated with the third phase of deformation (D_3) are heterogeneously developed in the Kluane schist. Common D_3 structures comprise close to tight inclined asymmetric centimeter to meter scale F_3 folds defined by the trace of S_{2a} and deformed isoclinal F_2 folds. F_3 folds regularly contain an axial planar cleavage (S_3) defined by the alignment of fine to medium grained biotite and muscovite (± chlorite; M_3; Figure 31). Less commonly, F_3 folds are defined by the trace of deformed discontinuous, meter thick felsic dykes (Figure 32). The cordierite-bearing Kluane gneiss exhibits close to tight asymmetric and convolute F_3 folds that lack an axial planar cleavage (Figure 33). F_3 folds consistently exhibit a northeast-over-southwest sense of vergence (Figure 31).

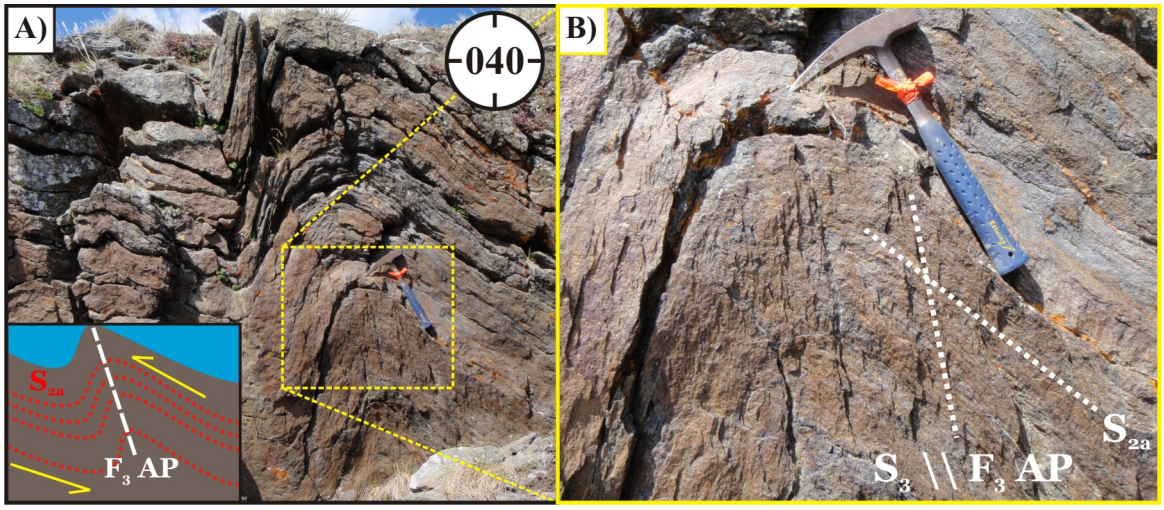

Figure 31: Station 10-VLS-011 showing a west vergent tight F_3 fold with well-developed axial planar cleavage ($S_3 = F_3AP$; looking 040°). A) Outcrop photo with schematic drawing shown in inset diagram and, B) photograph of S_3 axial planar cleavage in hinge zone of F_3 fold.

Using equal-area lower hemisphere plots, F_3 fold axis and axial plane measurements display regional scale preferred orientations (Figure 34). Within both domains, F_3 fold axis measurements contain a bimodal point maximum of orientations that plunge shallowly towards the north-northwest and southeast (Figure 34C). The later orientation represents a dominant por-

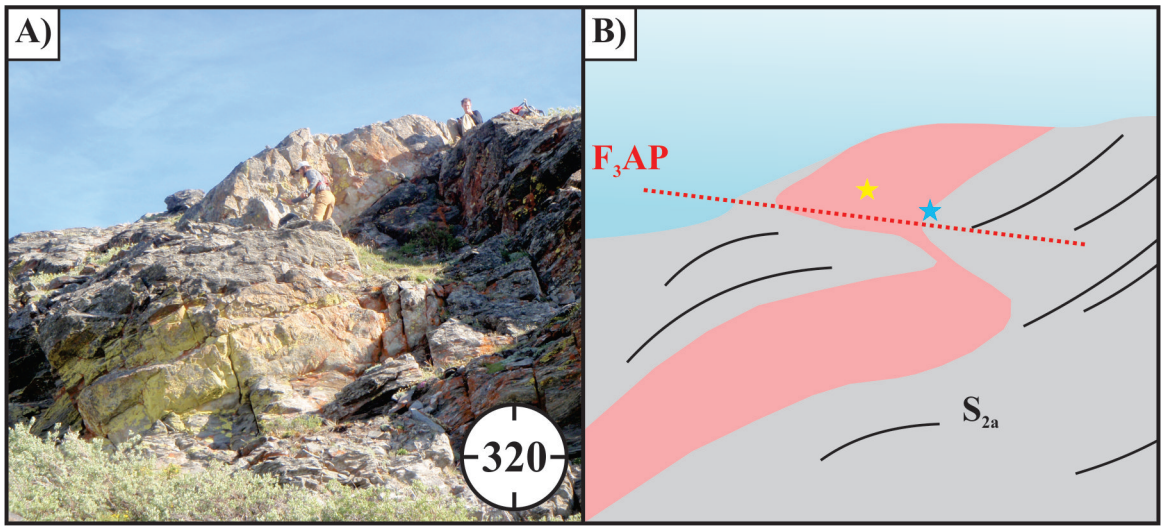

Figure 32: Meter scale thick leucocratic tonalite dyke folded into an asymmetric southwest vergent F_3 fold at station 10-VLS-136. Host rock is muscovite-rich Kluane schist. A) Outcrop photograph looking 320° and, B) schematic drawing of outcrop relationships. The apparent necking of the dyke at the hinge zone of the fold is apparent due to the depth of the photograph and weathering. F_3AP indicates trace of F_3 axial plane. Blue star indicates location of hand-sample collected for microscopic kinematic analysis and yellow star indicates location of sample collected for U-Pb zircon LA-ICPMS geochronology (discussed in detail in Chapter 4).

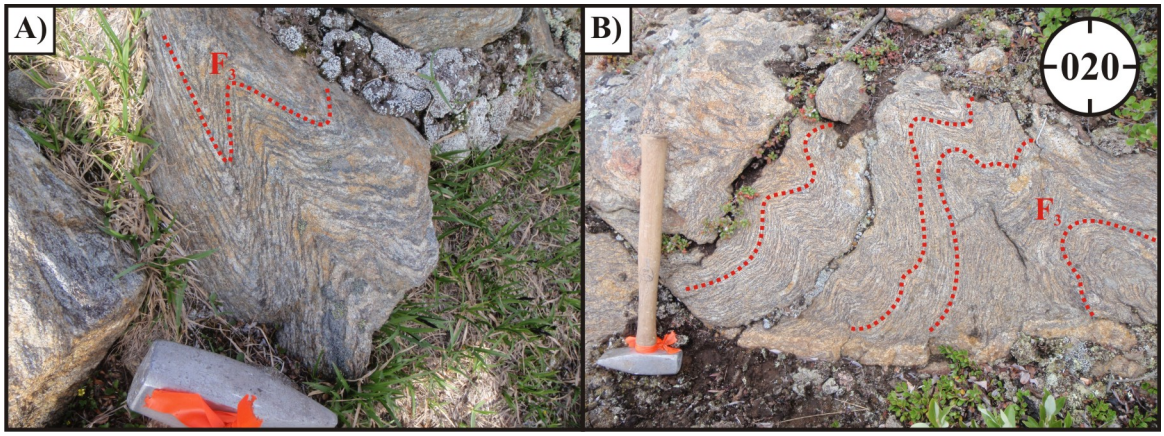

Figure 33: Examples of close to tight asymmetric F_3 folds in cordierite-bearing Kluane gneiss. A) Station 10-VLS-244 showing a tight asymmetric F_3 fold in a boulder. B) Station 10-VLS-281 exhibiting convolute F_3 folds (looking 020°).

tion of the F_3 fold axis data-set. Similar to the regional scale preferred orientation pattern of S_{2a} poles (*i.e.,* F_2 axial planes), F_3 axial plane orientations in the northwestern domain are consistently northeast dipping while in the southeastern domain, northeast and southwest dipping orientations are recognized. A compilation of the F_3 axial plane poles from both domains spread along a slightly symmetric calculated great-circle girdle and beta-axis oriented at 217/73 (RHR) and $17 - 127$ (PLNGE-TRND), respectively (Figure 34F). Notably, these features are within approximately 10° of the calculated great-circle girdle and beta-axis for S_{2a}

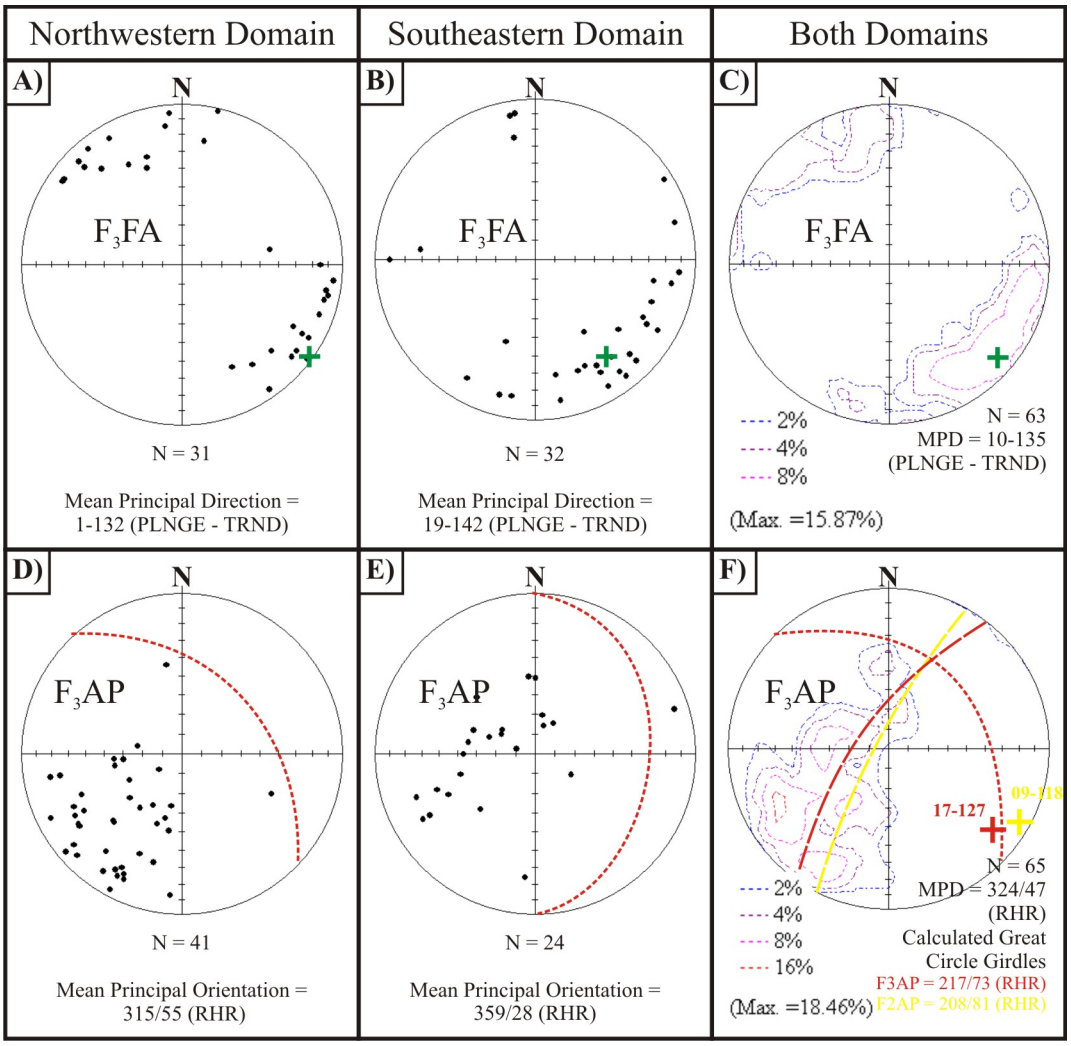

Figure 34: Equal-area lower hemisphere plots and contoured plots of F_3 fold axis (A-C) and F_3 axial plane measurements (D-F) from northwestern (left column) and southeastern (middle column) domains. Right column displays contoured plots of both domains. Green crosses indicate location of mean principle direction (MPD) of fold axis measurements and short red dashed lines indicate location of MPD of axial plane measurements. Long red and yellow dashed lines indicate locations of calculated great-circle girdles for F_3 and S_{2a} (*i.e.*, F_2 axial plane) pole measurements, respectively. Red and yellow crosses indicate locations of corresponding calculated beta-axes for F_3 and S_{2a} great-circle girdles.

poles. These two sets of calculated features are interpreted to be parallel, which indicates the same broad, open fold responsible for folding S_{2a} is also responsible for folding F_3 axial planes. This feature is recognized in the field where the consistently southwest vergent F_3 folds appear on both northeast and southwest dipping S_{2a} orientations (Figure 29 and 35).

The presence of southwest vergent F_3 folds within the cordierite-bearing gneiss indicates the gneiss (and the corresponding inverted metamorphic aureole) formed prior to D_3. Southwest vergent F_3 folds are also observed in deformed granitic dykes indicating that the early stages of Ruby Range batholith (RRB) were being emplaced prior to D_3. The author inter-

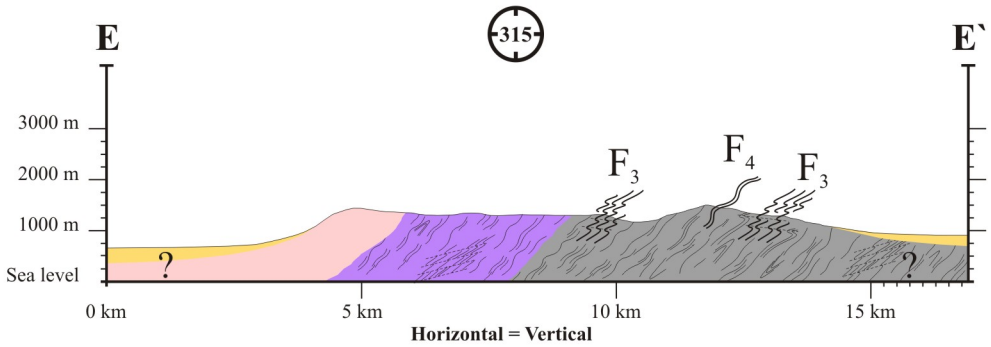

Figure 35: Geological cross-section E-E′ of the Paint Mountain area (looking 315°). F_3 and F_4 indicate location of corresponding fold structure observed at surface. Wavy black lines indicate trace of folded (F_4-related) S_{2a}. See Figure 26 for location and Figure 2 for corresponding colour legend.

prets that the inverted metamorphic aureole in the Kluane schist formed late during D_2 and following F_2 given the lack of F_2 folding evidence of the metamorphic aureole. The aureole appears to have formed almost contemporaneously as the early stages of RRB intruded into the schist.

The map pattern of the cordierite-bearing gneiss occurs as a linear feature parallel to and between the biotite-rich schist and foliated and massive phases of the RRB (Figure 2). However, at the southeastern end of McKinley Creek the cordierite-bearing gneiss appears to be offset by approximately 7.5 km of right-lateral horizontal displacement (Figure 26). The muscovite- and biotite-rich schist units do not appear to be offset. The intricate map pattern of all three units in this region coupled with the change in orientation of S_{2a} through this area could possibly be explained by the presence of a relatively large scale shallowly southeast plunging F_3 fold. This fold is displayed in Figure 36 which shows a schematic block diagram sketch of the area at the southeastern end of McKinley Creek. Detailed mapping in this region is lacking. Nevertheless, the limited data appears to show a fold closure of all three units of the Kluane schist. In Figure 36, plane ABCD shows an oblique view of the broad, open F_4 fold defined by the folding of S_{2a} and F_3 axial plane poles discussed in the previous section. Plane CDEF shows how the intricate map pattern at surface is transformed into an F_3 fold closure in the subsurface. These map patterns appear to confirm that the inverted metamorphic aureole developed prior to D_3.

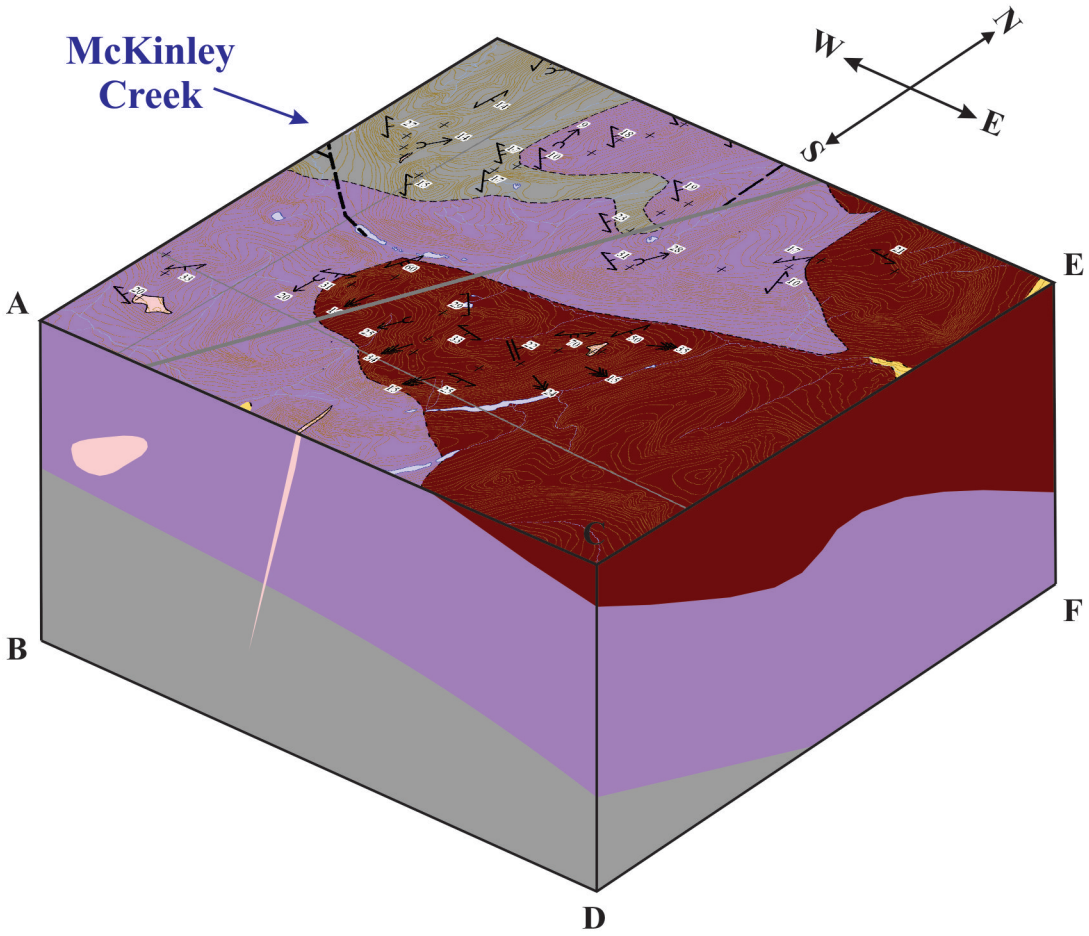

Figure 36: Schematic block diagram sketch of the area southeast of McKinley Creek. Note that plane ABCD displays the eastern shallowly dipping limb of a broad, open F_4 antiform fold structure and plane CDEF displays a southwest vergent F_3 fold defined by the map pattern of the D_2-related inverted metamorphic aureole. See Figure 26 for location and scale.

3.5 D_4 - Broad, open regional scale folding, emplacement of syn-kinematic intrusions, and the development of a 'late' metamorphic overprint

Structures associated with the fourth phase of deformation (D_4) are ubiquitous in the Kluane schist. D_4 structures comprise broad, open, undulating symmetric decimeter to meter scale F_4 folds [F_{n+3} of Mezger (1997)] defined by the trace of S_{2a} (Figure 37). Where the S_{2a} plane is exposed, these folds appear as decimeter scale dome-and-basin patterns wherein fold axes are generally shallowly plunging (Figure 37B) and axial planes are steeply dipping to vertical. No preferred orientation pattern of F_4 fold axis and/or axial plane trends is identified in the study area.

Less common D_4-related structures include 'fresh' ridge-in-groove lineations (L_{RG}; Figure 38) and deformed quartz-rich tension gashses (Figure 39). The former structure is repre-

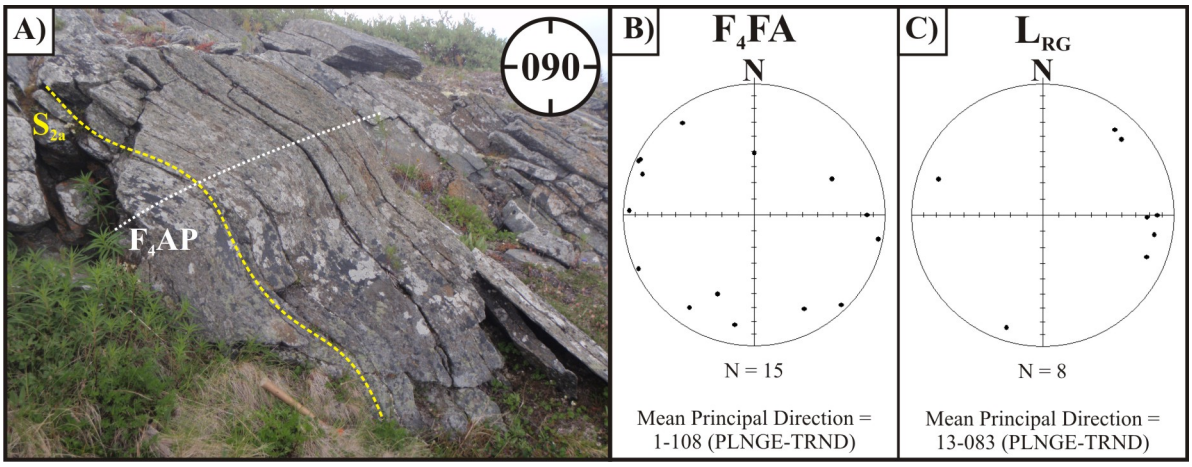

Figure 37: Station 10-VLS-257 showing: A) a broad, open, undulating F_4 fold pattern (F_4AP = F_4 axial plane; looking 090°). B) Equal-area lower hemisphere plot of F_4 fold axis and C) L_{RG} (ridge-in-groove) measurements from both domains. See Figure 38 for outcrop evidence of L_{RG}.

sented by groups of parallel striae oriented parallel to a silky slickenside surface (S_{2a}). L_{RG} structures are defined by the alignment of ridges and grooves composed of mica and quartz grains. The limited number of L_{RG} measurements (*i.e.,* 8) show an array of orientations with consistently shallow plunge values (Figure 37C). Quartz-rich tension gashes are present in minor amounts and also show an extremely variable orientation pattern (not shown here). The deformed shape of a small population of these centimeter scale veins exhibit an opposing sense of shear (*i.e.,* both top-to-the-east and top-to-the-west) and, they appear to only preserve one episode of shortening (Figure 39).

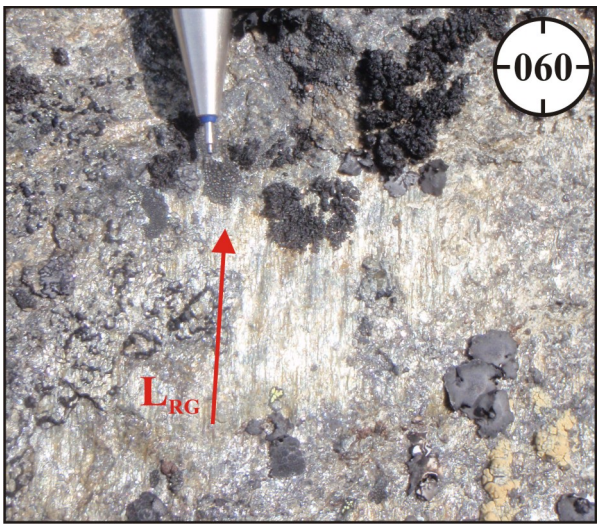

Figure 38: Station 10-VLS-265 showing a textural example of L_{RG} (red arrow) oriented on S_{2a} (looking 060°). S_{2a} surface is composed of mica and quartz grains.

Field observations and statistical analysis of S_{2a} and F_3 axial plane measurements indicate

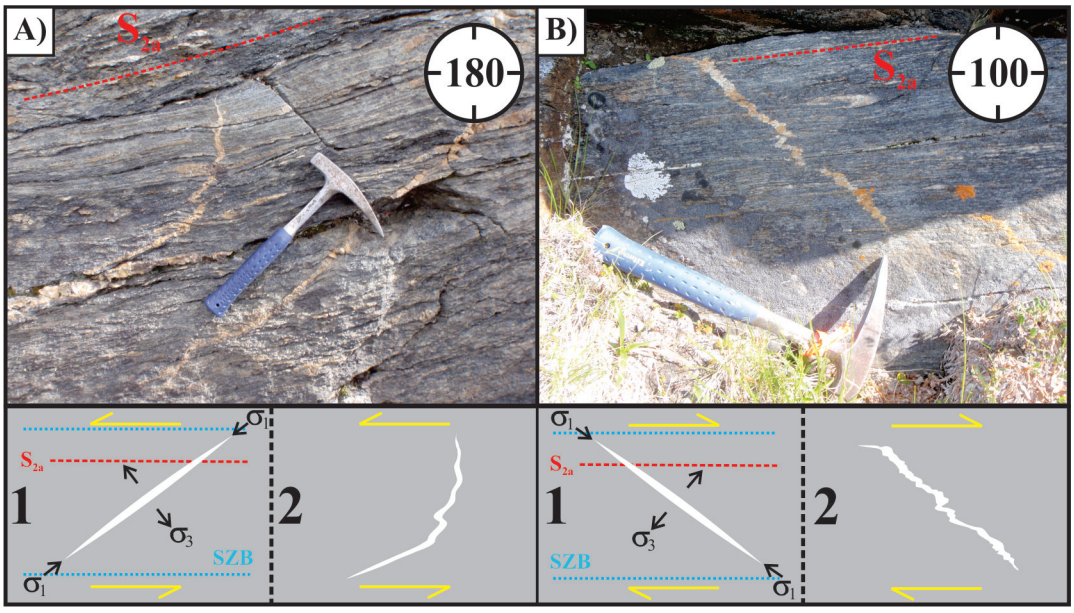

Figure 39: Examples of deformed D_4-related quartz-rich tension gash veins. A) Station 09-VLS-033 and B) station 10-VLS-121 exhibit centimeter thick veins that have been deformed by top-to-the-east and top-to-the-west movement defined by their folded (*i.e.,* shortened) morphology, respectively. Red dashed line indicates trace of S_{2a}. Orientation of view is labelled in top right corner of photographs. Inset images display: 1) hypothetical vein emplacement orientation with respect to orientation of principle compressive (σ_1) and tensile (σ_3) stresses and shear zone boundaries (SZB) and, 2) schematic diagram of the sense of motion responsible for deformation.

a broad, open, regional scale F_4 fold plunges shallowly towards the east-southeast in the Kluane schist (Figure 27 and 28). Massive and foliated igneous phases associated with the Hayden Lake intrusive suite (HLIS) appear to intrude this structure. Consequently, these igneous phases appear both discordant and concordant with the F_4 structure wherein concordant foliated phases intrude the western limb (Figure 35) while discordant phases appear to intrude the hinge region of the structure (Figure 28 and 40). Localized metamorphic aureoles are associated with these intrusive phases and they are defined by the growth of relatively coarse grained pristine phase 2 garnet grains (± biotite; see Chapter 2; Figure 7). To review, phase two garnet grains are relatively pristine with sharp grain boundaries that truncate S_{2a}. This study interprets phase two garnet grains grew during D_4 wherein the igneous phases associated with the HLIS impart local contact metamorphic aureoles onto the schist (see area west of Kloo Lake and the area surrounding Paint Mountain in Figure 26; also see western portion of cross-section C-C′-C″ in Figure 28). During intrusion, the schist was folded into a regional scale F_4 structure that is preserved in the southeastern portion of the Kluane schist. Whereas M_2 metamorphism is associated with moderate temperature and pressure conditions (*i.e.,* 7 kbar and 500°C), M_4 metamorphism (M_2 of Mezger *et al.,* 2001) is associated with distinctly higher temperature and lower pressure conditions indicating the schist was exhumed as well as heated during D_4

(3.5 to 4.5 kbar and 530 to 720°C; Mezger *et al.,* 2001).

Figure 40: Compositional layering texture observed at outcrop where sample 10-VLS-161 was collected (looking 305°). The mafic layers are composed of aligned hornblende and biotite grains and the felsic layers are comprised of dynamically recrystallized quartz and plagioclase grains. A sample was collected from this outcrop for U-Pb zircon LA-ICPMS (see Chapter 4).

3.6 Discussion of structural and metamorphic evolution of the Kluane schist

Following deposition of the Late Cretaceous Kluane schist protolith, it likely underwent diagenetic compaction due to burial of successive layers. This compaction led to volume loss associated with the expulsion of pore fluids and volatiles associated with certain hydrous clay minerals (Winter, 2001). Subsequently, a bedding-parallel foliation (S_1) formed during D_1. This foliation likely developed under sub-greenschist grade metamorphic conditions [M_1; M_1 of Mezger (1997)]. Winter (2001, p. 562) indicates that relatively low-grade metamorphism of pelitic-like sediments is an arbitrarily defined zone "in the range of approximately 200 °C and 0.15 GPa." Based on an average pressure gradient in the crust of 0.0286 GPa/km (using 2.8 g/cm^3 as an average density of the crust) this places the Kluane schist at 5.25 km depth during M_1 (Winter, 2001). Although these values do not represent robust qualitative estimates of the temperature and pressure conditions associated with M_1, they do represent a starting point at which D_1 may have occurred.

Folding of S_1 is recorded by microscopic open to isoclinal F_2 structures observed in plagioclase and garnet porphyroblasts. Early F_2 structures likely formed as upright structures since

S_1 likely developed as a horizontal, bedding parallel structure. These structures progressively tightened and became attenuated wherein regional scale parasitic F_2 structures are currently present as antiforms and synforms overturned towards the southwest. Timing of overturning the regional F_2 structure remains difficult to deduce. It likely occurred prior to northeast-over-southwest folding associated with D_3 since those structures and the northeast-over-southwest vergence remains preserved.

Development of the inverted northeast-dipping contact metamorphic aureole is interpreted to be associated with the late stages of D_2 since the aureole is folded by F_3 and not by F_2. Although it is difficult to deduce the exact mechanism which caused this metamorphic aureole, it is the result of a composite deformation event associated with three geologic processes: 1) thrusting of relatively deeper and hotter YTT rocks to the southwest over the Kluane schist, 2) structural stacking of the Kluane schist and YTT as a result of regional scale folding, and 3) thermal heating of the schist associated with emplacement of the RRB along the Kluane schist/YTT contact. Metamorphism associated with this composite D_2 deformation event (*i.e.,* M_2) is associated with moderate pressure and temperature conditions at approximately 7 kbar and 500°C, therein placing the schist at a maximum depth of approximately 24 kms during D_2 (2.8 g/cm^3 crustal density; Winter, 2001).

From the D_2-related structures described above, the Kluane schist is interpreted as a mylonite with a well-developed L-S tectonite fabric (L = lineation; S = schistosity). If the dominantly east-southeast, shallowly plunging D_2 linear fabrics are used as the direction of D_2 shearing and, the dominantly northeast-dipping S_{2a} is used as the orientation of the D_2 shear zone boundary then that shear zone was an oblique sinistral structure which is what relative plate motions of Engebretson (1985) would predict for the region during the *ca.* 82 Ma D_2 event (Israel *et al.,* 2011a).

D_3 deformation is associated with a consistently northeast-over-southwest folding event. Continued intrusion of the RRB occurred during this event resulting in further destruction of the YTT/Kluane schist contact. F_3 folding of the northeast dipping inverted metamorphic aureole occurred during this deformation event.

Field observations and statistical analysis of S_{2a} and F_3 axial plane measurements indicate a broad, open, regional scale F_4 fold plunges shallowly towards the east-southeast in the Kluane schist (Figure 27 and 28). F_4 folding is interpreted to have been accommodated, in part, by shear along S_{2a} planes with low cohesion. This process is referred to as flexural slip wherein the layers and their contact surfaces act as brittle-ductile shear zones (Figure 41; Ramsay and Huber, 1987). En echelon tension gash arrays can develop within layers when bending is accommodated by flexural flow. The relative sense of shear within the layer can be inferred

from the orientation of the tension gashes relative to layering and the rotation of the gashes as indicated by their S- or Z-shape. The sense of shear related to the formation of the regional scale F_4 fold must be related to the sense of shear necessary to accommodate the flexural bending. Lin *et al.* (2007) indicate ridge-in-groove striations approximate the in-situ shear direction. L_{RG} orientations vary considerably within the study area and do not provide a definitive, consistent shear direction (Figure 37C). The significance of this lack of preferred orientation is ambiguous. The relatively small scale dome-and-basin fold patterns, deformed quartz-rich tension gash veins, and L_{RG} structures are interpreted as D_4-related structures which formed as the result of flexural slip associated with sub-horizontal, northeast-southwest compression and the formation of a broad, open regional scale F_4 fold. Contemporaneously during F_4 folding, this part of the Cordillera became host to significant felsic plutonism associated with the Hayden Lake intrusive suite (HLIS; *ca.* 55 Ma; Israel *et al.,* 2011a; Mortensen and Hart, 2010). The author believes the distinction between M_2 and M_4 will only be recognized by detailed geobarometric studies that target metamorphic minerals within the corresponding D_2- and/or D_4-related metamorphic aureoles that grew syn- and/or post-tectonically (*e.g.,* micas, hornblende, plagioclase, and/or garnet).

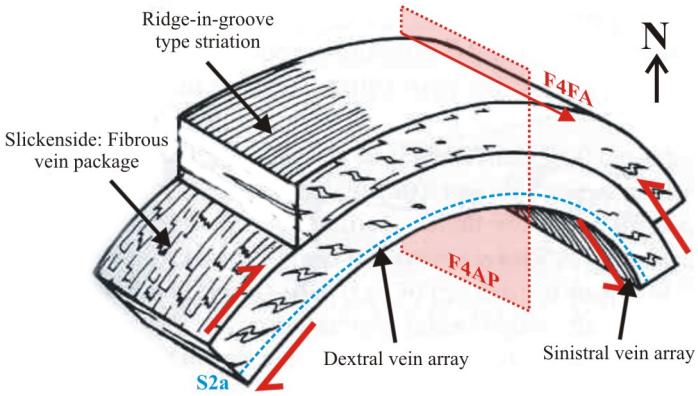

Figure 41: Schematic drawing of flexural slip structures associated with a broad, open anticline. Ductile ridge-in-groove type striations (L_{RG}) and fibrous mineral lineation packages lie on the sheared layer planes (slickensides; S_{2a}). En echelon tension gash arrays develop within layer parallel brittle-ductile shear zones. The relationship of the fold axis (F_4FA) and axial plane (F_4AP) with respect to a broad, open anticline fold structure (F_4 fold) are indicated. Modified after Ramsay and Huber (1987).

Nelson and Colpron (2007) state that subduction had all but ceased off the west coast of Canada by *ca.* 40 Ma. Motion along the Canadian Cordillera and within the North American plate margin is now translated into dextral strike-slip faulting associated with the Queen Charlotte fault and its subordinate splays (*e.g.,* Denali fault system).

4 Uranium-lead zircon geochronology

4.1 Introduction

Uranium-lead (U-Pb) zircon geochronology was undertaken for this study to constrain the age of deposition, provenance, magmatic crystallization, and overgrowth ages of zircon grains hosted within the meta-sedimentary Kluane schist and deformed and undeformed granitic samples. As well, zircon grains from the cordierite-bearing Kluane gneiss unit, which occupies a significant portion of the boundary zone between the schist and RRB, were analyzed to better understand the affinity of this unit. The importance of penetrative overgrowth rims on detrital and magmatic zircons will be clarified by determining the crystallization and/or metamorphic ages for deformation and magmatic events associated with the schist and associated plutonic rocks. Ages obtained from these samples will add important geochronological age data for this part of the Canadian Cordillera and will also add critical age data required to better understand the evolution and paleo-tectonic setting of the Kluane schist.

Ages reported in this study are derived from U-Pb zircon laser ablation-inductively coupled plasma mass spectrometry (LA-ICPMS) completed at the Jack Satterly Geochronological Laboratory within the Department of Geology at the University of Toronto and, at the Core Research Equipment and Instrument Training (CREAIT) Network within the Department of Earth Sciences at Memorial University. As is commonly the case when dealing with different laboratories, sample processing methods and analytical techniques may vary slightly; however, the data-set presented here is a homogeneous compilation since both laboratories adhere to similar procedures. When deemed relevant, any variation in data collection and/or data processing is indicated.

4.2 Geochronological age dating

Isotopes are nuclides (atoms) of the same element with different numbers of neutrons. Nuclides can exist as both stable and unstable, wherein unstable nuclides undergo radioactive decay (*i.e.,* radioactive isotopes). Decay rates for unstable parent nuclides to stable daughter nuclides are proportional to the number of parent nuclides present at any time t (Dickin, 2005). Radioactive decay can be expressed in terms of a radioactive isotopes half-life, which is the time required for half of the parent nuclides to decay. The number of decayed parent nuclides is equal to the number of daughter nuclides formed. If the number of daughter nuclides at time $t = 0$ is D_o, then the total number of daughter nuclides after time t is given as:

$$D = D_o + n\left(e^{\lambda t} - 1\right) \tag{1}$$

The above equation forms the principal basis for geochronological age dating. For this study, the method of U-Pb age dating was used. This method represents the most precise and most accurate geochronometer for determining the age(s) of terrestrial and extraterrestrial rocks (Faure and Mensing, 2005).

4.2.1 Uranium-thorium-lead (U-Th-Pb) zircon geochronology

Lead exists as four isotopes one of which, ^{204}Pb, is non-radiogenic (*i.e.,* common Pb). The other three, ^{206}Pb, ^{207}Pb, and ^{208}Pb are the final decay products of three intricate decay sequences from U and Th (see Table 1). Minerals that readily incorporate large concentrations of U and very low concentrations of initial, common Pb are monazite, uraninite, and zircon. Uranium, Th, and Pb are incorporated in the continental crust because they concentrate in early melts due to their incompatible behaviour. Notably, zircon is more abundant in intermediate to acidic rocks (*i.e.,* $SiO_2 \geq 52$ wt. %) than monazite and uraninite. Most importantly, zircon concentrates U moderately but almost completely excludes Pb. Therefore, zircon is typically analyzed in U-Pb age dating (Winter, 2001; Dickin, 2005).

Table 1: U-Th-Pb parent-daughter decay sequences, half-lives, and decay constants. Adapted from Jaffey *et al.* (1971) and Dicken (2005).

Parent-daughter decay sequence	Half-life, $t_{\frac{1}{2}}$ (Byr)	Decay constant (yr^{-1})
$^{238}U \longrightarrow {}^{206}Pb$	4.47	1.55125×10^{-10}
$^{235}U \longrightarrow {}^{207}Pb$	0.704	9.8485×10^{-10}
$^{232}Th \longrightarrow {}^{208}Pb$	14.01	0.49475×10^{-10}

As an example of how to apply age dating equations to a geological problem, Dicken (2005) exhibits an igneous system that crystallized at age t from a magma. The nuclides produced from each decay sequence are substituted into equation 1 and ^{204}Pb is then divided through the equation to obtain isotopic ratios rather than absolute abundances (Dickin, 2005).

$$\left(\frac{^{206}Pb}{^{204}Pb}\right)_P = \left(\frac{^{206}Pb}{^{204}Pb}\right)_I + \frac{^{238}U}{^{204}Pb}\left(e^{\lambda_{238}t} - 1\right) \tag{2}$$

$$\left(\frac{^{207}Pb}{^{204}Pb}\right)_P = \left(\frac{^{207}Pb}{^{204}Pb}\right)_I + \frac{^{235}U}{^{204}Pb}\left(e^{\lambda_{235}t} - 1\right) \tag{3}$$

$$\left(\frac{^{208}Pb}{^{204}Pb}\right)_P = \left(\frac{^{208}Pb}{^{204}Pb}\right)_I + \frac{^{232}Th}{^{204}Pb}\left(e^{\lambda_{232}t} - 1\right) \tag{4}$$

In Equations 2, 3, and 4, P and I represent abundances of the corresponding nuclides at present and initial times. These decay equations are eventually used to construct isochron diagrams. It was recognized early on by Nicolaysen (1961) that Equation 1 is the same as the equation for a straight line (*i.e.,* y = c + xm) where the intercept, c, is the initial ratio of unstable parent nuclide to stable nuclide. If the above example system remains closed, the initial ratio in a suite of co-magmatic minerals will define a line termed an isochron (Nicolaysen, 1961; Dicken, 2005). The slope of this line, $m = e^{\lambda t} - 1$, will subsequently provide the age of the minerals. However, the closed system assumption may be invalid given that the U-Pb system rarely remains closed in silicate rocks due to the mobility of U and Pb in both low grade metamorphism and surface weathering conditions (Dickin, 2005).

Since the U-Pb system has two separate decay sequences with common parent and daughter nuclides (see Table 1), age information can be extracted from a disturbed system. To attain this information, minerals that strongly incorporate U at the time of formation but not Pb should be analyzed (*e.g.,* zircon; Dickin, 2005). Equation 2 can then be altered to:

$$^{206}Pb* = \ ^{238}U\left(e^{\lambda_{238}t} - 1\right) \ldots and/or \ldots \frac{^{206}Pb*}{^{238}U} = \left(e^{\lambda_{238}t} - 1\right) \tag{5}$$

where Pb$*$ is radiogenic lead only. Minerals that actually do remain as closed systems will give concordant values of t when their isotopic compositions are substituted into Equation 5. Concordant ages plotted graphically together will then form a curve, formally termed concordia by Whetherill (1956; Dickin, 2005). Conversely, discordant ages plotted graphically together will form a line termed discordia. The upper intersection of discordia and concordia represents the minerals age of formation and the lower intersection represents the time of a thermal event that caused lead loss from the minerals (Dickin, 2005). The shape of concordia reflects the behaviour of the U-Pb system wherein the consumption of parent and production of daughter is reflected graphically. More specifically, since ^{235}U decays faster than ^{238}U (see Table 1), the

$^{207}Pb/^{235}U$ ratio will always be larger than the $^{206}Pb/^{238}U$ ratio and the difference will become greater with time. This results in the characteristic concave shape of concordia (Winter, 2001).

Concordia diagrams are typically used to display U-Pb isotopic data, however, these diagrams can become cluttered as the number of grains analyzed increases. Thus, it has become the norm to present large data-sets, which span a large time-frame, on histograms or probability density distribution diagrams. Fedo *et al.* (2003, pg. 282) state that it is important to note there are two critical limitations to presenting data on a histogram:

1. Errors of age measurements are not presented, hence, measurements containing large error may be presented with measurements containing low error; and
2. Bin sizes are arbitrary.

With respect to probability density distribution diagrams, which were eventually used to circumvent the above limitations, these diagrams introduce errors in the age data and produce a probability distribution of the entire dataset. The main disadvantage of this diagram is that frequency and proportion are represented in the area beneath a curve rather than height, as is the case for histogram diagrams. Hence, the amount of measurements represented in each mode is not clearly demonstrated (Fedo *et al.,* 2003). It appears from recent articles that a combination of both histograms and probability density distributions has become a typical display for large data-sets. This study will use the above methodology to present and interpret the corresponding data-set.

4.3 Methodology

4.3.1 Sample preparation and mineral separation

In the field, approximately 20 kilogram rock samples were collected and placed in separate sealed containers for transport to the laboratory. At the laboratory, sample processing began with reducing oversized samples to rock chips. After rock crushing and disc milling, any piece of equipment that may have been contaminated during processing is thoroughly cleaned using: compressed air hoses, high-efficiency particulate air filters and vacuums, a hand drill with polishing steel wire brush attachment, and ethanol.

The next stage of sample processing involves mineral separation using a Wilfley^{TM} table. This table is used to divide the sample into heavy and light mineral fractions using a wet, gravity-based separation technique. The heavy mineral concentrate produced after this step is then transferred to filter paper, flushed with ethanol to remove any moisture, and placed under a heat lamp to completely remove the residual moisture. Once dry, the concentrate

is passed through a 40 μm mesh sieve to separate fine and coarse grain particles. The fine grained concentrate is then placed in a glass vial filled with a high specific gravity solution (*e.g.,* methylene iodide). During this step, separation occurs by allowing the heaviest particles to settle to the bottom of the vial while the lightest particles are left floating on top. The heavy mineral concentrate continues with magnetic separation.

Initial magnet separation may commence with either a large hand magnet or a Frantz^{TM} Canister Separator. This process separates the magnetic concentrate and any excess iron filings (that may have been produced during previous sample processing stages) from the less magnetic concentrate. Both techniques appear to produce the same result.

The second stage of magnetic separation involves use of the Frantz Isodynamic^{TM} magnetic separator. This apparatus contains a large Frantz^{TM} Canister Separator with a narrow gap through the middle of the magnet. The less magnetic concentrate is fed from one end of the magnetic field and allowed to travel the full length of the apparatus, along a vibrating aluminum trough with a side tilt. The more magnetic material is drawn in towards the uptilt part of the gap where the magnetic attraction is greatest. As grains travel along the gap, a divider separates magnetic from relatively non-magnetic fractions (*e.g.,* zircon, monazite, titanite, etc.) until they are collected in a plastic container at the opposite end of the apparatus. Frantz Isodynamic^{TM} magnetic separation is either a one- or two-step process involving: 1) Initial Frantz^{TM} separation and 2) Final Frantz^{TM} separation.

Initial Frantz^{TM} separation involves setting the machine at a side tilt (10 °) and running the magnet at variable amperages (0.5, 1.0, and 1.7 ampere). Final Frantz^{TM} separation involves setting the machine at an amperage (1.7 ampere) and varying the degree of side tilt of the trough (5 °, 3 °, 1 °, and 0 °). After the apparatus is modified, fractions are collected and the less magnetic fraction continues with processing. Regardless of following the one- or two-step process for the second stage of magnetic separation, the less magnetic fraction is then handpicked for zircon grains using a binocular microscope. However, to reduce sampling bias, Final Frantz^{TM} separation may be omitted and zircon fractions produced from Initial Frantz^{TM} separation are randomly deposited onto a grain mount as opposed to hand-picked using a binocular microscope (Israel *et al.,* 2011a). The omission of Final Frantz^{TM} separation reduces sample bias by excluding human error that arises when picking zircon grains (*e.g.,* the largest or most pristine looking grains will be the most obvious zircon grains to pick). The recognition and omission of this human error is important when analyzing detrital samples because sedimentary rocks may retain complex provenance information that can only be studied in detail by analyzing the multitude of zircon grain populations that may not be obvious to the human eye.

Approximately $60 - 100$ zircon grains per sample were selected for analysis to provide a reasonable quantity for each sample. Colour, morphology, and inclusions were documented to characterize any observable populations. Grains were then mounted on double sided tape attached to a glass slide. After characterization, approximately ten zircon grain standards per grain mount were mounted with each sample. The standard zircon grains used are DD-8310 and 09-TOA-180. They were chosen as reference zircons because their ages were previously determined using isotope dilution-thermal ionization mass spectrometry (ID-TIMS) and chemical abrasion-TIMS; their ages are 2733.0 ± 0.9 Ma (Das and Davis, 2010) and 98.26 ± 0.03 Ma [unpublished internal reference material; V. Bennett pers. comm., 2010], respectively. Analysis of a standard allows for correction of instrumental fractionation of $^{207}Pb/^{206}Pb$ and $^{206}Pb/^{238}U$. Two sets of analyses were completed for the four meta-sedimentary samples. In the first analyses, whole grains attached to double sided tape were ablated. This first set of analyses was undertaken to investigate the abundant disseminated opaque material observed within a large majority of the zircon grains. The second set of analyses was undertaken on all meta-sedimentary, igneous, and gneiss samples. This step was preceded by mounting the samples in a hardening epoxy and polishing them before ablation. A 1.5 cm diameter puck-shaped plastic cylinder was placed over the glass slide and a hardening epoxy was poured into the cylinder and allowed to harden over night. The puck was then polished either manually (3, 1, and 0.3 μm polishing paper) or automatically (6, 3, 1, and 0.3 μm polishing paper). Before and after polishing steps, the puck was cleaned in an ultrasonic bath to remove any grit produced during polishing. When grain surfaces were mostly free of scratches and grit, the puck was coated in a gold-palladium mixture or carbon in preparation for imaging using a scanning electron microscope. The polishing steps allowed for accurate imaging and characterization of magmatic zircon populations and epitaxial relationships (*i.e.,* core *vs.* rim). The recognition of morphological differences between magmatic and epitaxial features assists intragrain targeting of the laser beam during LA-ICPMS. Bennett and Tubrett (2010, p. 48) state that erronously targeting overlapping age domains "produces isotopically heterogenous data which, typically, is a significant contributor to U-Pb discordance" using the LA-ICPMS procedure.

4.3.2 Scanning electron microscope (SEM)

The SEM apparatus typically operates in either backscattered electron (BSE) or cathodoluminescence (CL) mode. BSE mode operates by scanning a sample with a high-energy beam of electrons that scatter off atoms in the sample. Detection of the scattered electrons reveals a contrast in atomic number of regions on the sample wherein a high atomic number corresponds to a high amount of electrons reflected (*i.e.,* bright). This type of imaging is formally termed

BSE imaging and it is widely recognized as a powerful tool for studying zonation in minerals (Corfu *et al.,* 2003). CL mode operates in the same manner as BSE mode except the CL detector appears to provide the best resolution of internal textures in the sample being analyzed. Basically, the emission of CL is attributed to the electronic transitions of 5d-electron transition elements, the 4f-electron electronic transitions of the trivalent rare earth elements, the vibrational luminescence of the uranyl ion, or defect-related phenomena (Corfu *et al.,* 2003).

Electron microscopy was undertaken using a JEOL JSM-840 SEM (University of Toronto) and a FEI Quanta 400 environmental SEM (Memorial University). The presence of zircon and other minerals was confirmed using energy dispersive x-ray (EDX) analysis on the SEM. EDX analysis works in BSE mode by bombarding the sample with electrons and the energies and intensities of emitted x-rays are then measured. These x-rays are the result of electrons ionizing core shells of the atoms present in the sample. Since the resulting shell transitions are characteristic of each chemical element, the resulting x-rays energies are characteristic of the specimens elemental composition, and the intensity of the x-rays is directly associated with weight fraction of each of those chemical elements. The BSE images and chemical spectra produced from the zircon grains chosen for LA-ICPMS reveals various textural, morphological, and compositional features.

The SEM at Memorial University is also equipped with mineral liberation analysis (MLA) software from JKTech at the University of Queensland, Australia. This software allows a quantitative evaluation of the abundances, associations, sizes and shapes of minerals in an automated, systematic manner. MLA uses the BSE technique to evaluate an average atomic number to discriminate grain boundaries and then it uses various x-rays to classify the grains identified as particular minerals. This software is invaluable when normal optical microscopy does not easily reveal the presence of the particular minerals being investigated. MLA was undertaken on one sample during the course of this study (*i.e.,* 10-VLS-136). During normal sample processing and mineral separation techniques of this sample no zircon grains were identified. After MLA analysis, three zircon grains were identified the results of which are discussed in detail later in this chapter. After BSE imaging, chemical spectra analyses, and MLA investigations the epoxy pucks were transferred to the LA-ICPMS instrument to begin analysis.

4.3.3 Laser ablation-inductively coupled plasma mass spectrometry (LA-ICPMS)

LA-ICPMS is a common analytical technique used in the study of earth sciences today (Longerich, 2008). As the acronym suggests, the technique involves two instruments: 1) a laser ablation (LA) system and 2) inductively coupled plasma mass spectrometer (ICPMS). The LA

portion of the apparatus consists of a laser and microscope, an airtight cell to host a sample, and tubing flushed with helium (He) gas. In the airtight cell, a laser beam is directed onto a sample that is consequently converted into an aerosol of particles. These particles are then carried by He gas into the ICPMS. In the ICP, He gas is heated to a high temperature to form plasma. This plasma is essentially a gas-like fluid but contains many free electrons and ions. The particles liberated from the sample are brought to the plasma where they are vaporized into very fine particles and ionized. The ionized particles enter the MS, which is under vacuum, where they are separated according to their masses. The separation of ions based on masses is an important step since it identifies elemental and isotopic compositions (Longerich, 2008). The intensity of the ion beam (ions/sec) is then converted into an electrical signal that is measured and recorded. Recording the intensity of the signal provides a concentration of the corresponding element and its isotopic composition in the sample.

LA-ICPMS U-Pb zircon geochronology was undertaken at the University of Toronto using a VG Plasma quadrupole mass spectrometer with a 213 nm Coherent laser system. At Memorial University, the instrument is a Finnigan ELEMENT XR, high resolution double focusing magnetic sector inductively coupled plasma mass spectrometer with a GEOLAS 193 nm excimer laser system. The methodology for LA-ICPMS followed during analyses involved two steps:

1. Rastering a 10 to 40 μm diameter beam over the sample surface at a velocity of 1 to 60 μm/sec. The laser was set at 70 % output with a laser repetition of 5 to 10 Hz. Four raster passes were completed on each sample surface. This step was undertaken to clean the sample surface from any debris that may have been projected from nearby analyses and remove the outer layers of zircon, which could have suffered Pb loss.

2. A 10 to 40 μm diameter beam was then fired over a stationary spot and/or line at the middle of the previous raster area for 30 seconds. The laser beam settings were the same as step one. Caution was taken at this step to target spots on the grains free of inclusions and cracks. This step was used for primary data collection of selected elements.

Primary data collection during analyses involved the measurement of strontium (^{88}Sr), thorium (^{232}Th), ^{238}U, ^{207}Pb, and ^{206}Pb intensities. Once primary data collection was completed, the averages of ^{207}Pb/^{206}Pb and ^{206}Pb/^{238}U ratios were calculated for a selected window of data. For every three unknown sample zircon grains analyzed, one standard zircon grain was analyzed. This process was followed because the ablation process usually biases the calculated ^{207}Pb/^{206}Pb and ^{206}Pb/^{238}U ratios; therefore, a correction for the calculated biases is interpolated between each pair of standards. This protocol ensures the "efficiency of the mass bias correction as well as the correction for laser-induced mass fractionation" (Bennett

and Tubrett, 2010, pg. 50). The final values include errors in both the unknown sample and the known standard measurements. To calculate the isotopic ratios, basic radiogenic isotopic principles fundamental to geochronology described in previous sections are used.

4.4 Sample descriptions and results

4.4.1 Introduction

Four schist, three igneous, and one gneiss sample were collected for U-Pb zircon LA-ICPMS during the summers of 2009 and 2010 (Figure 42). All samples retain clearly defined contact relationships with adjacent units and/or tectonic fabrics. Sampling of the schist was undertaken to investigate and provide age constraints on the source(s) of the schist's protolith. The igneous samples were chosen because they constrain syn- and post-kinematic tectonic fabrics preserved in the schist. The gneiss sample was chosen to investigate the complexity and diversity of zircon grains observed within the unit. Complete U-Pb zircon LA-ICPMS data-sets are provided in Appendix B.

While under the supervision of various experts at both laboratories, it became clear that low Pb and U concentrations were recorded in all samples. During LA-ICPMS analysis, background U and Pb levels were kept at low levels and laser energy was kept high to allow the collection of usable, but less precise age data. When elemental concentrations did not exceed background levels, the data was deemed unusable and not included in any of the following results and/or interpretations. Where isotope mass 204 levels exceeded acceptable background levels, this data was rejected since the value likely represents excess common Pb. It is noted in the text when data presented below exceeds 10 % discordance. Quoted ages are based on $^{206}\mathrm{Pb}/^{238}\mathrm{U}$ since $^{207}Pb/^{206}Pb$ ages are relatively imprecise for late Phanerozoic samples and also more susceptible to contamination (D. Davis pers. comm., 2010).

4.4.2 Kluane schist samples

The Kluane schist U-Pb zircon data-set presented below represents a reconnaissance scale investigation to better understand the complexity of the zircon grain population(s) found in the schist. A statistically more robust U-Pb detrital zircon LA-ICPMS study of the schist was undertaken by Israel *et al.* (2011a). Data from that study is carefully integrated and compared to data for the current study.

The schist samples are located in the northwestern domain of the study area (Figure 42). Two samples were collected from each of the muscovite-rich schist (09-VLS-052 and 066) and

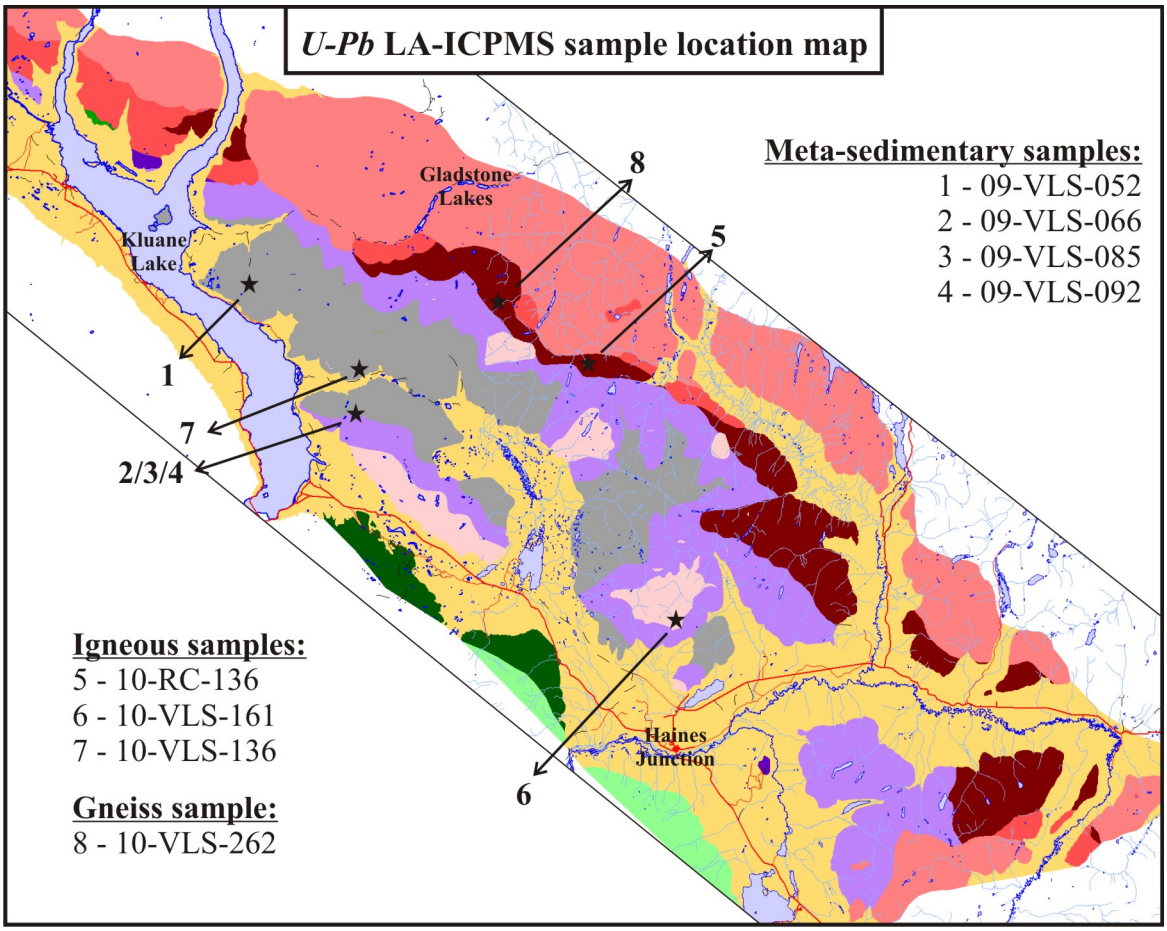

Figure 42: Location map of 2009 and 2010 U-Pb zircon LA-ICPMS samples.

biotite-rich schist (09-VLS-085 and 092). Initial optical and SEM investigations in late-2009 revealed a lack of epitaxial relationships (*i.e.,* core *vs.* rim) in zircon grains for these samples. Subsequent high quality imaging followed up in 2010 by this study and Israel *et al.* (2011a) indicate a clear relationship between xenocrystic cores and overgrowth rims on a majority of the zircon grains. However, U-Pb LA-ICPMS targeting on the schist samples was complete prior to obtaining the high quality images. Therefore, the U-Pb age data-set presented below likely reflects the collection of overlapping age domains; however, the data presented here is in fact similar to age data presented by Israel *et al.* (2011a).

Two hundred and twenty-six grains were analyzed from four samples. Fifty-seven of those analyses are from polished grains and one hundred and sixty-nine analyses are from unpolished grains. Notably, almost all analyses exceed 10 % discordance. The discordance is likely the result of erroneously targeting overlapping age domains, which as noted above is a significant contributor to U-Pb discordance (Bennett and Tubrett, 2010). As such, a significant amount of prudence should be taken when interpreting and integrating this data with that of Israel *et*

al. (2011a).

Sample 09-VLS-052 yields a bimodal signature with dominant clusters and peaks at 89 – 104 Ma and 169 – 186 Ma (Figure 43A and 44A-B). Single zircon ages at 154, 212, and 241 Ma indicates a possible increase in the signature of the older peak width. A single zircon age exists at approximately 349 Ma. Not shown here is one Early Proterozoic analysis. Sample 09-VLS-066 yields a relatively precise bimodal signature with dominant clusters and peaks at 95 – 101 Ma and 173 – 209 Ma (Figure 43B and 44C-D). Sample 09-VLS-085 yields a less obvious bimodal signature with dominant clusters and peaks at 70 – 86 Ma and 134 – 157 Ma (Figure 43C and 44E-F). Single zircon ages at 96, 105, and 122 Ma just outside both time intervals indicates a possible increase in the signature of both peak widths or the presence of one broad population. A single zircon age exists at 312 Ma. An age of 70 Ma for one grain in this sample records the youngest age reported for this sample. Not shown here are two Late Archean analyses. Sample 09-VLS-092 is more complex, showing a multi-modal signature (Figure 43D). A prominent peak exists from 71 – 82 Ma and multi-modal peaks exist at 120 – 149 Ma and 184 – 200 Ma (Figure 44G and H). Single zircon ages at 90, 99, and 105 Ma between the two youngest intervals indicates a possible increase in the signatures of both peak widths or the presence of one broad population. A single zircon age exists at 229 Ma.

Concordia, histogram, and probability age distribution diagrams for a majority of the zircon grains show ages that span from as young as Late Cretaceous (70 Ma) to as old as Early Carboniferous (350 Ma). The data appears to be less robust in the older half of this time span. A broad view of the entire zircon data-set appears to exhibit a bimodal peak signature with ages ranging from 70 – 104 Ma and 134 – 212 Ma. Older ages for single zircon grains exist at 229, 241, 312, and 349 Ma. Subordinate ages include three Early Proterozoic to Late Archean ages (*ca.* 2346, 2686, and 2691 Ma). Note that 09-VLS-052 and 09-VLS-066 patterns are similar. 09-VLS-085 and 09-VLS-092 are also statistically indistinguishable from each other except for a small portion of data that exists around *ca.* 200 Ma (Figure 44G). Notably, all samples appear to have a similar mid-Cretaceous peak and, all samples except for 09-VLS-085 appear to have a similar Early to Middle Jurassic peak (Figure 44).

Hoskin and Black (2000, p. 430) state that Th/U values for igneous zircon are greater than 0.5 and less than 0.1 for recrystallized, metamorphic zircon. However, Harley *et al.* (2007, p. 28) state that Th/U values for metamorphic zircon are variable to high. Thus, caution should be taken when integrating Th/U values in any attempt to establish a igneous *vs.* metamorphic affinity to specific analyses. More robust conclusions are drawn from data that consolidates chemical and textural criterion. Israel *et al.* (2011, p. 114) note targeted overgrowth rims from their detrital zircon study correspond to high concentrations of U (879 – 8129 ppm) and

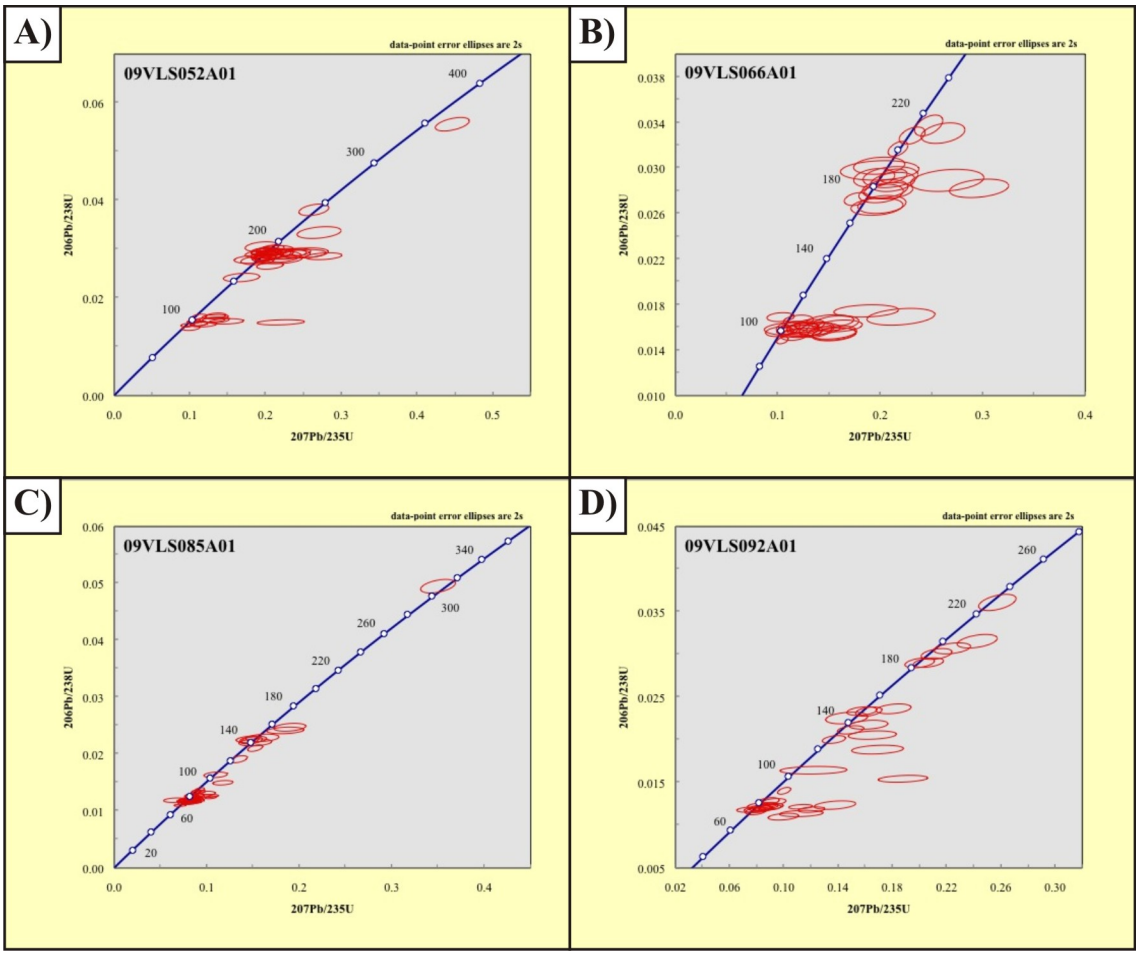

Figure 43: U-Pb concordia diagrams for analyses of four schist samples 09-VLS-052 (A), 09-VLS-066 (B), 09-VLS-085 (C), and 09-VLS-092 (D). Two sigma uncertainty ranges are documented for all ages plotted on concordia diagrams. Figure 42 for locations of samples.

very low Th ($4-88$ ppm). Calculated $^{206}Pb/^{238}U$ concordia ages for those overgrowth analyses yield a metamorphic age of 82.10 $\pm$ 0.65 Ma. Where Israel *et al.* (2011a) encounter an ambiguity of unknown core *vs.* rim relationship in sample 08DM126, they interpret the youngest age peak/cluster of that sample as a metamorphic age since it overlaps with the calculated $^{206}Pb/^{238}U$ concordia age introduced above. The current study interprets the youngest age peak observed in samples 09-VLS-085 and 092 (*ca.* $70-86$ Ma) as a metamorphic age similar to that of of sample 08DM126. Israel *et al.* (2011a) also found that the youngest accurate age for xenocrystic cores (with relatively higher Th/U values) that preserve internal zoning textures (*e.g.,* oscillatory, sector, and diffuse) is 94.9 $\pm$ 1.1 Ma. This age overlaps in time with the obvious peaks and clusters from all samples presented for this study. From this one analysis, Israel *et al.* (2011a) place a lower age constraint for deposition of the Kluane schist protolith at *ca.* 95 Ma.

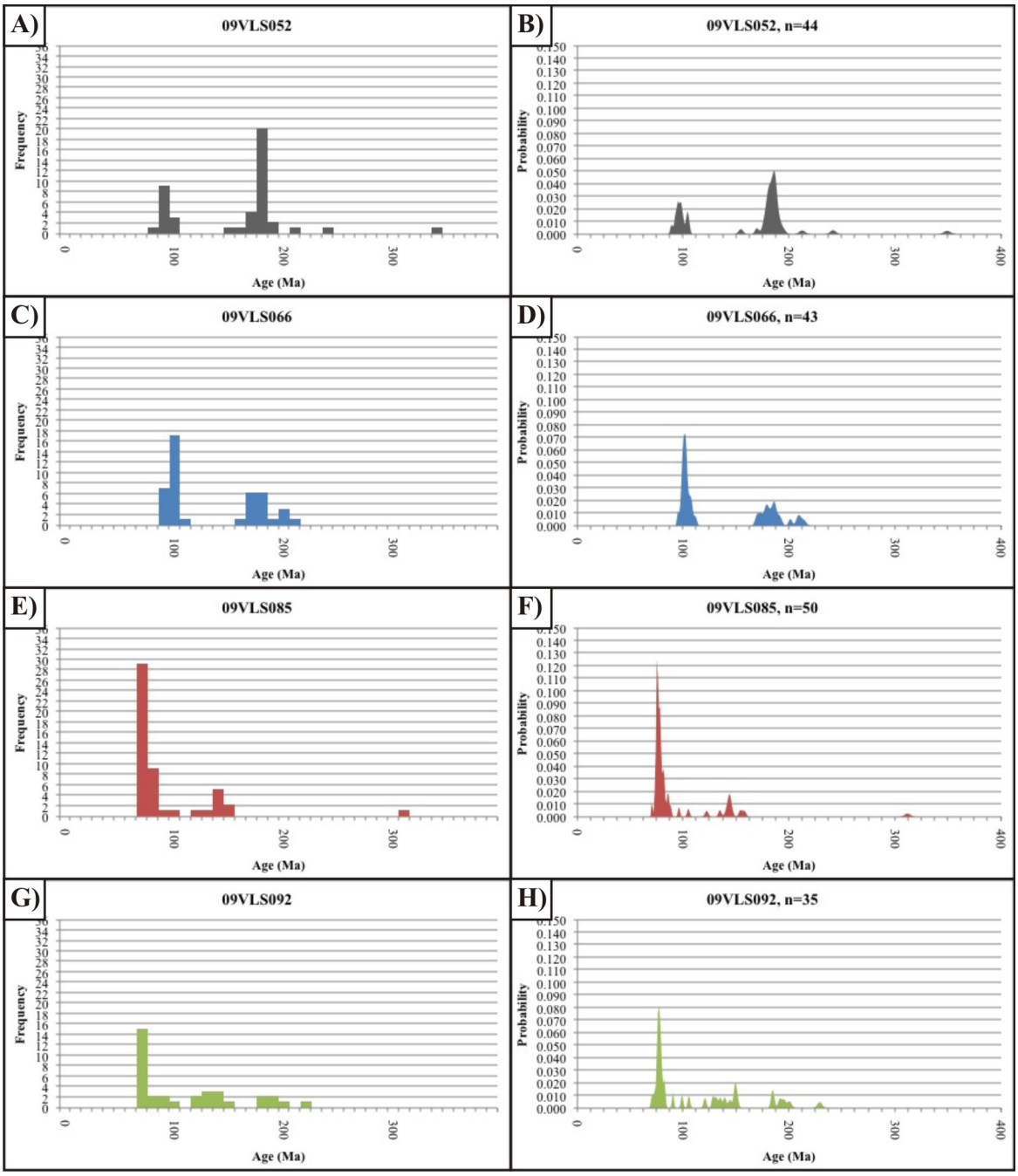

Figure 44: Histogram (left) and probability distribution (right) diagrams showing age spectrum of four schist samples. 09-VLS-052 (A-B), 09-VLS-066 (C-D), 09-VLS-085 (E-F), and 09-VLS-092 (G-H).

The detrital zircon age spectrum from the Kluane schist sample of Israel *et al.* (2011a) are similar to regionally proximal igneous bodies. These igneous phases include: the Late Triassic to Eocene Coast plutonic complex, the *ca.* $104 - 98$ Ma Nisling Range granodiorite and, the *ca.* $190 - 180$ Ma Aishihik batholith. All of these intrusions are located east of the schist indicating the schist was likely sourced from uplifted rocks of YTT. Proterozoic to Archean

detrital zircon ages reported here and in Israel *et al.* (2011a) confirm YTT as a significant source for the Kluane schist since it retains an identical older detrital zircon age peaks.

4.4.3 Igneous samples

4.4.3.1 Sample 10-RC-136

Sample 10-RC-136 was collected from a meter thick, undeformed, leucocratic porphyritic biotite-hornblende-tonalite dyke. This dyke cross-cuts foliated cordierite-bearing Kluane gneiss northwest of Killermun Lake (Figure 42 and 25). The dyke is host to several randomly oriented, decimeter scale oblate mafic enclaves composed of biotite and hornblende. Age data calculated for this dyke was originally hypothesized to provide a post-kinematic age constraint for all tectonic fabrics recorded in the gneiss.

BSE and CL images reveal all zircon grains from this sample are anhedral to subhedral in form and, they all retain penetrative overgrowth rims texturally different from the xenocrystic cores (Figure 45). Twenty-two analyses were completed on sixteen zircon grains from this sample; six overgrowth rims were targeted. Eight analyses were less than 10 % discordant, three of which are targeted rims. One of the 'targeted' rims was contaminated by a proximal xenocrystic core age domain and therefore, it is excluded from the plots presented below. All targeted xenocrystic cores remain at least 25 million years older than the rims. Since no pristine, euhedral 'igneous' zircon grains were found, data from the most concordant overgrowth rims is used to calculate the age of the youngest zircon growth event for this dyke. The most concordant data (*i.e.,* between $92 - 106$ % concordant) indicates the overgrowth rims formed at 55.3 ± 1.7 Ma (Figure 46).

Of the eight relatively concordant analyses, three retain Th/U values ≤ 0.016 (Figure 47). Coincidentally, these three low Th/U values correspond to targeted overgrowth rims with an age range from 55 to 76 Ma. The targeted xenocrystic cores obviously record older ages but also record high and variable Th/U values (≥ 0.133) possibly indicating inheritance of zircon grains from a compositional and temporal range of source rock(s). The oldest age of the three low Th/U overgrowth rims represents data collected from overlapping age domains and therefore, it is excluded from the calculated $^{206}Pb/^{238}U$ concordia age presented in Figure 46. The two accurately targeted overgrowth rims used to represent the age of the youngest zircon growth event for the dyke (*i.e.,* 55.3 ± 1.7 Ma) show Th/U values indicative of recrystallization associated with metamorphism (*i.e.,* < 0.1). The dyke likely inherited a significant amount of zircon grains during its ascent and emplacement. Pressure and temperature conditions of the surrounding environment during emplacement was likely high enough to cause recrystallization

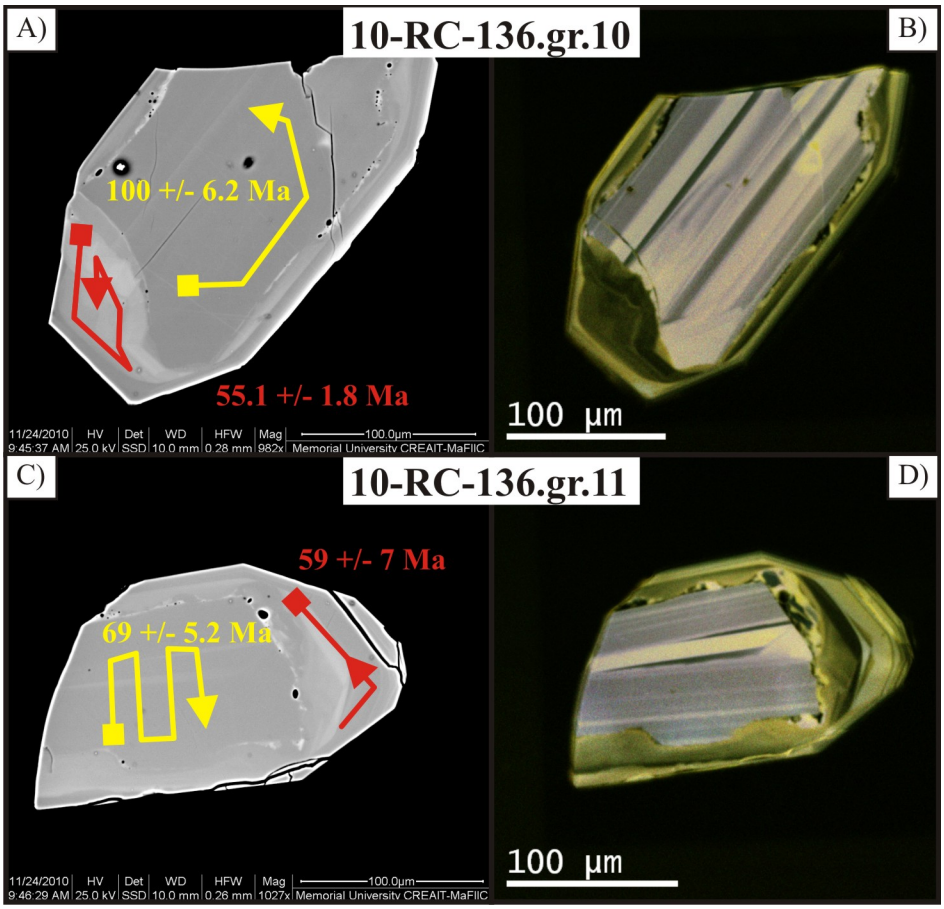

Figure 45: Example of BSE (left) and CL (right) images of zircon grains from sample 10-RC-136. Grain 10 (A-B) and 11 (C-D) showing BSE images labelled with line segments where targeted LA-ICPMS occurred. Corresponding U-Pb ages of analyses are labelled. Note the variability of the xenocrystic core ages and the similarity (within error) of the overgrowth rims.

and the formation of 'new', metamorphic zircon on the outer margins of the inherited grains. Although the dyke shows no textural signs of deformation, the metamorphic overgrowth rims may represent a cryptic or relatively later metamorphic event associated with deformation inferred to have overprinted the schist.

4.4.3.2 Sample 10-VLS-161

Sample 10-VLS-161 was collected on the southern margin of a kilometer scale granitic exposure of the Hayden Lake intrusive suite (HLIS) northwest of Paint Mountain (Figure 42 and 26). The outcrop is comprised of medium to coarse grained foliated hornblende-biotite-quartz-diorite (Figure 40). A foliation is present and defined by a compositional layering comprised of mafic layers with aligned, euhedral hornblende and biotite grains and felsic layers with dynamically recrystallized quartz and plagioclase grains. North of this outcrop the intrusion

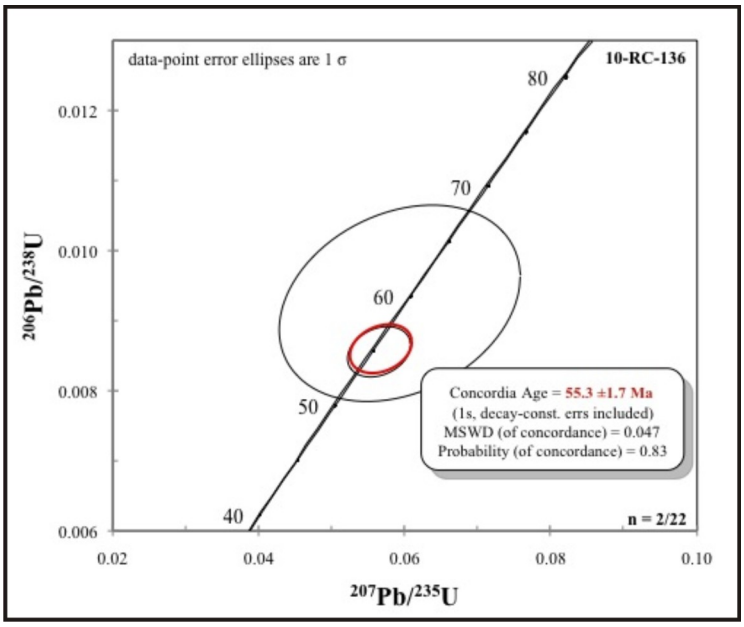

Figure 46: Concordia diagram for LA-ICPMS analyses from sample 10-RC-136. One sigma uncertainty ranges are documented for the two ages plotted on diagram. The age of metamorphism for these inherited grains from the dyke are believed to be associated with these two most concordant targeted overgrowth rims which provide a calculated $^{206}Pb/^{238}U$ concordia age of 55.3 ± 1.7 Ma (see red ellipse).

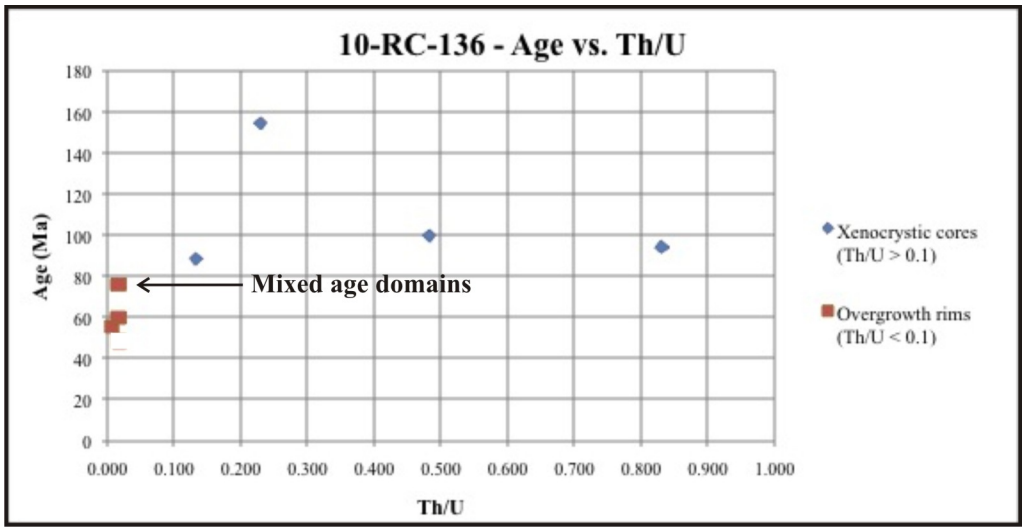

Figure 47: Plot of Th/U *vs.* age for zircon grains from sample 10-RC-136. All eight analyses are less than 10 % discordant. Note that an Early Proterozoic core is excluded from the plot to focus on the Phanerozoic data. Also note the tight cluster of Th/U values for the overgrowth rims (red squares) and the variability of Th/U values for the xenocrystic cores (blue diamonds). Analysis that collected age data from two or more age domains is indicated.

gradationally changes into a massive, non-foliated rock. South of this outcrop, the contact with the biotite-rich schist is buried beneath vegetation. In this area, the foliation of the schist strikes southeast-northwest and dips southwest whereas the orientation of the foliation

where sample 10-VLS-161 was collected strikes northwest-southeast and dips northeast. Age data calculated for this outcrop is interpreted as a syn- to post-kinematic age constraint for diorite deformation because: 1) the outcrop texture displays a well-developed foliation and, 2) the HLIS imparts local contact metamorphic aureoles onto the schist that are, in places, concordant and discordant to tectonic fabrics observed in the schist.

BSE and CL images reveal that all zircon grains from this sample are mostly subhedral to euhedral in form with doubly terminated prismatic morphologies (Figure 48). Except for two, all grains appear to lack penetrative overgrowth rims and, the two grains with noticeable rims retain sub-rounded to rounded xenocrystic cores likely indicating inheritance. Forty-four analyses were completed on forty-two grains from this sample; two overgrowth rims were targeted. Nineteen analyses were less than 10 % discordant, two of which are the targeted rims. These nineteen analyses range between 44 and 72 Ma with all except three analyses being less than 63 Ma. The two overgrowth rims are *ca.* 54 and 69 Ma. The youngest and most concordant fifteen doubly terminated zircon grains are interpreted to represent pristine, igneous zircon that document the crystallization age for this sample. These fifteen analyses are used to calculate a $^{206}Pb/^{238}U$ concordia age and $^{206}Pb/^{238}U$ weighted mean average age for the sample (Figure 49). Results indicate the sample crystallized at 55.0 $\pm$ 3.2 Ma.

Of the nineteen relatively concordant analyses, there is no unique Th/U value distinction between the two targeted overgrowth rims and the dominant population of grains that lack overgrowth rims (Figure 50). As is the case with xenocrystic cores targeted in sample 10-RC-136, there appears to be a range of Th/U values for the doubly terminated analyses in this sample ($0.124 - 0.404$). Since there is rarely any evidence of core *vs.* rim textures, the doubly terminated prismatic zircon grains from this sample are interpreted to represent original igneous zircon that are used to calculate the crystallization age for this sample. The Th/U values for both the xenocrystic cores and two rims from 10-VLS-161 remain similar and $\geq$ 0.124. This likely indicates the growth of new, igneous zircon as opposed to recrystallized, metamorphic zircon (*i.e.,* Th/U $<$ 0.1). Coincidentally, the calculated $^{206}Pb/^{238}U$ weighted mean average age presented above (55.0 $\pm$ 3.2 Ma) temporally overlaps with the calculated $^{206}Pb/^{238}U$ concordia age of sample 10-RC-136 (55.3 ± 1.7 Ma). These two ages are interpreted to represent contemporaneous felsic magmatism and metamorphism associated with intrusion of HLIS during deformation.

4.4.3.3 Sample 10-VLS-136

Sample 10-VLS-136 was collected from the center of a meter-scale thick deformed leucocratic tonalite dyke hosted within biotite-rich Kluane schist approximately seven kilometers east of

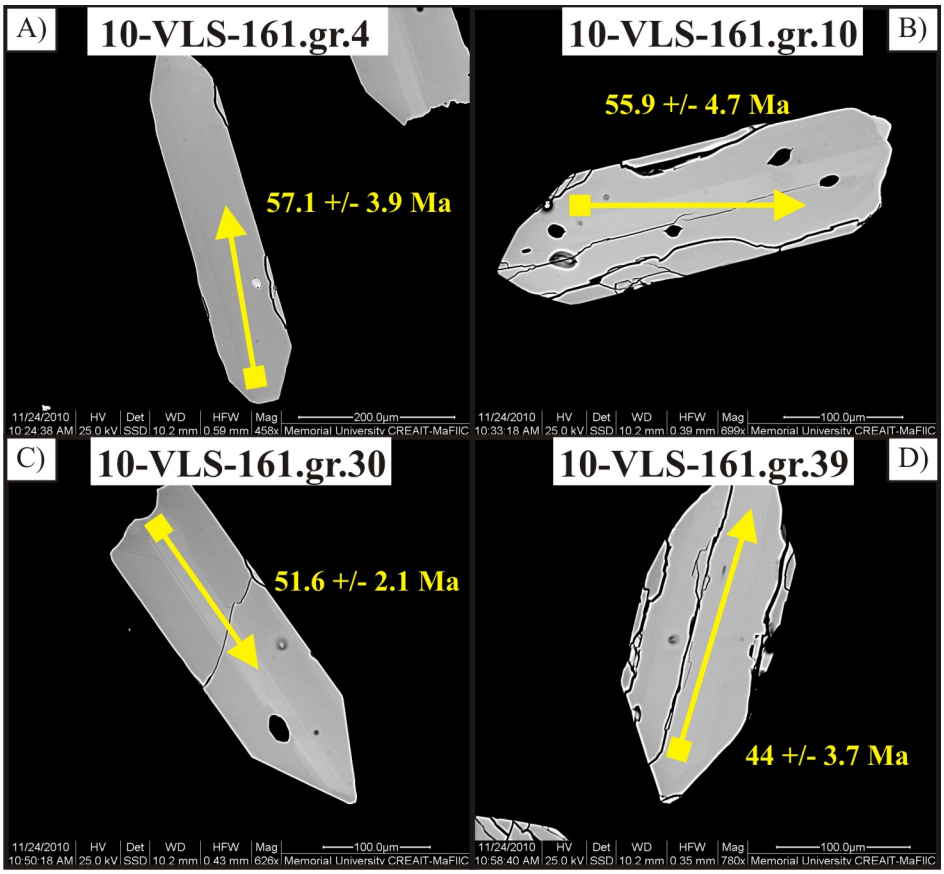

Figure 48: Example of BSE images of zircon grains from sample 10-VLS-161. Grain 4 (A), 10 (B), 30 (C), and 39 (D) showing BSE images labelled with line segments where targeted LA-ICPMS occurred. Corresponding U-Pb ages of analyses are indicated. Note the morphological similarities of the doubly-terminated zircon grains.

Grayling Lake (Figure 42 and 32). The dyke is a fine to medium grained weakly foliated chlorite-sericite-bearing tonalite rock that is folded into a tight, asymmetric southwest vergent F_3 fold structure. The weak foliation is an axial planar cleavage related to the F_3 fold and, it is defined by the alignment of chlorite and sericite. Age data calculated for this dyke is interpreted as a pre- to syn-D_3 age constraint.

Optical investigations of the various heavy mineral concentrates produced during mineral separation exhibited a lack of zircon. MLA was undertaken on the SEM to ascertain the presence of any zircon that possibly remained hidden from view. This resulted in finding tens of zircon grains, only three of which big enough to target given the limitations of the LA-ICPMS beam diameter. All three grains have very thin ($\leq$ 10 μm) overgrowth rims (Figure 51). BSE and CL images reveal all three grains are subhedral to anhedral in form with irregular and corroded grain boundaries. The cores of the three grains retain oscillatory and sector zoning textures indicating an igneous origin. Four analyses were completed on the

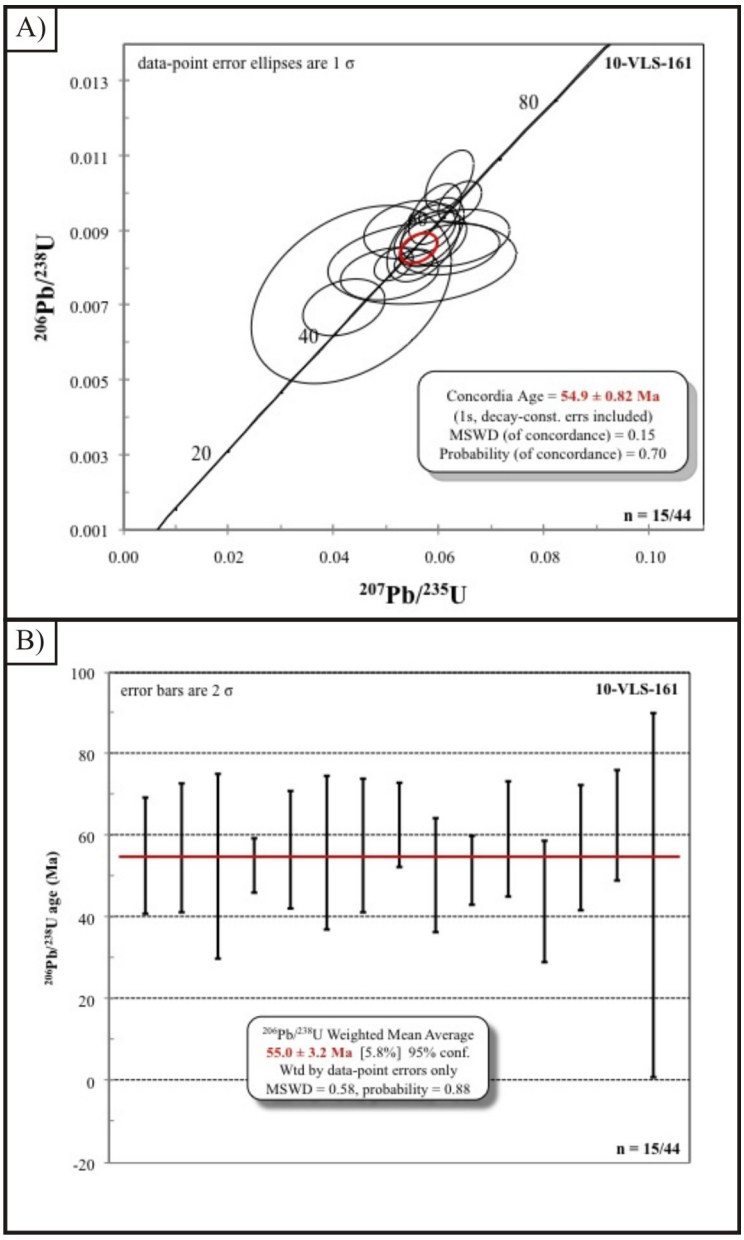

Figure 49: Concordia (A) and weighted mean average age (B) diagrams for LA-ICPMS analyses from sample 10-VLS-161. Calculated $^{206}Pb/^{238}U$ concordia age and $^{206}Pb/^{238}U$ weighted mean average age of fifteen most concordant analyses from sample 10-VLS-161. One sigma uncertainty ranges are documented for the ages plotted on the concordia diagram and two sigma uncertainty ranges for the ages plotted on the weighted mean average diagram. The age of crystallization for the sample is believed to be associated with the doubly terminated, 'igneous' zircon grains which provide a $^{206}Pb/^{238}U$ concordia age of 55.0 ± 3.2 Ma. The age of crystallization for 10-VLS-161 is based on the weighted mean average age since it retains a higher range of error than the concordia age (*i.e.,* ± 0.82 Ma).

three grains wherein all four analyses range from 95 to 105 % concordance (Figure 52). The two older Triassic analyses likely represent inheritance while the youngest age (77.0 ± 4.0 Ma) provides an upper age constraint for emplacement of the dyke.

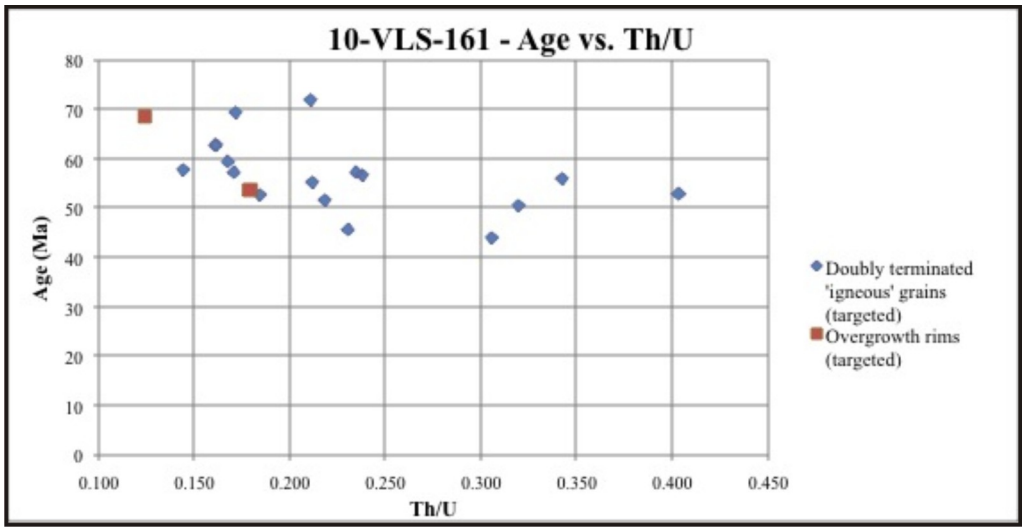

Figure 50: Plot of Th/U *vs.* age for zircon grains from sample 10-VLS-161. All nineteen analyses are less than 10 % discordant. Note the wide range of Th/U values correspond to a relatively small age bracket of analyses (*ca.* 45 to 70 Ma). Also note the targeted overgrowth rims (red squares) retain Th/U values similar to the Th/U values for the doubly terminated prismatic igneous grains (blue diamonds).

All four analyses from this sample exhibit a range of Th/U values from 0.155 to 0.498 (not shown here). Although these values are < 0.5, which would indicate an igneous origin, they are > 0.1 which indicates they are not related to recrystallized, metamorphic zircon (Hoskin and Black, 2000). This point, coupled with the igneous zoning textures mentioned above suggests the youngest $^{206}Pb/^{238}U$ age of 77.0 $\pm$ 4.0 Ma is more likely a crystallization age for the dyke. All three grains retain very thin overgrowth rims indicating a second zircon growth event took place post-77.0 $\pm$ 4.0 Ma. The overgrowth rims observed from this sample could very likely be related to the contemporaneous *ca.* 55 Ma magmatic/deformation event recorded by samples 10-RC-136 and 10-VLS-161 described above or a separate unknown, cryptic metamorphic event. Age data collected for the sample described thus far indicate D_3-related deformation took place during or after *ca.* 77 Ma, but pre-dates *ca.* 55 Ma.

4.4.4 Kluane gneiss sample

Sample 10-VLS-262 was collected from the central portion of the cordierite-bearing gneiss unit fifteen kilometers south-southeast of Gladstone Lakes (Figure 42). The outcrop is comprised of a medium to coarse grained foliated gneiss with abundant undeformed quartzofeldspathic ($\pm$ biotite) layers that vary in thickness from 1 to 10 cm (Figure 8). These layers are composed of randomly oriented quartz and feldspar phenocrysts ($\pm$ biotite) that, in places, overgrow the dominant foliation in the adjacent hornblende-biotite-rich melanocratic layers. Israel *et al.* (2011a) state this unit appears considerably different from the Kluane schist in that it

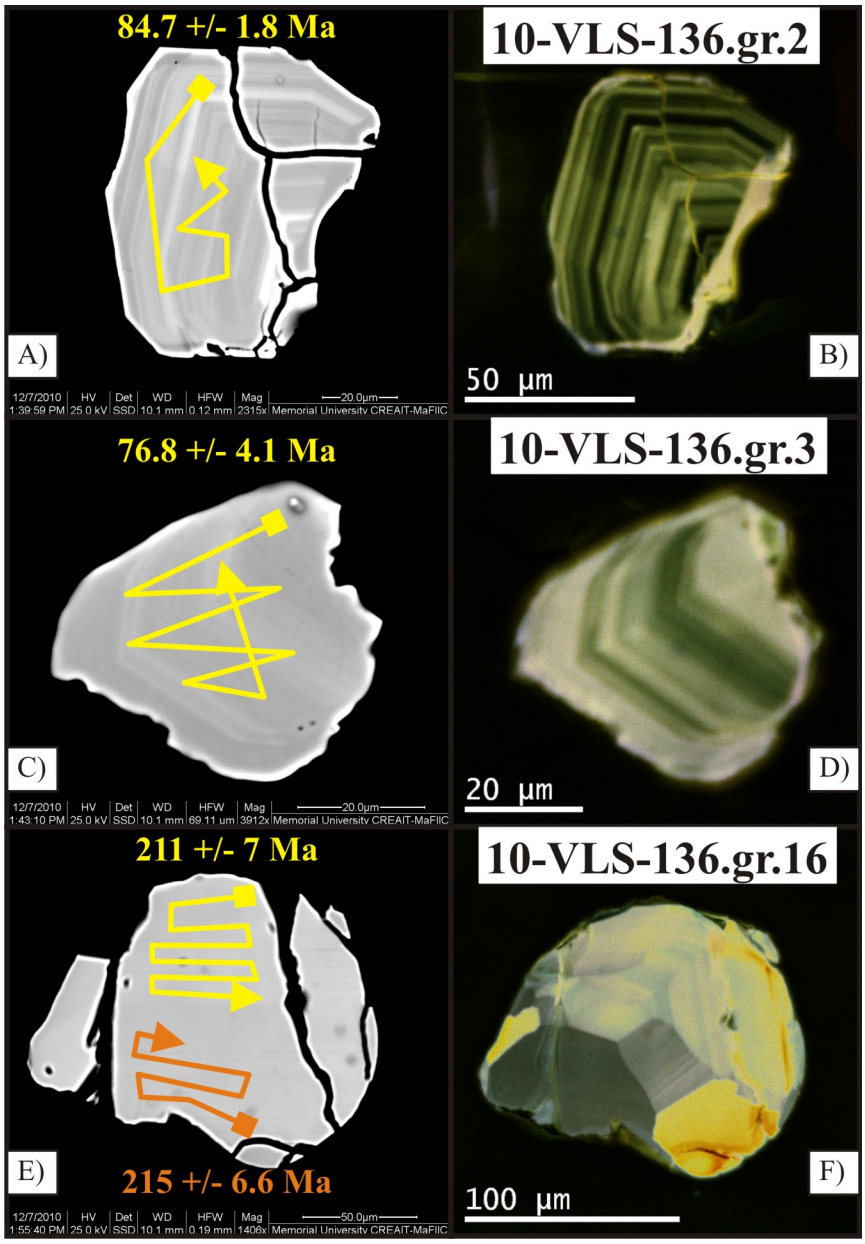

Figure 51: Example of BSE (left) and CL (right) images of zircon grains from sample 10-VLS-136. Grain 2 (A-B), 3 (C-D), and 16 (E-F) showing BSE images labelled with line segments where targeted LA-ICPMS occurred. Corresponding U-Pb ages of analyses are labelled. Note the oscillatory and sector zoning textures and the very thin overgrowth rims.

contains abundant igneous material as opposed to deformed quartz veins that are abundant in the schist. However, the transition from biotite-rich schist to cordierite-bearing gneiss is gradational over hundreds of meters wherein the quartzofeldspathic material is more abundant towards the east. The current study analyzed sample 10-VLS-262 under the assumption the igneous material is likely derived from partial melting of the Kluane schist. This hypothetical partial melting phase is believed to be due to heating of the structurally highest part of the

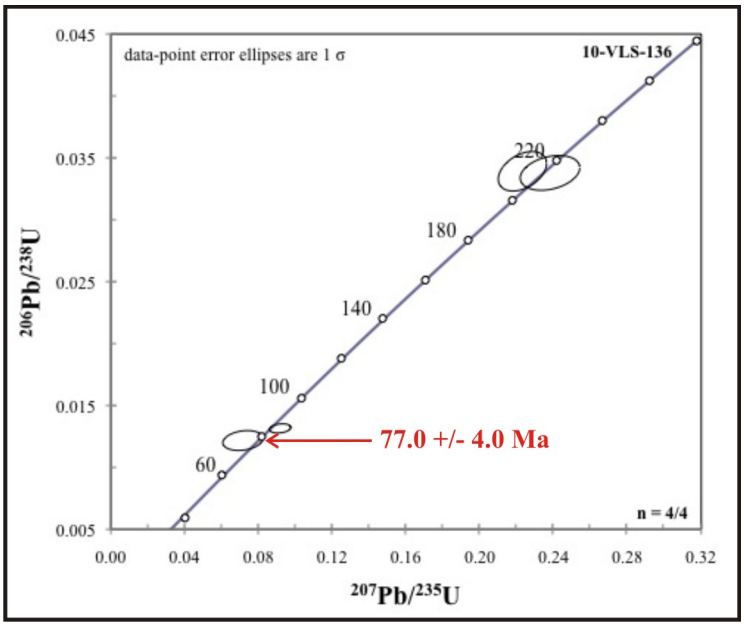

Figure 52: Concordia diagram showing four analyses of the three largest and most concordant zircon grains from sample 10-VLS-136. One sigma uncertainty ranges are documented for the four analyses plotted on diagram. The age of crystallization for the dyke is believed to be less than or equal to the youngest calculated $^{206}Pb/^{238}U$ concordia age of 77.0 $\pm$ 4.0 Ma.

Kluane schist where it was in contact with the voluminous *ca.* 64 to 57 Ma RRB (D.C. Murphy, pers. comm., 2010). LA-ICPMS targeting of epitaxial relationships of zircon grains appears to confirm this hypothesis. Nevertheless, age data calculated for this sample is meant to provide insight into the complexity, or lack thereof, of the zircon grain population(s) found in the sample.

BSE and CL images confirm all zircon grains from this sample are anhedral to subhedral in form and, all these grains retain penetrative overgrowth rims texturally different from the xenocrystic cores (Figure 53). Fifty-six analyses were completed on forty-four zircon grains from this sample; twelve overgrowth rims were targeted. Thirty-one analyses were less than 10 % discordant, seven of which are targeted rims. Three of the 'targeted' rims were contaminated by a proximal xenocrystic core age domain and therefore, they are excluded from the plots presented below. All targeted xenocrystic cores remain at least 18 million years older than the targeted rims. Similar to sample 10-RC-136, no pristine euhedral 'igneous' zircon grains were found and, data from the most concordant overgrowth rims are used to calculate the $^{206}Pb/^{238}U$ crystallization age for this sample. The most concordant data (*i.e.,* between $95 - 104$ % concordant) indicates the overgrowth rims formed at 65.6 $\pm$ 2.5 Ma (Figure 54).

Investigations of the xenocrystic core analyses from sample 10-VLS-262 appears to yield a trimodal signature with dominant peaks at $81 - 96$ Ma, $161 - 183$ Ma, and $346 - 347$

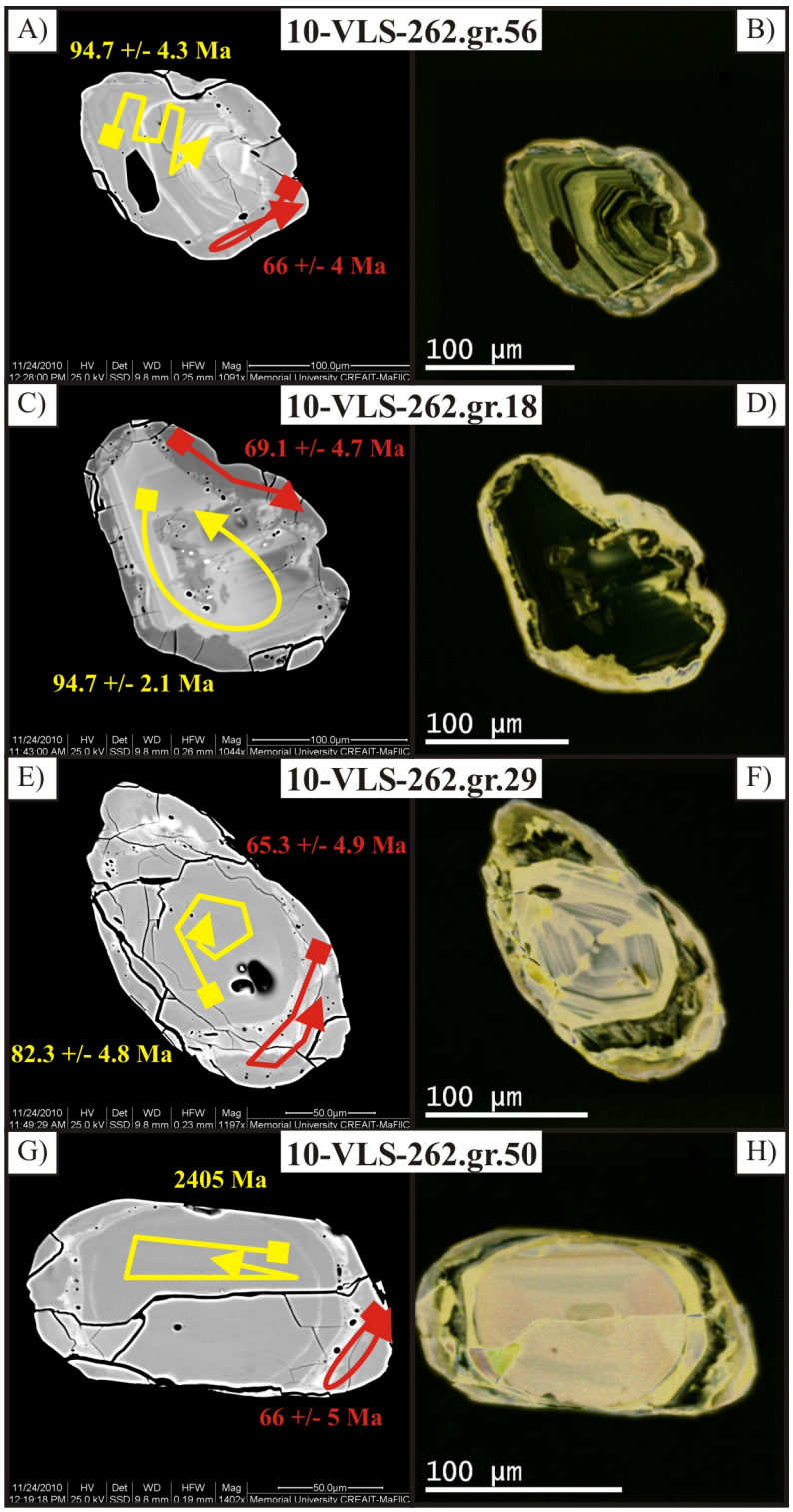

Figure 53: Example of BSE (left) and CL (right) images of zircon grains from sample 10-VLS-262. Grain 56 (A-B), 18 (C-D), 29 (E-F), and 50 (G-H) showing BSE images labelled with line segments where targeted LA-ICPMS occurred. Corresponding U-Pb ages of analyses are labelled. Note the variability of the xenocrystic core ages and the similarity (within error) of the overgrowth rim ages.

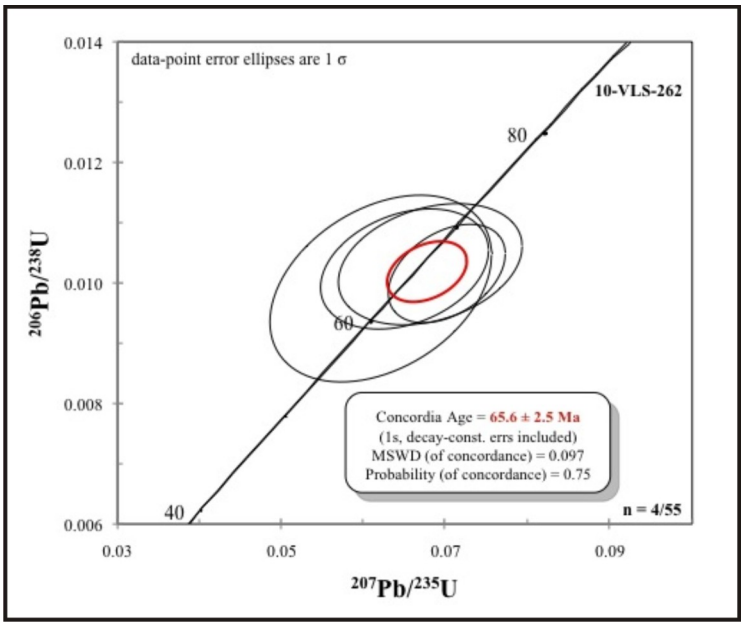

Figure 54: Concordia diagram showing most concordant targeted overgrowth rim analyses from sample 10-VLS-262. One sigma uncertainty ranges are documented for the four ages plotted on diagram. The age of crystallization for the gneiss is believed to be associated with these overgrowth rim analyses which provide a calculated $^{206}Pb/^{238}U$ concordia age of 65.6 $\pm$ 2.5 Ma (see red ellipse).

Ma (Figure 55). Single zircon ages at 107, 118, 249, 317 Ma just outside the time intervals indicate a possible increase in the signature of the peak widths. Single zircon ages also exist at approximately 1179, 1686, 2405, and 2533 Ma. When compared to the Kluane schist data-set presented above (Figure 44), the only difference sample 10-VLS-262 exhibits is the presence of an Early Carboniferous age peak; however, sample 09-VLS-085 does retain one Carboniferous aged analysis. The detrital zircon spectrum of samples 09SIT11 and 08DM126 collected from the Kluane schist presented by Israel *et al.* (2011; see their Figure 20, p. 113) show similar zircon age spectrum to 10-VLS-262. Therefore, the cordierite-bearing gneiss is interpreted to represent metamorphosed Kluane schist.

Of the thirty one relatively concordant Phanerozoic analyses, seven retain Th/U values $\leq$ 0.006 but three of these analyses are excluded due to erroneously targeting overlapping age domains (Figure 56). Coincidentally, the four remaining low Th/U values correspond to the targeted overgrowth rims with an age range from *ca.* 66 to 63 Ma. The targeted xenocrystic cores record older ages and higher Th/U values indicating inheritance of zircon grains from a compositional and temporal range of source rock(s). The four accurately targeted overgrowth rims used to represent the age of crystallization for the sample (*i.e.,* 65.6 $\pm$ 2.5 Ma) exhibit Th/U values indicative of recrystallization associated with metamorphic zircon (*i.e.,* $<$ 0.1; Hoskin and Black, 2000). The gneiss unit is recrystallized Kluane schist wherein

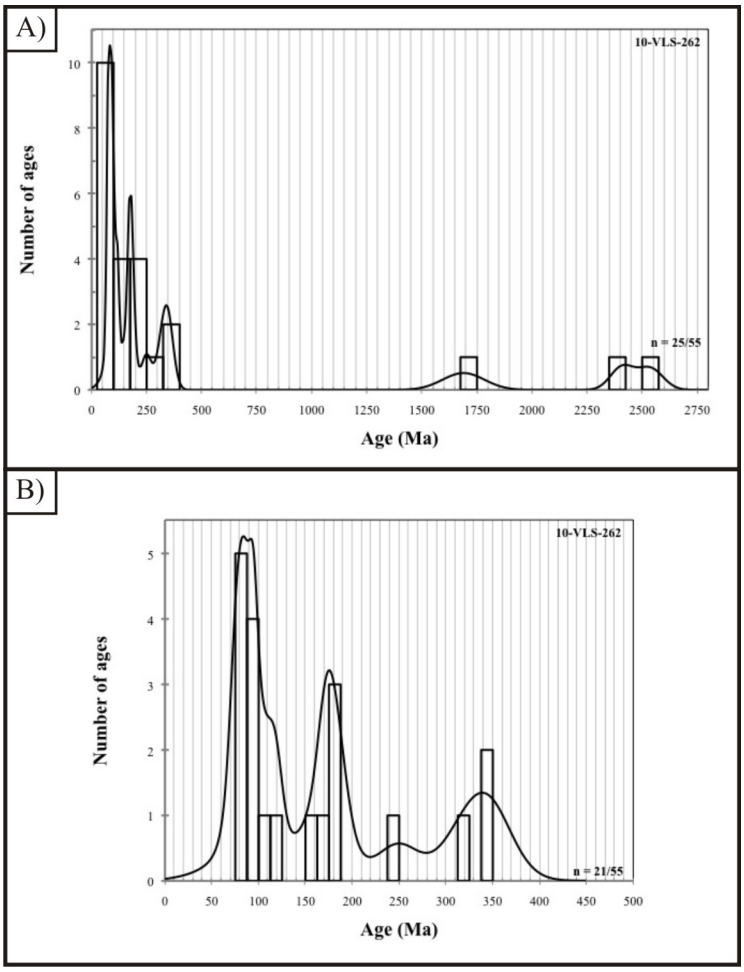

Figure 55: Histogram and probability distribution diagrams showing detrital zircon age distributions for sample 10-VLS-262 (excluding targeted overgrowth rim data). A) All data within 10 % of concordance and B) a detailed view of the Phanerozoic data-set.

the undeformed, igneous quartzofeldspathic layers likely represent a 'newly' formed partial melt phase. The partial melt phase likely formed as the result of relatively increased pressure and/or temperature conditions associated with the voluminous RRB (*ca.* 64 to 57 Ma; D.C. Murphy, pers. comm., 2010). During or after emplacement of this large granitic body, new zircon grew on the outer margins of xenocrystic cores.

4.5 Summary of U-Pb LA-ICPMS results

Uranium-Pb zircon LA-ICPMS analyses was completed on various rock-types in the study area to better understand: 1) the affinity of the source rock(s) of the Kluane schist; 2) the complexity of the zircon population(s) found in the cordierite-bearing gneiss at the boundary between the Kluane schist and RRB; and 3) the magmatic evolution that occurred prior to, during, and after the various deformation events that imparted tectonic fabrics onto the Kluane

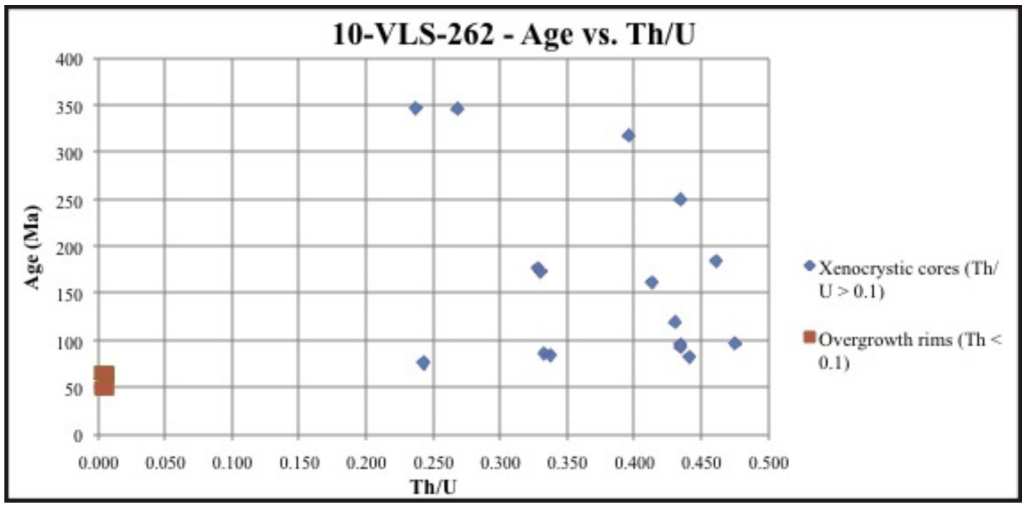

Figure 56: Plot of Th/U *vs.* age for zircon grains from sample 10-VLS-262. All analyses are less than 10 % discordant. Note analyses older than Proterozoic are excluded from the plot to focus on the Phanerozoic data-set. Also note the tight cluster of Th/U values for the overgrowth rims (red squares) and the variability of Th/U values for the xenocrystic cores (blue diamonds).

schist and gneiss.

Zircon grains collected from the four schist samples confirm a clear relationship between xenocrystic cores and penetrative overgrowth rims. Collectively, the four samples reveal significant age peaks exist at *ca.* $70-104$ Ma and $134-212$ Ma with minor age peaks between $229-349$ Ma and $2346-2691$ Ma. A comparison of data from Israel *et al.* (2011a) indicate age data between *ca.* 70 and 86 Ma collected for the current study likely represent a broad metamorphic age peak. The breadth and accuracy of the current data-set is not sufficient enough to decipher whether this time frame is host to one or multiple metamorphic events. Detailed targeting of xenocrystic cores and overgrowth rims by Israel *et al.* (2011a) distinguish at least two metamorphic events occurred at *ca.* 82 Ma and 70 Ma. Zircon age spectrum calculated for the current study are similar to that of the detrital age spectrum of Israel *et al.* (2011a). The source rock of the Kluane schist is situated to the east and is likely comprised of Late Triassic through mid-Cretaceous igneous phases that were built upon YTT.

One of the igneous samples (10-VLS-136) analyzed during this study is from a deformed D_3-related dyke that is folded into a tight, asymmetric, southwest vergent F_3 fold. Although the zircon yield is low for this sample, the three zircon grains analyzed confirm the dyke intruded during or after *ca.* 77 Ma. Notably, this time frame post-dates the *ca.* 82 Ma (Israel *et al.,* 2011a) main D_2-related tectonometamorphism (M_2) of the Kluane schist. Therefore, D_3-related deformation, metamorphism (*i.e.,* axial planar cleavage development; M_3), and felsic magmatism most likely related to the earliest stages of RRB emplacement appears to have begun as early as *ca.* 77 Ma, if not earlier. Very thin ($< 10\ \mu m$) overgrowth rims observed on

the three zircon grains from this sample indicate a post-77 Ma new zircon growth event. The rims were not analyzed due to instrument limitations. There is lack of igneous crystallization ages $\geq$ 77 Ma in the region, although there are vast regions of magmatic bodies whose age remains unkonwn.

The cordierite-bearing gneiss sample reveals a complex array of zircon grain populations. As is the case with the four schist samples, zircon grains from the gneiss sample retain clear textural differences between xenocrystic cores and overgrowth rims. The overgrowth rims analyzed from the cordierite-bearing gneiss formed at *ca.* 65 Ma. This age is interpreted to represent the youngest undeformed quartzofeldspathic igneous phase that overgrows the dominant foliation in the adjacent melanocratic layers of the outcrop where this sample was collected. Partial melting of the Kluane schist and formation of the gneiss is interpreted to have occurred in response to emplacement of the RRB some time after *ca.* 95 Ma, which represents the youngest detrital zircon found by Israel *et al.* (2011a). Geobarometry studies by Mezger (2001) indicate low pressure and high temperature conditions during formation of the cordierite-bearing gneiss unit indicating it was exhumed from a depth of approximately 24 km during or after D_2 to approximately 4 to 5 kbar (14 to 17.5 km depth) during D_3 partial melting. To have raised the temperature of such a large portion of the Kluane schist to form a partial melt phase, a significant portion of the RRB must have been emplaced prior to D_3.

The other two igneous samples (10-RC-136 and 10-VLS-161) confirm that syn- to post-kinematic emplacement of the HLIS occurred at *ca.* 55 Ma. On a regional scale, this unit is believed to have been emplaced between *ca.* 57 and 48 Ma (D.C. Murphy, pers. comm., 2010). Thermal heating and the formation of small contact metamorphic aureoles on the schist is associated with this felsic magmatic phase. This metamorphism coupled with the local exposures of foliated HLIS that are oriented parallel to D_4-related deformation in the adjacent schist indicates that parts of the HLIS intruded prior to or during D_4.

U-Pb zircon LA-ICPMS results are compiled with findings from the Chapter 3 to provide a tectonic context of how this part of the Canadian Cordillera evolved from the Late Cretaceous to present.

5 Tectonic model and conclusions

5.1 Tectonic model and structural evolution of the region encompassing the Kluane schist

Mezger's (1997, 2000, and 2003) geochemical, petrological, and structural studies indicate the Kluane schist protolith was a fine grained sedimentary rock derived from juvenile volcanic arc and mature continental sources. Those works interpreted the mixing of source rock(s), the lack of a remnant arc between the Kluane schist and North America, and the presence of unzoned ultramafic rocks structurally imbricated within and above the schist as evidence for the schist protolith to have been deposited in a relatively young and bouyant back-arc basin that collapsed by east-directed subduction in the Late Cretaceous. However, copious amounts of U-Pb zircon crystallization age dates obtained since those works by Mortensen and Hart (2010), for example, indicate that prior to and during deposition of the Late Cretaceous Kluane schist protolith, extensional arc magmatic signatures were present along the eastern side of Yukon-Tanana terrane (YTT), far from the basin that hosted the Kluane schist protolith (Figure 57A and 58A). U-Pb detrital zircon provenance work by Israel *et al.* (2011a) indicates the Kluane schist protolith was likely sourced from Jurassic to Cretaceous plutonic rocks that were built upon YTT to the east. The current study adheres to the notion that the Kluane schist sedimentary protolith was more likely deposited southwestward(?) into a closing Cretaceous seaway that originally represented the oceanic basin that separated Insular terrane from YTT prior to their amalgamation in the Jurassic (Nelson and Colpron, 2007). Closure of the seaway that eventually became host to sediments of the Kluane schist began in Triassic time when a broadly east dipping subduction zone was present outboard of the YTT margin (see Figure 13A). Engebretson (1985) indicates this time frame (as well as the time frame during deposition of the Kluane schist protolith) corresponds to a northwest moving Laurentian plate relative to a northeast moving Farrallon plate (Figure 58A). Although the exact magnitude of movement is not known, the relative sense of motion created by these plates define a left-lateral sense of motion at the interface of the two plates (Figure 58A). Planar and linear structural fabrics observed within the Kluane schist confirm that the early stages of deformation (*i.e.,* D_2) records oblique, sinistral northeast-over-southwest shearing and thrusting. At present, it is not known whether the Kluane schist sedimentary protolith was deposited upon either Insular terrane or YTT. Considering the significant amount of strain associated with rocks of the Kluane schist, it is also unclear as to the exact location (in terms of present day coordinates) where the Kluane schist basin was originally located relative to the western YTT margin.

The Dezadeash Formation, which presently outcrops southwest of the schist (see Figure 2),

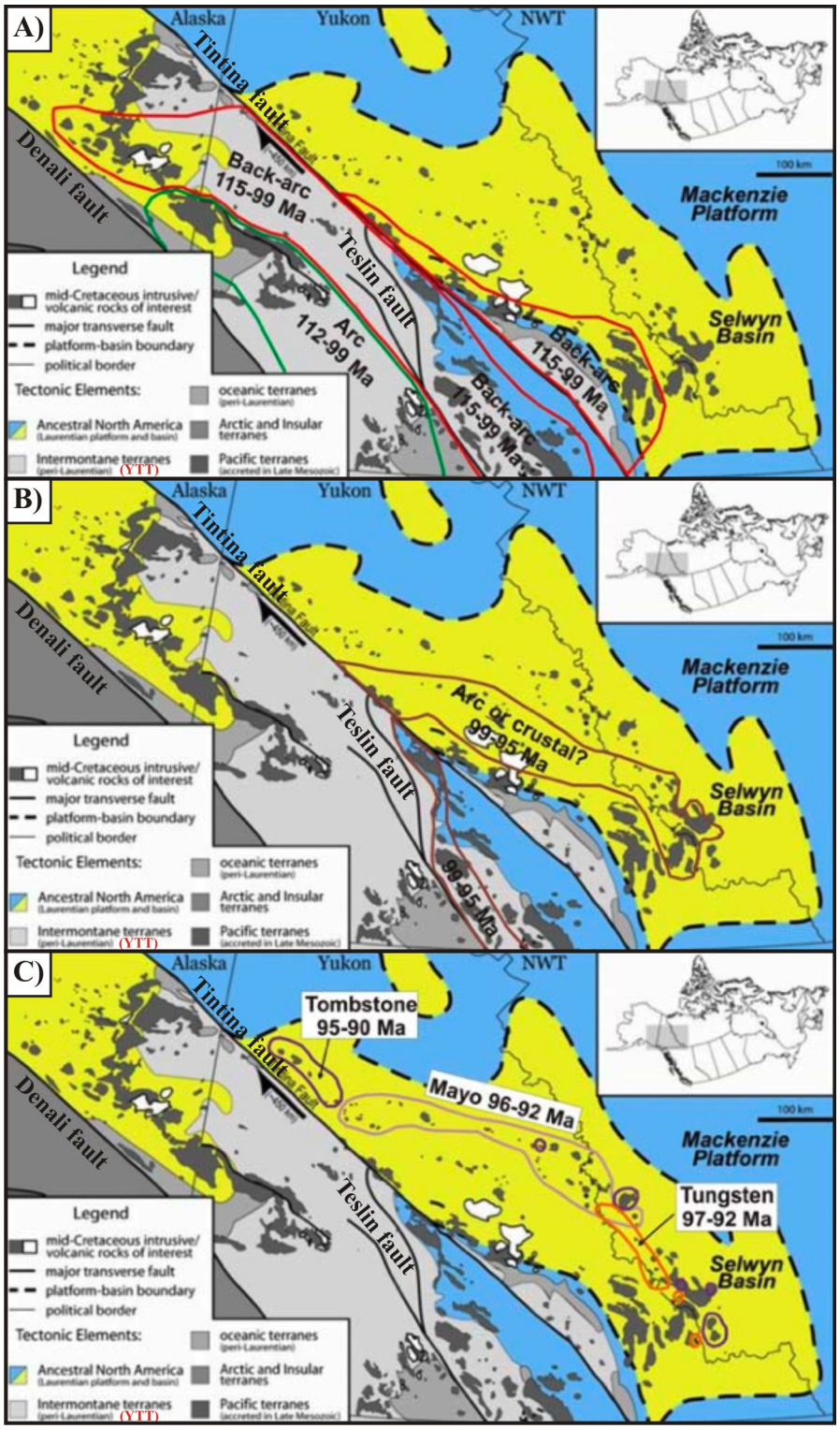

Figure 57: Distribution of Cretaceous magmatism in Yukon and eastern Alaska. The Kluane schist outcrops along the northern contact of the Denali fault in Yukon Territory. A) Approximate locations of 115 to 99 Ma back-arc (red polygons; intrusions associated with reduced compositions) and fore-arc magmatism (green polygon; intrusions associated with moderately oxidized compositions). B) Approximate locations of 99 to 95 Ma intermediate to mainly felsic magmatism (burgundy polygons; intrusions associated with arc-like compositions). C) Approximate locations of 96 to 90 Ma magmatism (indicated polygons; intrusions associated with enriched mantle back-arc-like compositions). By Mortensen and Hart (2010).

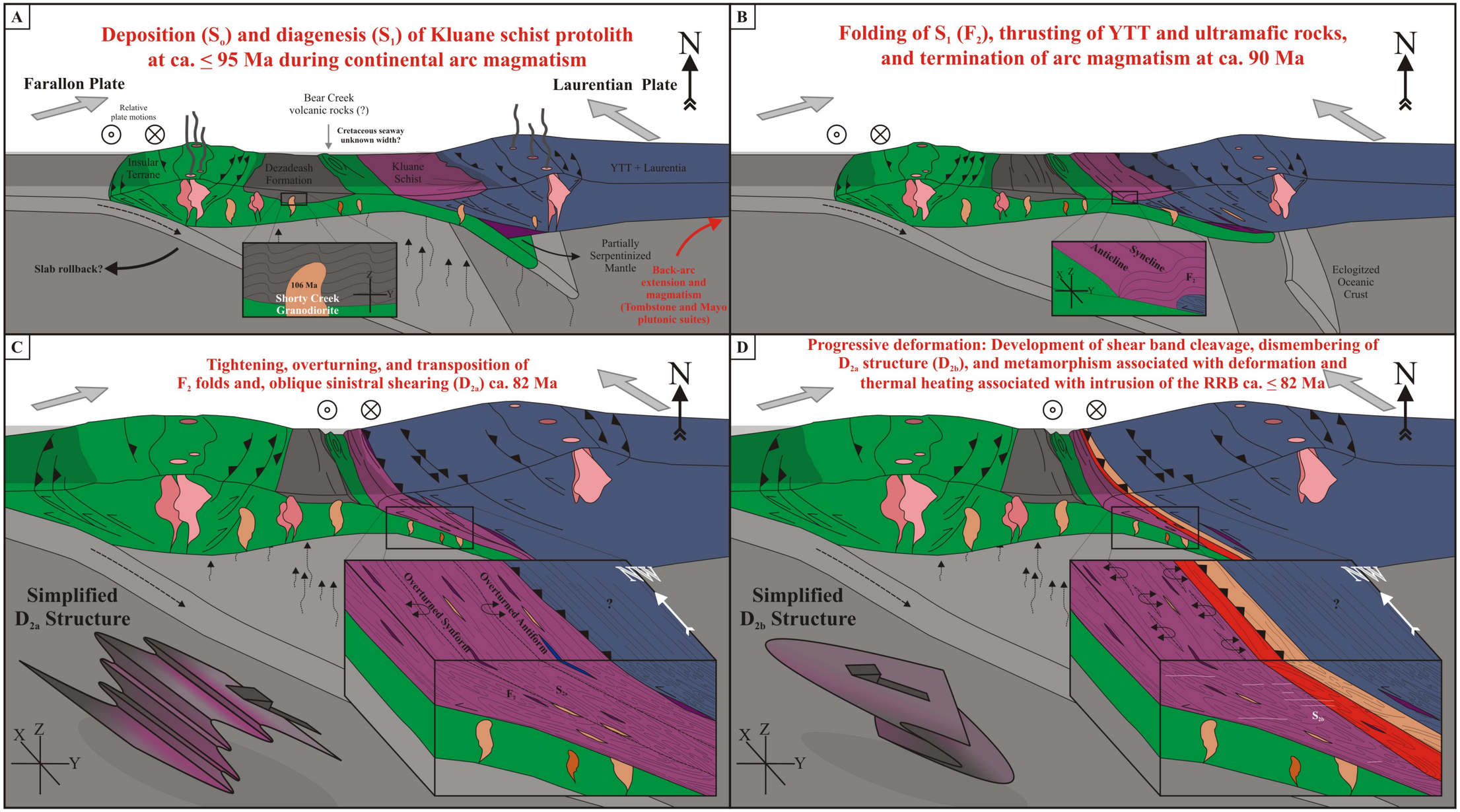

Figure 58: A conceptual tectonic model of southwestern Yukon Territory during deposition and deformation of the Kluane schist protolith. See text for details. Paleo-tectonic setting and relative plate motions displayed in A are adapted from data and figures by Eisbacher (1976), Engebretson et al. (1985), and Hampton et al. (2010) with references therein. Spatial relationship of magmatism in regards to each diagram are adapted from Mortenson and Hart (2010).

was already deposited and deformed prior to deposition of the schist protolith (Eisbacher, 1976). This geologic history is preserved by the *ca.* 106 Ma Shorty Creek granodiorite that cross-cuts east trending folds in the Dezadeash Formation (see inset diagram in Figure 58A). Given the significant amount of Tertiary and younger dextral strike-slip motion associated with the Denali fault and its subordinate splays (*i.e.,* upwards of 400 km), the originial spatial relationship between the Late Cretaceous Kluane schist and Jurassic-Cretaceous Dezadeash Formation is not clear. Figure 58A displays the two sedimentary units were deposited into opposing sides of the same basin. This spatial relationship is likely oversimplified since 400 km of Cenozoic dextral strike slip motion would obviously have juxtaposed units derived from sedimentary basins much further away from each other. Given the lack of marker horizons and the significant amount of bulk strain accumulated in the Dezadeash Formation and Kluane schist, the original width of this oceanic basin is not known. The affinity of the greenschist facies Bear Creek meta-volcanic rocks that outcrop north of Dezadeash Formation and west of the Kluane schist at present also remain undetermined (see Figure 2). Mezger (1997) records that the unit is the depositional base of the overlying Dezadeash Formation providing a pre-Late Jurassic upper age constraint for the metamorphosed volcanic rocks (Figure 58A). Although the contact between the Kluane schist and Dezadeash Formation/Bear Creek meta-volcanic rocks is not exposed at surface, Eisbacher (1976) hypothesizes the contact is a northeast dipping reverse fault. However, Cenozoic dextral strike-slip faulting associated with splays to the Denali fault system is also another plausible scenario for the juxtaposition of these two sedimentary units. Nevertheless, the interpreted fault contact likely formed some time after the *ca.* 82 Ma main D_2 event recorded in rocks of the Kluane schist since that event is associated with relatively more bulk strain and metamorphic mineral assemblages indicative of higher pressure and temperature conditions compared to the same variables in the Dezadeash Formation.

Prior to or during the main D_2 tectonometamorphic event, several wedges of ultramafic rocks became interleaved within and above the Kluane schist. This relationship is preserved by the conformable alignment of lithological contacts and foliations (S_{2a}) within the two units. The affinity and emplacement mechanism for the ultramafic rocks is uncertain. Mezger (1997 and 2000) believes they represent topographic highs on the down-going plate that were dismembered and entrained within and above the overlying Kluane schist during the collapse of a hypothetical back-arc basin (Mezger, 1997 and 2000). However, as noted above, back-arc basin magmatic signatures are only present inboard of the Kluane schist. Moreover, if these ultramafic bodies are associated with topographic highs of a down-going oceanic plate, there is a lack of imbricated basaltic bodies (*i.e.,* remnant seamounts) within the schist. Recent geochemical work by Escayola (pers. comm., 2011) indicates the ultramafic rocks at the northern portion of the study area (*i.e.,* Doghead Point, Kluane Lake) could represent portions

of the mantle that became fastened to the underside of YTT as it was thrust west over the Kluane schist (Figure 58B and C). The conformable nature of the lithological contacts and the parallel orientation of the structural fabrics indicate that the ultramafic rocks were at least in contact with the Kluane schist prior to or during D_2. U-Pb zircon age constraints indicate the ultramafic rocks at Doghead Point are Triassic in age (M. Escayola, pers. comm., 2011). The older ultramafic units are interpreted to have been placed in thrust contact with the Kluane schist prior to or during D_2. Prior to the D_2 tectonometamorphic event, a body of YTT also became interleaved within the Kluane schist. At the one exposure (west of Killermun Lake; see Figure 25), the strike and dip of the foliation in the YTT outcrop is conformable to the schist/YTT contact and, the transposition foliation in the schist. The current study interprets that the YTT body was thrust westward over the Kluane schist prior to or during the *ca.* 82 Ma D_2 event since both units preserve similar isoclinal fold structures (Figure 58B and C). The Kluane schist was eventually deformed, metamorphosed, and buried to a depth of 24 km at *ca.* 82 Ma during D_2 (Figure 58C and D). Burial and deformation-metamorphism is recorded by pressure and temperature calculations of porphyroblasts as well as penetrative overgrowth rims on zircon grains from the schist (*i.e.,* cordierite-bearing gneiss sub-unit; Mezger, 2001). The composite D_2 deformation event is associated with oblique ductile, sinistral shearing and folding. Pressure and temperature calculations from metamorphic minerals collected within the Kluane schist indicate that the 24 km depth represents maximum burial of the schist (Mezger, 1997). M_2 metamorphism was likely caused by shearing, structural stacking/thickening associated with isoclinal folding and thermal heating associated with intrusion of the early stages of the Ruby Range batholith (RRB). As the RRB intruded structurally above the Kluane schist, an inverted metamorphic aureole was created in the schist wherein metamorphic grade decreases down-section towards the southwest. Notably, this inverted M_2 metamorphic aureole is not folded by F_2 indicating that 1) isoclinal F_2 folding represents an early stage of D_2 deformation and 2) intrusion of the RRB began late during D_2 deformation. Future pressure and temperature work on metamorphic minerals from the Kluane schist will likely aid in understanding the exact mechanism responsible for M_2.

Following deposition of the schist protolith at $\leq$ *ca.* 95 Ma, arc magmatism is interpreted to have been terminated abruptly around *ca.* 90 Ma (Figure 58B). This interpretation is based on a lack of plutonic and volcanic rocks between *ca.* 90 and 78 Ma (Mortensen and Hart, 2010). The mechanism responsible for the termination of arc magmatism is not known.

Pressure and temperature calculations by Mezger (1997) as well as field relationships of overprinting fold and foliation patterns indicate that following the main D_2 event, the Kluane schist was simultaneously exhumed and deformed. These events are believed to be associated

with unroofing and D_3 and D_4 deformation events, respectively. D_3 began by as early as *ca.* 77 Ma and D_4 as early as 55 Ma. Whereas D_2 is associated with oblique sinistral motion as a result of the northwest moving Laurentian plate relative to the northeast moving Farallon plate, D_3 appears to be the result of almost orthogonal northeast-over-southwest shearing. The slight change in orientation infers a slight change in relative plate motion prior to and/or during the D_3 deformation in the forearc region. Regional scale F_3 folding of the cordierite-bearing Kluane gneiss confirms the inverted M_2 metamorphic aureole formed prior to D_3. D_4 deformation appears to be associated with near horizontal shortening wherein the axial plane of the regional scale F_4 fold remains nearly vertical and the fold axis is shallowly plunging towards the southeast. The timing of regional scale folding associated with D_4 is at least as old as the syn-kinematic intrusive phases associated with the Hayden Lake intrusive suite at *ca.* 55 Ma and, D_3-related deformation at *ca.* $\leq$ 77 Ma is associated with syn-kinematic intrusive phases associated with the RRB. The Kluane schist is interpreted to have arrived at its present structural level by *ca.* 55 Ma given the lack of post-D_4 deformation.

Mortensen and Hart (2010) display complex geochemical signatures from plutonic rocks in southwestern Yukon Territory that correlate with a similar time frame for RRB emplacement (*i.e.,* 78 and 72 Ma). These signatures are complex showing arc magmatic compositions as well as mantle derived plume-like compositions. That work interprets that the complexity of the magmatic signatures are related to arc magmatism and lithospheric delamination (Mortensen and Hart, 2010). Notably, geochemical and geochronological data regarding the voluminous RRB in the area proximal to the Kluane schist is lacking and future work on this batholith will surely add valuable geologic information to the region.

Nelson and Colpron (2007, p. 782) state that magmatism had all but ceased in the Canadian Cordillera by 40 Ma in response to the cessation of subduction off the west coast of Canada (subduction continues to the north off the coast of Alaska). At present, motion along the current plate margin is hosted by the dextral transcurrent Queen Charlotte fault (see Figure 1). Within the North American plate, dextral motion during this time frame has shifted between the Tintina and Denali faults. Within the study area, numerous geophysically determined strike-slip faults have been determined and are believed to be splays to the regional scale dextral transcurrent Denali fault system (see Figure 2). These faults remain hidden from view given the valleys that contain them are covered with Quaternary sediments. As Israel *et al.* (2011) notes, movement on subordinate faults related to the larger Denali fault system are difficult to resolve given the lack of good marker horizons within the Kluane schist.

The tectonic model and structural evolution presented here describes a very complex tectonic history of the Canadian Cordillera during deposition and deformation of the Kluane

schist. This tectonic history is believed to be dominated by compression in the fore-arc region above a northeast dipping subduction zone located outboard of Insular terrane.

5.2 Results and conclusions

Rocks of the Late Cretaceous Kluane schist record a complex geologic history with four different generations of structures recognized by fold and foliation overprinting patterns at the microscopic to mesoscopic scale. Two of these structures are associated with distinct fold patterns not previously differentiated in the schist. These two folding events are important tectonic vergence indicators that help resolve how the schist structurally evolved during the early stages of its deformation history. U-Pb detrital zircon ages reported for this study add to the pre-existing detrital zircon database for the region. As well, U-Pb zircon crystallization ages constrain when syn- and post-tectonic igneous phases related to the Ruby Range batholith and Hayden Lake intrusive suite intruded the schist. The current study presents the following new interpretations, results, and conclusions:

1. The Kluane schist is interpreted to have been deposited in a Late Cretaceous seaway that was in the process of complete closure. Although the amalgamation of Insular terrane and YTT is known to have occurred by at least the mid-Jurassic, this seaway could possibly have represented a remnant ocean basin that existed between YTT and Insular terrane.

2. Zircon grains collected from four samples of the schist have added to the detrital zircon data set of the region wherein significant age peaks exist at $70 - 104$ Ma and $134 - 212$ Ma with minor age evidence at 229, 241, 312, and 349 Ma. Subordinate ages include three Early Proterozoic to Late Archean ages (*ca.* 2346, 2686, and 2691 Ma).

3. The second deformation event (D_2) recorded in the Kluane schist was a protracted event involving oblique thrusting, folding, and shearing along a northeast-dipping sinistral shear zone. Contemporaneously, the early stages of RRB were being emplaced along the YTT/Kluane schist contact wherein thermal heating of the underlying Kluane schist occurred. These composite deformation and heating events resulted in the formation of an inverted contact metamorphic aureole that was progressively deformed.

4. A deformed tonalitic dyke sampled from within the schist and analyzed for U-Pb zircon geochronology indicates that D_3 occurred some time during or after *ca.* $\leq$ 77 Ma. However, overgrowth rims on zircon grains from quartzofeldspathic igneous phases in the cordierite-bearing Kluane gneiss formed at 65 Ma. These rims indicate that RRB emplacement occurred over a protracted time period from *ca.* 77 Ma to at least 65 Ma.

5. Following shearing and folding associated with D_2 and D_3, regional scale folding of planar pre-D_4 fabrics is believed to have been accommodated by flexural slip associated with sub-horizontal north-northeast/south-southwest compression. F_4 folding occurred some time after D_3 (*i.e., ca.* 77 Ma) and/or during intrusion of the syn- to post-kinematic igneous phases associated with the Hayden Lake intrusive suite at *ca.* 55 Ma. These relatively late igneous phases impart contact metamorphic aureoles onto the schist that are both concordant and discordant to the regional scale F_4 structure.

References

Bazard, D.R., Butler, R.F., Gehrels, G.E., and Soja, C.M., 1995. Early Devonian paleomagnetic data from the Lower Devonian Karheen Formation suggest Laurentia-Baltica connection for the Alexander terrane. *Geology*, 23, p. 707-710.

Bennett, V., and Tubrett, M., 2010. U-Pb isotopic age dating by LAM-ICP-Ms, INCO Innovation Centre, Memorial University: Sample preparation methodology and analytical techniques. *In* MacFarlene, K.E., Weston, L.H., and Blackburn, L.R., eds., Yukon Exploration and Geology 2009. *Yukon Geological Survey*, p. 47-55.

Beranek, L.P., and Mortensen, J.K., 2006. A Triassic link between Yukon-Tanana terrane and North America: New detrital zircon age, geochemical and biostratigraphic data. *Geological Society of America*, Abstracts with Programs, Cordilleran Section, 38, p. 5.

Bradley, D.C., Dumoulin, J., Layer, P., Sunderlin, D., Roeske, S., McClelland, W., Harris, A.G., Abbott, G., Bundtzen, T., and Kusky, T., 2003. Late Paleozoic orogeny in Alaska's Farewll terrane. *Tectonphysics*, 372, p. 23-40.

Colpron, M., 2006. Tectonic assemblage map of Yukon-Tanana and related terranes in Yukon and northern British Columbia (1:1,000,000 scale). *Yukon Geological Survey*, Open File 2006-1.

Colpron, M., Nelson, J.L., and Murphy, D.C., 2006. A tectonostratigraphic framework for the pericratonic terranes of the northern Canadian Cordillera. *In* Colpron, M., and Nelson, J.L., eds., Paleozoic Evolution and Metallogeny of Pericratonic Terranes at the Ancient Pacific Margin of North America, Canadian and Alaska Cordillera. *Geological Association of Canada*, Special Paper 45, p. 1-23.

Colpron, M., Nelson, J.L., and Murphy, D.C., 2007. Northern Cordilleran terranes and their interactions through time. *Geological Society of America Today*, 17, p. 4-10.

Corfu, F., Hanchar, J.M., Hoskin, P.W.O., and Kinny, P., 2003. Atlas of zircon textures. *In* Hanchar, J.M., and Hoskin, P.W.O., eds., Zircon: Reviews in Mineralogy and Geochemistry. *Mineralogical Society of America*, 53, p. 468-500.

Das, A., and Davis, D.W., 2010. Response of Precambrian zircon to the chemical abrasion (CA-TIMS) method and implications for improvement of age determinations. *Geochemica et Cosmochimica Acta*, 74, p. 5333-5348.

Dicken, A.P., 2005. Radiogenic Isotope Geology: Second Edition. Cambridge University Press (New York, 492 p.

Eisbacher, G.H., 1976. Sedimentology of the Dezadeash flysch and its implications for strike-slip faulting along the Denali fault, Yukon Territory and Alaska. *Canadian Journal of Earth Sciences*, 13, p. 1495-1513.

Engebretson, D., Cox, A., and Gordon, R.C., 1985. Relative motions between oceanic and continental plates in the Pacific Basin. *Geological Society of America*, Special Paper 106, 59 p.

Farrar, E., Clark, A.H., Archibald, D.A., and Way, D.C., 1988. Potassium-argon age of granitoid plutonic rocks, southwest Yukon Territory, Canada. *Isochron/West*, 51, p. 19-23.

Faure, G., and Mensing, T.M., 2005. Isotopes: Principles and Applications: Third Edition. John Whiley and Sons Inc. (New Jersey), 897 p.

Fedo, C.M., Sircombe, K.N., and Rainbird, R.H., 2003. Detrital zircon analysis of the sedimentary record. *In* Hanchar, J.M., and Hoskin, P.W.O., eds., Zircon: Reviews in Mineralogy and Geochemistry. *Mineralogical Society of America*, 53, p. 277-303.

Gibson, H.D., Brown, R.L., and Carr, S.D., 2005. U-Th-Ph geochronologic constraints on the structural evolution of the Selkirk fan, northern Selkirk Mountains, southern Canadian Cordillera. *Journal of Structural Geology*, 27, p. 1899-1924.

Goldfarb, R.J., Baker, T., Dube, B., Groves, D.I., Hart, C.J.R., and Gosselin, P., 2005. Distribution, character, and genesis of gold deposits in metamorphic terranes. emphSociety of Economic Geologists, Economic Geology 100th Anniversary Volume, p. 407-450.

Hampton, B.A., Ridgway, K.D., and Gehrels, G.E., 2010. A detrital record of Mesozoic island arc accretion and exhumation in the North American Cordillera: U-Pb geochronology of the Kahiltna basin, southern Alaska. *Tectonics*, 29, p. 1-21.

Harley, S.L., Kelly, N.M., and Moller, A., 2007. Zircon behaviour and the thermal histories of mountain chains. *Elements*, 3, 25-30.

Hoskin, P.W.O., and Black, L.P., 2000. Metamorphic zircon formation by solid-state recrystallization of protolith igneous zircon. *Journal of Metamorphic Geology*, 18, p. 423-439.

Israel, S., 2004. Geology of southwestern Yukon (1:250000 scale). *Yukon Geological Survey*, Open File 2004-16.

Israel, S., Cobbett, R., Westberg, E., Stanley, B.F., and Hayward, N., 2010. New insights into the geology and mineral potential of the Coast Belt, southwestern Yukon. *In* poster at Yukon Geoscience Forum annual meeting, Whitehorse, YT, Canada.

Israel, S., Murphy, D.C., Bennett, V., Mortensen, J., and Crowley, J., 2011a. New insights into the geology and mineral potential of the Coast Belt in southwestern Yukon. *In* Weston, L.H., and Relf, C., eds., Yukon Exploration and Geology 2010. *Yukon Geological Survey*, p. 101-123.

Israel, S., and Westberg, E., 2011b. Bedrock geology of the northwestern Aishihik Lake sheet, NTS 115H/12 and 13. *In* poster at Yukon Geoscience Forum annual meeting, Whitehorse, YT, Canada. *Yukon Geological Survey*.

Jaffey, A.H., Flynn, K.F., Glendenin, L.E., Bentley, W.C., and Essling, A.M., 1971. Precision measurement of the half-lives and specific activities of U235 and U238. *Physical Review*, 4, p. 1889-1907.

Johnston, S.T., and Erdmer, P., 1995. Hot-side-up aureole in southwestern Yukon and limits on terrane assembly of the northern Canadian Cordillera. *Geology*, 23, p. 419-422.

Johnston, S.T., Mortensen, J.K., and Erdmer, P., 1996. Igneous and metaigneous age constraints for the Aishihik metamorphic suite, southwest Yukon. *Canadian Journal of Earth Sciences*, 33, p. 1543-1555.

Lin, S., Jiang, D., and Williams, P.F., 2007. Importance of differentiating ductile slickenside striations from stretching lineations and variation of shear direction across a high-strain zone. *Journal of Structural Geology*, 29, p. 850-862.

Longerich, H., 2008. Laser ablation-inductively coupled plasma-mass spectrometry (LA-ICP-MS): An introduction. *In* Sylvester, P.J., eds., Laser ablation ICP-MS in the earth sciences: Current practices

and outstanding issues. Short Course Series. *Mineralogical Association of Canada*, 40, p. 1-18.

Lowey, G.W., 1992. Variation in bed thickness in a turbidite succession, Dezadeash Formation (Jura-Cretaceous), Yukon, Canada. Evidence of thinning-upward and thickening-upward cycles. *Sedimentary Geology*, 78, p. 217-232.

Lowey, G.W., 2007. Lithofacies analysis of the Dezadeash Formation (Jura-Cretaceous), Yukon, Canada: The depositional architecture of a mud/sand-rich turbidite system. *Sedimentary Geology*, 198, p. 273-291.

McClelland, W.C., and Saleeby, J.B., 1992. Upper Jurassic-lower Cretaceous basinal strata along the Cordilleran margin: Implications for the accretionary history of the Alexander-Wrangellia-Peninular terrane. *Tectonics*, 11, p. 823-835.

McClelland, W.C., Tikoff, B., and Manduca, C.A., 2000. Two-phase evolution of accretionary margins: examples from the North American Cordillera. *Tectonophysics*, 326, p. 37-55.

Mezger, J.E., 1997. Tectonometamorphic evolution of the Kluane metamorphic assemblage, SW Yukon: evidence for Late Cretaceous eastward subduction of oceanic crust underneath North America. *Ph.D. thesis*, University of Alberta, Edmonton, Alberta, 306 p.

Mezger, J.E., 2000. "Alpine-type" ultramafic rocks of the Kluane metamorphic assemblage, southwestern Yukon: Oceanic crust fragments of a late Mesozoic back arc basin along the northern Coast Belt. *In* Emond, D.S., and Weston, L.H., eds., *Yukon Exploration and Geology.* Exploration and Geological Services Division, Yukon Region, Indian and Northern Affairs Canada, p. 127-138.

Mezger, J.E., 2003. Geology of the Dezadeash Range and adjacent northern Coast Mountains (115A), southwestern Yukon: Re-examination of a terrane boundary. *In* Emond, D.S., and Weston, L.H., eds., *Yukon Exploration and Geology.* Exploration and Geological Services Division, Yukon Region, Indian and Northern Affairs Canada, p. 149-163.

Mezger, J.E., Creaser, R.A., Erdmer, P., and Johnston, S.T., 2000. A Cretaceous back-arc basin in the Coast Belt of the northern Canadian Cordillera: evidence from geochemical and neodymium isotope characteristics of the Kluane metamorphic assemblage, southwest Yukon. *Canadian Journal of Earth Sciences*, 38, p. 91-103.

Mezger, J.E., Chacko, T., and Erdmer, P., 2001. Metamorphism at a late Mesozoic accretionary margin: a study from the Coast Belt of the North American Cordillera. *Journal of Metamorphic Geology*, 19, p. 121-137.

Mihalynik, M.G., Nelson, J.L., and Diakow, L.J., 1994. Cache Creek terrane: oroclinal paradox within the Canadian Cordillera. *Tectonics*, 13, p. 575-595.

Mihalynik, M.G., Erdmer, P., Ghent, E.D., Cordey, F., Archibald, D.A., Friedman, R.M., and Johannson, G.G., 2004. Coherent French Range blueschist: Subduction to exhumation in ¡2.5 m.y.? *Geological Society of America Bulletin*, 116, p. 910-922.

Miller, E.L., Toro, J., Gehrels, G.E., Amato, J.M., Prokopiev, A., Tuchkova, M.I., Akinin, V.V., Dumitru, T.A., Moore, T.E., and Cecile, M.P., 2006. New insights into Arctic paleogeography and tectonics from U-Pb detrital zircon geochronology. *Tectonics*, 25, p. 1-19.

Monger, J.W.H., and Price, R., 2002. The Canadian Cordillera: Geology and tectonic evolution. *Canadian Society of Exploration Geophysicists Recorder*, February 2002, p. 17-36.

Mortensen, J.K., and Hart, C.J.R., 2010. Late and post-accretionary Mesozoic magmatism and metallogeny in the northern Cordillera, Yukon and east-central Alaska. *In* presentation at Geological Society of America annual meeting, Denver, CO, USA. *Geological Society of America*.

Muller, J.E., 1967. Kluane lake map-area, Yukon Territory (115G, 115F E1/2). *Geological Survey of Canada*, Memoir 340, 137 p.

Murphy, D.C., van der Heyden, P., Parrish, R.R., Klepacki, D.W., Mcmillan, W., Struik, L.C., and Gabites, J., 1995. New geochronological constraints on Jurassic deformation of the western edge of North America, southeastern Canadian Cordillera. *In* Miller, D.M., and Busby, C., eds., Jurassic Magmatism and Tectonics of the North American Cordillera. *Geological Society of America*, Special Paper 299, p. 159-171.

Murphy, D.C., Morentsen, J.K., and van Staal, C.R., 2009. 'Windy-McKinley' terrane, western Yukon: new data bearing on its composition, age, correlation and paleotectonic settings, *in* Weston, L.H., Blackburn, L.R., and Lewis, L.L., eds., Yukon Exploration and Geology. *Yukon Geological Survey*, p. 195-209.

Nelson, J., Colpron, M., Piercey, S.J., Dusel-Bacon, C., Murphy, D.C., and Roots, C., 2006. Paleozoic tectonic and metallogenetic evolution of pericratonic terranes in Yukon, northern British Columbia and eastern Alaska. *In* Colpron, M., and Nelson, J.L., eds., Paleozoic Evolution and Metallogeny of Pericratonic Terranes at the Ancient Pacific Margin of North America, Canadian and Alaska Cordillera. *Geological Association of Canada*, Special Paper 45, p. 323-360.

Nelson, J., and Colpron, M., 2007. Tectonics and metallogeny of the British Columbia, Yukon and Alaskan Cordillera, 1.8 Ga to present. *In* Goodfellow, W.D., ed., Mineral Deposits of Canada: A synthesis of Major Deposit-Types, District Metallogeny, the Evolution of Geological Provinces, and Exploration Methods. *Geological Association of Canada*, Mineral Deposits Division, Special Publication No. 5, p. 755-791.

Nicolaysen, L.O., 1961. Graphic interpretation of discordant age measurements on metamorphic rocks. *Annals of the New York Academy of Sciences*, 91, p. 198-206.

Nokleberg, W.J., Parfenov, L.M., Monger, J.W.H., Norton, I.O., Khanchuk, A.I., Stone, D.B., Scotese, C.R., Scholl, D.W., and Fujita, K., 2000. Phanerozoic tectonic evolution of the circum-North Pacific. *U.S. Geological Survey*, Professional Paper 1626, 122 p.

Passchier, C.W., and Trouw, R.A.J., 2005. Microtectonics: Second Edition. Springer, Berlin, 289 p.

Piercey, S.J., Nelson, J.L., Colpron, M., Dusel-Bacon, C., Murphy, D.C., Simard, R.L., and Roots, C.F., 2006. Paleozoic magmatism and crustal recycling along the ancient Pacific margin of North America, northern Cordillera. *In* Colpron, M., and Nelson, J.L., eds., Paleozoic Evolution and Metallogeny of Pericratonic Terranes at the Ancient Pacific Margin of North America, Canadian and Alaskan Cordillera. *Geological Association of Canada*, Special Paper 45, p. 281-322.

Piercey, S.J., and Colpron, M., 2009. Composition and provenance of the Snowcap Assemblage, basement of the Yukon-Tanana terrane, northern Cordillera: Implications for Cordilleran crustal growth. *Geosphere*, 5, p. 439-464.

Ramsay, J.G., and Huber, M., 1987. The Techniques of Modern Structural Geology: Volume 2: Folds and Fractures. Academic Press Inc. (London) Ltd., 700 p.

Ridgway, K.D., Trop, J.M., Nokleberg, W.J., Davidson, C.M., and Eastham, K.R., 2002. Mesozoic and Cenozoic tectonics of the eastern and central Alaska Range: Progressive basin development and

deformation in a suture zone. *Geological Society of America Bulletin*, 114, p. 1480-1504.

Ross, C.A., and Ross, J.R.P., 1983. Late Paleozoic accreted terranes of western North America. *In* Stevens, C.H., eds., Pre-Jurassic Rocks in Western North American Suspect Terranes: Pacific Section. *Society of Economic Paleontologists and Mineralogists*, Los Angeles, California, p. 7-22.

Silberling, N.J., Jones, D.L., Monger, J.W.H., Coney, P.J., Berg, H.C., and Plafker, G., 1994. Lithotectonic terrane map of Alaska and adjacent parts of Canada. *In* Plafker, G., and Berg, H.C., eds., The Geology of Alaska. *Geological Survey of America*, The Geology of North America, v. G-1, Plate 3, scale 1:2,500,000.

Wheeler, J.O., and McFeely, P., 1991. Tectonic assemblage map of the Canadian Cordillera and adjacent parts of the United States of America. *Geological Survey of Canada*, Map 1712A, scale 1:2,000,000.

Whetherill, G.W., 1956. An interpretation of the Rhodesia and Witwatersrand age patterns. *Geochimica et Cosmochimica Acta*, 9, p.290-292.

Williams, P.F., and Price, G.P., 1990. Origin of kinkbands and shear-band cleavage in shear zones: an experimental study. *Journal of Structural Geology*, 12, p. 145-164.

Winter, J.D., 2001. An Introduction to Igneous and Metamorphic Petrology. Prentice-Hall Inc. (New Jersey), 697 p.

Appendix

A Bedrock geology map of the area encompassing the Kluane schist, southwestern Yukon Territory (1:100,000 scale)

This pdf file can be obtained from the Department of Earth and Environmental Sciences, upon request.

Appendix

B U-Pb zircon LA-ICPMS data

This excel spreadsheet file can be obtained from the Department of Earth and Environmental Sciences, upon request.